ATOMIC-SCALE INSIGHTS INTO ENERGY CONVERSION IN TWO-DIMENSIONAL TRANSITION METAL DICHALCOGENIDE MONOLAYERS FROM *AB-INITIO* STUDIES

DIMPLE

(PH14209)

A thesis submitted for the partial fulfillment of

the degree of Doctor of Philosophy

Institute of Nano Science and Technology

Phase-10, Sector-64, Mohali, Punjab-160062, India.

And

Indian Institute of Science Education and Research Mohali

Knowledge city, Sector 81, SAS Nagar, Manauli PO, Mohali 140306, Punjab, India.

September 2019

Declaration

The work presented in this thesis has been carried out by me under the guidance of Dr. Abir De Sarkar at the Institute of Nano Science and Technology (INST) Mohali. This work has not been submitted in part or in full for a degree, a diploma, or a fellowship to any other university or institute. Whenever contributions of others are involved, every effort is made to indicate this clearly, with due acknowledgement of collaborative research and discussions. This thesis is a bonafide record of original work done by me and all sources listed within have been detailed in the bibliography.

Dimple
(Candidate)

In my capacity as the supervisor of the candidate's thesis work, I certify that the above statements by the candidate are true to the best of my knowledge.

Dr. Abir De Sarkar
(Supervisor)
Associate Professor, Scientist-E
Institute of Nanoscience and Technology, Mohali

To my beloved family members

Acknowledgment

This 5-year journey towards a Ph.D. has been an important phase in my life which contributed immensely to my growth as a researcher and overall as a person.

I am indebted to my Ph.D. supervisor *Dr. Abir De Sarkar* for his unconditional support and limitless patience. I would like to express my deep gratitude to him for his invaluable advice, professional guidance and everlasting encouragement from my early days when I joined the group. It is my immense privilege and luck to have had the opportunity to work and learn from such an expert and enthusiast. He has great vision and deep understanding of research field, but also has the flexibility and an open mind to grant me the freedom to explore my own interests and provide guidance when I get lost in uncharted land. He never clipped my wings to a narrow research field. The commendable language skill, effective communications and excellent scientific discussions with him have paved a great benefit to me. I am extremely very fortunate to work with such an outstanding individual and feel truly honored as his student. He pushed me to do better, to improve myself, and test my limits not only as a student but as a whole person. His inspirational character would always guide me in my future career.

I had also been fortunate enough to work in collaboration with research groups of *Dr. Kiran Sankar Hazra* & *Dr. Ramendra Sundar Dey*. They offered generous scientific help and insightful discussions on collaborative projects.

I express my genuine thanks and great appreciation to my group members. *Nityasagar* deserves a special thanks for helping me cope with all the challenges during this journey. His knowledge, intuition and enthusiasm was a true inspiration.

I highly acknowledge and greatly thankful to *Dr. Seema Gautam*, the post-doctoral fellow in our group for her immediate help, support and insightful scientific discussions. I extend my heartfelt thanks to *Ashima, Raihan, Manish* and *Pradip* being involved in many different insightful scientific aspects and their benign support towards this work.

Furthermore, I highly thank my colleagues and friends, *Soumen, Rajinder, Ankur, Ashmeet, Munish, Swati, Rashmi, Ritu, Prabhjot, Neha* and *Ruchi* for all the good times we had, and who had been there for helping me when I needed. I would also thank lab members of collaborating groups: *Renu, Anirban,* and *Taniya* for their help and fruitful discussions.

I also thank all my teachers who taught me during my course work period both at INST and IISER Mohali.

No work is possible without adequate resources, and in this respect I gratefully acknowledge

the Ph.D. fellowship and the infrastructural support provided by the Department of Science and Technology (DST) and the Institute of Nano Science and Technology (INST), India which makes possible for me to carry out related research activities and finish this thesis. I remain thankful to Centre for Development in Advanced Computing (C-DAC), Pune, India for providing its supercomputing facilities on PARAM-YUVA-II.

Lastly, yet most importantly, what I am today is because of my supreme God “My Parents”. They have taught me to be strong and be courageous even when life hits with the worst hurdles. They have supported me through the highs and lows of life with unconditional love. I am very lucky to have a wonderful sister *Sumita*, jiju *Gautam* and my niece *Tanishka*, who have been always supportive of my dreams. I can never pay back the support provided by my in-laws during this period. The final credit goes to the very special persons in my life, my dear love, wife *Parul* and my little angle, daughter *Yuvika*. I deeply thank for their love, unconditional support, and patience.

Dimple

Abstract

This thesis highlights different kinds of energy conversion in atomically thin, two-dimensional (2D) transition metal dichalcogenide (TMDC) monolayers. More precisely, nanoelectromechanical energy conversion (piezoelectricity), scavenging waste heat into electricity (thermoelectricity) and solar energy harvesting (artificial photosynthesis) based on 1T-MX_2 (M=Zr, Hf; X = S, Se, Te) and 1H-MoS_2 monolayers have been addressed in the thesis. As carrier mobility commonly influences all these kinds of energy conversion, it has also been thoroughly investigated as well. Atomic-scale understanding reached *via* state-of-art first-principles calculations based on density functional theory (DFT) has been employed to uncover their electronic, optical, mechanical, piezoelectric and thermoelectric properties. First of all, the thesis introduces the occurrence of piezoelectricity in 2D semiconducting transition metal dichalcogenide monolayers, such as 1H-MoS_2, which arises from the breaking of inversion symmetry. However, pristine, semiconducting 1T-MX_2 (M=Zr, Hf; X = S, Se, Te) monolayers are intrinsically centrosymmetric and hence, non-piezoelectric. This inversion symmetry is broken in their Janus monolayer (non-centrosymmetric) structures, leading to the emergence of a high level of piezoelectricity in them. It brings along a new dimension in nanoscale piezoelectricity, as the origin of this piezoelectricity is predominantly ionic in nature, in contrast to 1H-MoS_2 monolayer, where it is of electronic character. Next, the mechanism underlying the compressive strain induced enhancement in thermoelectric power-factor has been unveiled in single-layer MoS_2, using density functional theory coupled to Boltzmann transport equation. A synergic coupling between the lattice vibrational properties and high Born effective charges in monolayer Hafnium dichalcogenides, such as HfS_2, $HfSe_2$ and their Janus derivative HfSSe, have been explored to reach the origin of ultralow lattice thermal conductivity in them. Finally, the effect of strain and pH on the artificial photosynthetic properties in single layer MoS_2 has been comprehensively studied in terms of band edges straddling the water redox potential, CO_2 reduction levels, optical conductivity, absorbance, carrier mobility and carrier mobility ratio in order to ascertain the type and magnitude of strain under which photocatalytic activities are optimally enhanced.

The thesis stresses the importance of finding sustainable, clean and alternative energies through efficient use and engineering of 2D materials. The approach adopted in the Ph.D. work consists in studying the several intertwined properties in a multifunctional material, thereby enabling to draw a systematic correlation between them.

****

List of Publications

■ Part of the thesis

1. **Dimple**, Nityasagar Jena, Ashima Rawat, Raihan Ahammed, Manish Kumar Mohanta, Abir De Sarkar*, "Emergence of high piezoelectricity along with robust electron mobility in Janus structures in semiconducting Group IVB dichalcogenide monolayers", **J. Mater. Chem. A** 2018, 6, 24885-24898

2. **Dimple**, Nityasagar Jena, Abir De Sarkar, "Compressive strain induced enhancement in thermoelectric-power-factor in monolayer MoS_2 nanosheet", ***Journal of Physics: Condensed Matter*** 2017, 29, 225501 (7pp)

3. **Dimple** et al., "Ultra-low lattice thermal conductivities and Phonon-Electric field coupling effects in Hafnium dichalcogenide monolayers" [To be submitted]

4. **Dimple**, Nityasagar Jena, Ashima Rawat, Abir De Sarkar*, "Strain and pH facilitated artificial photosynthesis in monolayer MoS_2 nanosheet", ***J. Mater. Chem. A*** 2017, 5, 22265-22276

■ Not included in the thesis

5. **Dimple**, Nityasagar Jena, Shounak Dhananjay Behere, Abir De Sarkar, "The effects of different possible modes of uniaxial strain on the tunability of electronic and band structures in MoS_2 monolayer nanosheet *via* first-principles density functional theory", **Pramana-Journal of Physics–Springer** 2017, 89, 1-7

6. Nityasagar Jena, **Dimple**, Shounak Dhananjay Behere, Abir De Sarkar, "Strain Induced Optimization of Nanoelectromechanical Energy Harvesting and Nanopiezotronic Response in MoS_2 Monolayer Nanosheet", **J. Phys. Chem. C** 2017, 121, 9181–9190

7. Renu Rani, **Dimple**, Nityasagar Jena, Anirban Kundu, Abir De Sarkar, Kiran Shankar Hazra, "Controlled formation of Nanostructures on MoS_2 Layers by Focused Laser Irradiation", **Applied Physics Letters** 2017, 110, 083101

8. Nityasagar Jena, **Dimple**, Raihan Ahammed, Ashima Rawat**,** Manish Kumar Mohanta, Abir De Sarkar*, "Valley drift and valley current modulation in a strained monolayer MoS_2", **Physical Review B** 2019, 100, 165413

9**.** Ashima Rawat**,** Nityasagar Jena, **Dimple**, Abir De Sarkar*, "A comprehensive study on carrier mobility and artificial photosynthetic properties in group VI B transition metal dichalcogenide monolayers", **J. *Mater. Chem. A*** 2018, 6, 8693– 8704

10. Ashima Rawat**,** Raihan Ahammed, **Dimple**, Nityasagar Jena, Manish Kumar Mohanta, Abir De Sarkar*, "Solar Energy Harvesting in Type II Van Der Waals Heterostructures of Semiconducting Group III Monochalcogenide Monolayers", **J. Phys. Chem. C** 2019, 123, 12666−12675

11. Raihan Ahammed, Ashima Rawat**,** Nityasagar Jena, **Dimple**, Manish Kumar Mohanta, Abir De Sarkar*, "ZrS_3/MS_2 and ZrS_3/MXY (M=Mo, and W; X, Y=S, Se, and Te) type-II van der Waals hetero-bilayers: prospective candidates in 2D excitonic solar cells", **Applied Surface Science** 2020, 499, 143894

12. Manish Kumar Mohanta, Ashima Rawat, **Dimple**, Nityasagar Jena, Raihan Ahammed and Abir De Sarkar**,** "Super-high out-of-plane piezoelectricity, low thermal conductivity and photocatalytic abilities in ultrathin 2D van der Waals heterostructures of Boron Monophosphide and Gallium Nitride", **Nanoscale** 2019, DOI: 10.1039/C9NR07586K

13. Taniya Purkait, **Dimple,** Manisha Das, Navpreet Kamboj, Subhajit Sarkar, Abir De Sarkar and Ramendra Sundar Dey, "Outstanding cycling capability of electrochemically active high-power pseudocapacitor; A mechanistic approach to study the superior performances" [Advanced Energy Materials, In Review]

14. Manish Kumar Mohanta, Ashima Rawat, Nityasagar Jena, **Dimple**, Raihan Ahammed and Abir De Sarkar**,** "Ultrathin hetero-bilayer of MoS2/boron-monophosphide for a colossal performance in thermoelectrics, 2D excitonic solar cell and nanopiezotronics" [Applied Materials & Interfaces, In Review]

15. Manish Kumar Mohanta, **Dimple**, Ashima Rawat, Nityasagar Jena, Raihan Ahammed and Abir De Sarkar**, "**Ultra-low thermal conductivity and super-slow hot-carrier thermalization induced by a huge phononic gap in multifunctional boron pnictide (BX (X = P, As, Sb)) monolayers", [To be submitted]

Contents

List of Figures

List of Tables

Abbreviations

BEC	Born Effective charges
BZ	Brillouin Zone
CBM	Conduction Band Minima
DFPT	Density Functional Perturbation Theory
DFT	Density Functional Theory
GGA	Generalized gradient approximation
KS	Kohn-Sham scheme
PBE	Perdew-Burke-Ernzerhof functional
TEMs	Thermoelectric materials
TMDC	Transition-metal dichalcogenide
VBM	Valence Band Maxima
vdWs	van der Waals

Symbols

$\hbar$	Plank constant
k_L	Lattice thermal conductivity
k_e	Electronic thermal conductivity
σ	Electric conductivity
S	Seebeck coefficient
θ_D	Debye temperature
ZT	Figure-of-Merit
Z_{ij}^*	Born Effective charge
T	Temperature in K
E_c	Cohesive energy per unit cell
$\mu_\perp$	Vertical dipole moment
m^*	Effective mass of electron/hole
σ_{ij}	Elastic stress tensor
ε_{kl}	Elastic strain tensor
C_{ijkl}	Total elastic stiffness tensor
P_i	Polarisation vector
e_{ijk}	Piezoelectric stress coefficient
d_{ijk}	Piezoelectric strain coefficient

"Do the difficult things while they are easy and do the great things while they are small. A journey of thousand miles begins with a single step." ***Lao Tzu***

Chapter 1

Introduction

1.1 Background: Two-dimensional materials

The evolution of human civilizations has an interesting history of discovering and designing new materials [1]. From the Stone, Bronze and Iron Ages to the modern Information Age that is built on the basis of silicon semiconductors, materials have always been an epitome of science and technology development.

Over the last decade, two-dimensional (2D) layered nanomaterials is one of the fastest developing areas in contemporary Nanoscience and Technology. 2D materials, referred to as "atomically-thin crystals" consisting of one- to few- layer thickness of atoms. In fact, for a long time, it was argued in the scientific community that no crystal could ever exist in its 2D form. Peierl [2] (in 1935) and Landau [3] (in 1937) theoretically demonstrated that one- and two-dimensional crystals could not exist because of infinite fluctuation in atomic displacements at finite temperature. Later, Mermin and Wagner [4,5] extended this hypothesis in their work, which was strongly endorsed by the experimental observations, where the melting point of thin films was shown to reduce rapidly with decrease in lattice thickness. This solidified the understanding of supported thin films and yielded a longstanding belief that these materials can only be grown on solid substrates with negligible lattice mismatch, but they can't be stable in their freestanding/isolated form. This prevalent knowledge persisted for a long-term until K. Novoselov and A. Geim made this impossible possible, which eventually led to their Nobel Prize (in 2010) recognizing their successful exfoliation of graphene in 2004 [6] and its exotic properties.

The success of graphene has generated tremendous interest in other 2D materials, where the use of different elements opens new endeavours for exciting physics and miniaturized devices for future generations (see Figure 1.1. 1). These include the well-known mono-elemental crystals 2D-Xenes (e.g. silicene, germanene) [7], Group VA 2D-Xenes (e.g. phosphorene, bismuthene) [8,9], transition metal dichalcogenides (TMDCs, e.g. MoS_2, WS_2)[10], Group III–V semiconductors and insulators (e.g. GaN, InP)[11], transition metal carbides and nitrides (MXenes, e.g. Ti_2CO_2)[12], post-transition metal chalcogenides (e.g. GaS, GaSe) [13], transition metal trihalides (e.g. CrI_3) [14], and organic-inorganic hybrid perovskites

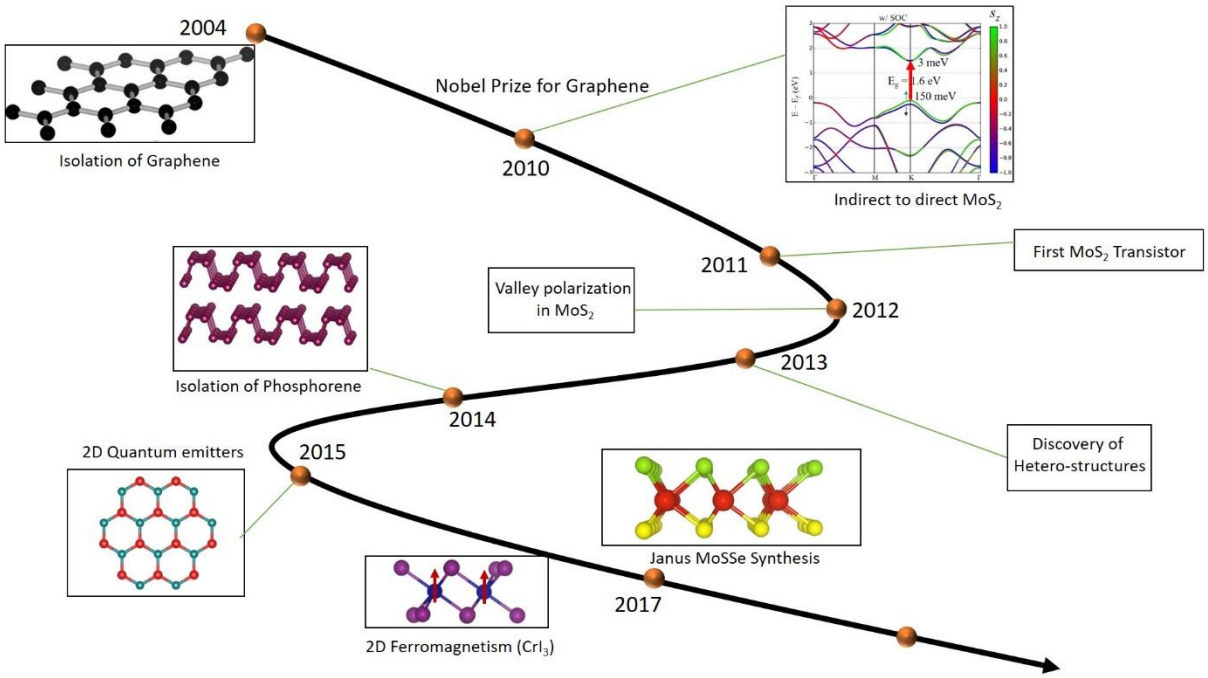

Figure 1. 1 Timeline of major breakthroughs in 2D materials [Details of the discoveries are in Ref. [6,14–21]].

(e.g. $Pb(C_4H_9NH_3)_2I_4$) [22]. In fact, the utilization of data mining approaches reveal that it is possible to exfoliate over 1000 2D materials and several hundreds of 3D materials consisting of weak van der Waals (vdWs) interaction [23–26].

2D materials have shown considerably distinct and sometimes unique properties compared to their host 3D bulk counterparts owing to the quantum confinement effects. Examples include the high mechanical strength (1TPa) and electrical conductivity of graphene [6,27,28], the piezoelectric properties of single-layer MoS_2 and h-BN (hexagonal Boron nitride) [29], an unprecedented high thermoelectric figure-of-merit of 2.6 ± 0.3 in single-crystal SnSe [30–32] at 923 K, the 2D ferromagnetism in exfoliated monolayer CrI_3 [14], the high photocatalytic activity for water splitting of 2D SnS_2 [33,34], the predicted remarkable optical and magnetic properties predicted in doped 2D BN [35], the promising electronic bandgap and band-alignment of 2D dichalcogenide, and monochalcogenide materials for semiconductor and photocatalysis applications [36,37].

There are several prevalent characteristics of 2D layered materials, such as the intra-layer bonding which are typically covalent in nature, whereas adjacent layers are held together by weak vdW forces of interaction. Due to vdW interactions between the weakly stacked layers, methods such as micromechanical exfoliation [38] and liquid-phase exfoliation [39,40] have been developed to obtain atomically thin 2D materials. As the sample size of 2D materials obtained from micromechanical exfoliation processes is usually limited, chemical vapor

deposition (CVD) technique can grow wafer-scale 2D materials on desired substrates [39,40]. In addition, the development of efficient sample transfer methods paved the way for the fabrication of various devices to investigate the physical characteristics of 2D materials.

As 2D materials are devoid of dangling bonds, they can be readily fabricated vertically with a precise sequence control to form vdW heterostructures, regardless of the differences in their incommensurate lattices, lattice constants and crystal symmetry [41]. Vertical 2D heterostructures consisting of distinct single-layers demonstrate some novel electronic [42] and optical properties [43], such as high carrier mobility [18] and ideal photoresponse [44]. Graphene/ TMDC heterostructures provide a rich platform for exploring coupled spin-valley phenomena that offers a new spin manipulation approach based on spin-relaxation anisotropy [45,46]. Such unique characteristics generated by the stacking of different atomically thin materials have opened the opportunities for tuning and engineering new materials for next-generation devices.

1.2 Objective of the thesis

The strong demand for futuristic energy materials and devices are dreadfully increasing owing to the growing consumption of limited and unsustainable fossils fuels, which have been an alarming cause of concern [47–52]. For this reason, serious efforts are being undertaken to explore new materials to realize the desired properties. Figure 1.2 shows the schematic representation of three different kinds of energy conversion processes that have been investigated in 2D TMDC monolayers in the present thesis. A brief overview of the research topics that have been explored individually in the subsequent chapters is as follows.

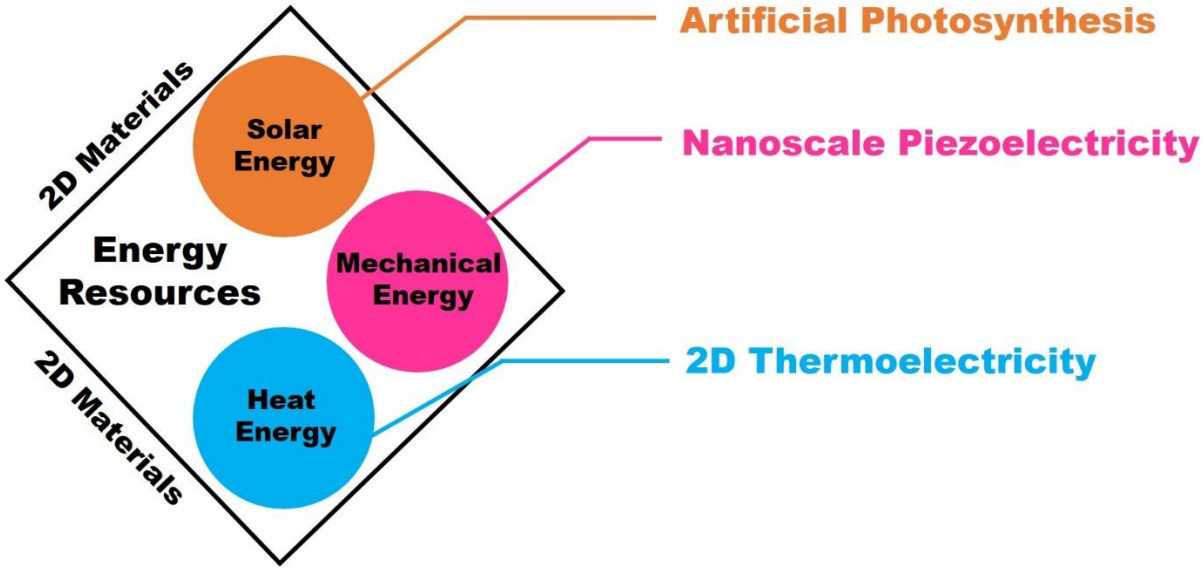

Figure 1. 2 Schematic representation of three kinds of energy conversion investigated in the 2D materials.

1.2.1 Nanoelectromechanical energy conversion

Materials with intrinsic non-centrosymmetric crystal structures and having bandgap allow for the interconversion between electrical energy and mechanical energy [53]. For the first time, in 1880, Pierre Curie and Jacques Curie demonstrated the piezoelectric effect in quartz crystals. Thereafter, a series of piezoelectric materials have been developed which include piezoelectric crystals, such as quartz, GaN, $BaTiO_3$, etc. and piezoelectric ceramics, such as lead zirconate titanate (PZT). Any insulating material which is a member of one of 20 polar crystal classes, out of 32, will be polarized and piezoelectric. However, in order to have a large piezoelectric effect, the crystal should contain the ions with large effective dynamic charges so that a large polarization can occur in response to the application of external lattice strain.

Piezoelectricity is known in bulk 3D materials for long. However, nanoscale piezoelectricity is relatively new. For instance, in 2006, Wang and Song revealed that zinc oxide (ZnO) nanowires behave like small power generators [54]. They continued and developed a whole new field, coined as piezotronics that could harvest power even from the tiny atomic scale movements. The nanoscale piezoelectric materials have a wide range of applications which include flexible and wearable electronics, sensors, actuators, transducers, and energy harvesters in the field of nanorobotics. For such applications, piezoelectric materials are required to be thin, flexible, chemically stable, and biocompatible. These requirements are difficult to be achieved in the conventional piezoelectric ceramics because they have no mechanical flexibility and lack of chemical stability in bio-environment and some of them contain the toxic components. These problems can be overcome with the use of strong, flexible and ultrathin piezoelectric materials. In 2014, the research groups of Wang and Zhang focused on improving the piezoelectric efficiency of the 2D materials by the pioneering studies of piezoelectricity in monolayer MoS_2 [55]. The cationic and the anionic charge centres coincide in monolayers with broken inversion symmetry in hexagonal honeycomb lattices, such as h-BN and MoS_2. The application of tensile (compressive) strain shifts the cationic (anionic) charge centres away from each other along opposite directions along the arm-chair direction, thereby resulting in the piezoelectric constant along the +ve or -ve y direction (arm-chair direction). So far, the reported piezoelectric vdWs layered semiconductors include but not limited to h-BN and TMDCs [56], Group III monochalcogenides (i.e., GaS, GaSe, and InSe) [57], and Group IV monochalcogenides (MX, M=Sn or Ge, X=S or Se) [58]. These layered materials have an inversion symmetry in their bulk structures, which is broken when they are thinned down to a monolayer or a few odd-layers. Moreover, their in-plane piezoelectricity is significantly decreased with the increase of atomic layer number because the reversed polarization directions between adjacent layers results in the cancellation of polarization. Thus,

the highest in-plane piezoelectric coefficient in vdWs layered materials exhibit in their monolayer structure form.

In fact, for the application of atomically thin piezoelectric materials in practical device applications involve some bottleneck issues because the piezoelectric current and voltage outputs are only about dozens of pA and mV, as found in monolayer MoS_2 [59]. Therefore, there is still need to explore new 2D piezoelectric materials or new avenues to bring about high magnitude of polarization and larger piezoelectric output signals together with long-term durability. For instance, in this Ph.D. work, inversion symmetry has been broken in the intrinsically centrosymmetric 1T-MX_2 (M=Zr, and Hf; X=S, Se, and Te) monolayers upon the formation of their Janus structures. As a result, a high level of piezoelectricity has been found to emerge in Janus Group IVB TMDC monolayers along with robust electronic mobility, which has been discussed in detail in Chapter 3. The corresponding schematic has been presented in Figure 1.3. A deeper insight into the mechanism underlying the process of piezoelectricity is provided in Chapter 3.

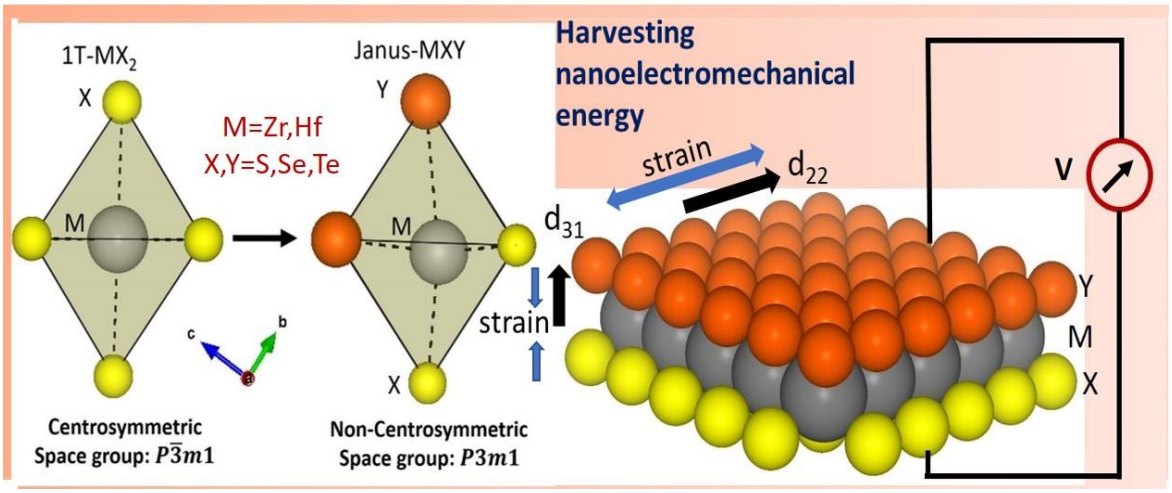

Figure 1. 3 Schematic representation of nanoelectromechanical energy harvesting in Janus structure of Group IVB TMDC monolayers.

1.2.2 Thermoelectric energy conversion

Thermoelectricity has long been recognized as a potentially transformative power generation technology which has been consistently growing due to their ability to convert waste-heat into electricity directly [60–62]. The advantage of such type of energy conversion mechanism is that it does not require any mechanical part. The effective way to enhance $ZT = \frac{S^2\sigma}{k_e+k_L}T$,which is the figure of merit used to characterize the energy conversion performance of thermoelectric materials (TEMs), is to reduce the lattice thermal conductivity (k_L), and the same time maintain

their electronic transport properties [63]-[64]. Ideally, TEMs behave like an "Electron-crystal and Phonon-glass" [65], which means that they can withstand a large temperature gradient across it, while maintaining high electric conductivity (σ) for an efficient thermoelectric energy conversion. In the bulk 3D crystalline semiconductor, S can be greater when the Fermi energy (E_F) close to the band edge as compared to when E_F lies midgap between the conduction and valence band edges. The transport properties are closely related to the electronic states near the CBM and VBM. Light bands facilitate large electrical conductivity, while heavy bands together with large degeneracy can bring about high Seebeck coefficients [66,67]. Therefore, via striking a balance between the two conflicting considerations, a well dispersed conduction/valence bands having a high local curvature along several k-pathways, which show up as multiple narrow peaks in the density of states (DOS), can be highly favourable in enhancing both σ and S simultaneously.

Bulk Bi_2Te_3 and Sb_2Te_3 show low thermal conductivity on account of the heavy atomic mass of the constituent atoms and the smaller difference in mass between the constituents. As a result, the phonons are dispersed over a smaller frequency scale, which provide adequate channels for the propagation of heat (or, thermal transport). This lowers thermal conductivity in these materials. Such understanding helps to design efficient thermoelectric materials in the low dimensions, i.e., nanoscale, as well.

In the past few years, the discovery of two-dimensional (2D) materials have been hogging the limelight owing to their superior thermoelectric properties [68],[69],[70] arising from quantum confinement effects and several other factors: (1) multiply degenerate energy band edges cause localized peaks in the DOS resulting in an enhanced Seebeck coefficient; (2) opportunities to exploit the anisotropic Fermi surfaces in multi-valley semiconductors; (3) pristine surfaces devoid of any surface dangling bonds effectively scatter heat-carrying phonons; (4) increased boundary scattering of phonons at interfaces allow to disentangle the two inversely coupled physical properties (σ and k_L) which limit the thermoelectric performance and (5) anharmonic crystal potential to facilitate the decoupling of σ and k_L. Density of states change with the material dimension. The improvement in thermoelectric properties in low dimensional materials is induced by an enhanced Seebeck coefficient, which arises from the increased density of states, as mentioned in (1). Lowering the dimensionality in materials opens the possibilities for phonon-boundary scattering, which may reduce phonon mean free path and in turn, phonon group velocities and thermal conductivity. Further details on the process of thermoelectricity have been elaborately discussed in Chapter 4.

In this context, the investigations on 2D materials based on chalcogenides (S, Se, and Te) have been boosted-up owing to their very high thermoelectric performance. Bismuth and Antimony based tellurides, such as Bi_2Te_3 [71], Sb_2Te_3 [72], lead chalcogenides(PbS, PbSe, PbTe) [73], tin dichalcogendies (SnS_2, $SnSe_2$) [74],[75],[76],[77], tin monochalcogenides [78],[79] (SnS, SnSe, SnTe), germanium chalcogenide (GeS, GeSe) [80],[81], indium chalcogenide (InSe) [82], ZnO [83], few-layer $PdSe_2$ [84] and transition metal dichalcogenide (TMDC) MX_2 (M=Mo, W, Zr, Hf; X=S, Se, Te) [85],[86],[87], have recently been added to the existing catalogue of 2D thermoelectric materials. Lead chalcogenides are promising thermoelectric materials; however, they are less preferable for mass production due to toxicity issues. The environmental instability of other 2D materials such as phosphorene [88], tellurene [89] has severely undermined the application prospects of the related materials. In a bid to further identify similarly good thermoelectric materials, much research efforts are still required to unleash their unique properties at a fundamental level. In this context, a promising route to enhance the thermoelectric power factor in single layer MoS_2 has been explored, as elaborated in Chapter 4. Besides, the origin of ultralow lattice thermal conductivity (k_L) in Hf-based dichalcogenides and their Janus derivatives have also been ascertained. Such insightful findings will be helpful in the design of thermoelectric materials with a high thermoelectric figure of merit. A more elaborate discussion on the process of thermoelectricity is provided in Chapter 4.

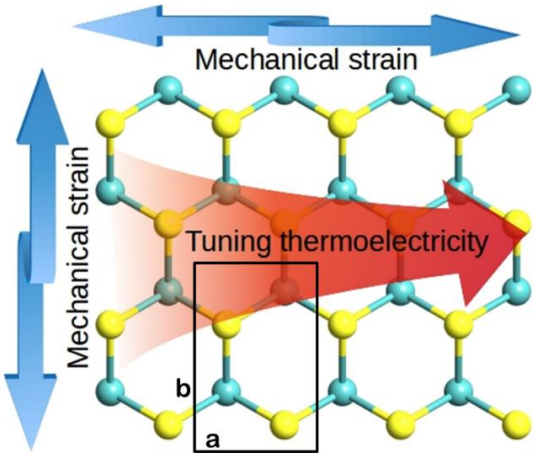

Figure 1. 4 Schematic representation of strain sensitive thermoelectric properties of ML-MoS_2. (Based on the work published in *Journal of Physics: Condensed Matter* 2017, 29, 225501)

1.2.3 Solar energy harvesting

Among various strategies to harness reliable, clean, cheap, green, sustainable and renewable energy; scavenging solar energy [90] has emerged as one the most viable option, e.g., in photovoltaics and water splitting. The most troublesome greenhouse gas, CO_2 is an extremely stable molecule where carbon exists in its highest oxidation state. Returning CO_2 to a useful

state *via* partial or complete reduction is an intricate problem from both scientific and technological perspectives. It requires appropriate catalysts and energy input, thereby posing several fundamental challenges in chemical catalysis, electrochemistry, photochemistry, and semiconductor physics and engineering. Solar water-splitting and CO_2 conversion *via* electrocatalytic reduction of carbon dioxide are already well documented. In 1972, Fujishima and Honda [91] made the first photocatalytic solar cell of semi-conducting TiO_2, where they split water into hydrogen and oxygen using ultraviolet radiation. In the context of such useful pointers, one of the promising avenues turns out to be artificial photosynthesis, which replicates the natural process of photosynthesis, a process where sunlight induces the simultaneous conversion of carbon dioxide and water into carbohydrates and oxygen. Solar Water Splitting [92] and light-driven carbon dioxide reduction [93], which also addresses the natural carbon fixation, has been drawing a surge in research interests. Photo-catalysts based on semiconducting materials is being actively investigated for solar light harvesting in several applications such as water splitting, dye degradation and CO_2 reduction [94–96]. It requires only water and sunlight, supplies of which are almost unlimited.

Band edges need to straddle the redox potentials, as discussed in Chapter 5, for water splitting to be thermodynamically favorable. For instance, for the hydrogen evolution reaction (HER) to be thermodynamically feasible, the HER level or the reduction potential of water should lie below the conduction band edge (CBE) of the semiconducting photocatalytic material. The smaller the difference in energy between the HER level and CBE, higher is the thermodynamic favorability of the HER reaction, as the protons need to draw electrons from the CBE in order to undergo reduction. Similar mechanism underlie the other reactions, such as, CO_2 reduction.

Photo-catalysts powered by sunlight offers the potential of a clean and renewable way to produce fuels and fuel precursors such as H_2, HCOOH, HCHO, CH_3OH, CH_4, *via* simultaneous photoconversion of CO_2 and water. The photocatalytic conversion of CO_2 into liquid fuels, such as, HCOOH, HCHO, and CH_3OH, depending on the varying degrees in reducibility of CO_2, is a crucial goal that would positively impact the global carbon balance by recycling CO_2 into usable fuels. The potential rewards that can accrue from meeting the challenges in artificial photosynthesis are enormous.

Due to quantum confinement effects, reducing the dimensionality is a promising way to tailor the electronic and optical properties of a material. Moreover, the valence band edge (VBE) and conduction band edge (CBE) positions can also be tuned along with other physical parameters [97,98]. In nanosheets, the high surface-to-volume ratio provides more chemically

active sites [99], more efficient light absorption and separation of electron-hole pairs as compared to the corresponding bulk counterparts [100]. Therefore, nanomaterials can potentially serve as new building blocks in constructing light energy harvesting assemblies and in opening up new avenues in utilizing renewable energy sources.

Monolayer MoS_2 is the second highest explored 2D material after graphene because of its outstanding electronic and optical properties. The Chapter no. 5 of Thesis is dedicated to the detailed exploration of the effect of different kind of mechanical strain for the photo-conversion of carbon-dioxide with water into renewable solar-fuels. Additionally, the role pH has been carefully addressed. A more detailed and an insightful analysis on the photocatalysis processes are discussed in Chapter 5.

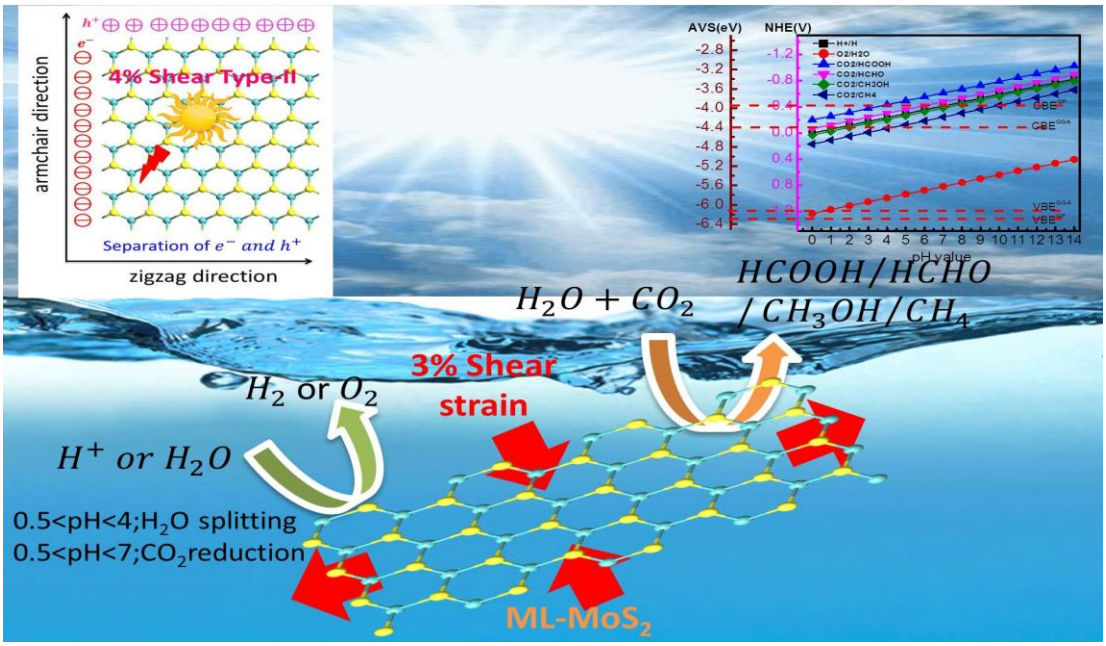

Figure 1. 5 Schematic representation of strain and pH induced optimization of photosynthetic activity in single layer MoS_2.

Chapter 2

Theoretical background

A brief introduction to the theoretical background and methods used in this thesis is described in this chapter.

2.1 Quantum Mechanical Methods

An important shortcoming of classical models lies in their inability to describe the electronic structure of materials which arises from electron interactions. However, in contrast, quantum mechanical models explicitly treat electron interactions by solving the Schrödinger equation, the governing equation of quantum mechanics. This equation can provide the fundamental description of matter at the atomic scale and predicts macroscopic material properties almost exclusively in terms of the interactions of electrons.

Within quantum mechanics, the electronic structure of a material is represented by a wave function Ψ. To determine Ψ, one must solve the *N*-electron Schrödinger equation,

$$\left[-\frac{\hbar^2}{2m}\nabla^2 + V_{II} + V_{Ie} + V_{ee}\right]\Psi(r_1, \dots\dots, r_N) = \varepsilon\,\Psi(r_1, \dots\dots, r_N) \qquad (2.1)$$

The first term on the left represents kinetic energy and V_{II} , V_{Ie} and V_{ee} denote the potential energy arising from ion-ion, ion-electron, and electron-electron interactions, respectively. Most computational techniques expand Ψ in a pre-defined basis-sets functions. Solving for Ψ is then analogous to determining the degree to which each basis function contributes to the overall wave function. The accuracy and cost of the calculation rises with the increase in basis-sets functions. When evaluating the Schrödinger equation, one generally invokes the Born-Oppenheimer approximation [101], which allows ionic and electronic degrees of freedom to be treated separately. Electrons are assumed to respond instantaneously to the fixed potential field generated by stationary ions, which is reasonable since electron dynamics occur on substantially shorter time scales than those of the ionic cores.

2.2 Density Functional Theory (DFT)

The basic idea of DFT is to use the electron density, $n(r)$ as the basic variable instead of the wave function. This simplifies the problem of working with 3*N* spatial variables for a *N*-electron problem to only 3. The first attempts to use density functional is found with the Thomas-Fermi theory (in 1927) [102,103]. This was a density-based theory to deal with many-electron systems. In this model, the kinetic energy density of a many-electron system is approximated by a homogeneous independent electron system with electron density, $n(r)$:

$$T_{TF}[n] = A \int n\,(r)^{5/3} dr \tag{2.2}$$

where $n(r)$ is the electron density of the homogeneous electron gas and A is a constant. The total energy is determined by adding electrostatic energy and interaction with external potential $V_{ext}(r)$ to the kinetic energy, so that

$$E_{TF}[n] = A \int n\,(r)^{5/3} dr + \int n\,(r) V_{ext}(r) dr + \frac{1}{2} \iint \frac{n(r) n(r')}{|r - r'|} dr dr' \tag{2.3}$$

The second term is the electrostatic energy of the ion-electron interaction, and the final term is the classical Hartree-energy. The ground-state density and energy can be obtained by minimizing eq. 2.3 with the constraint of constant electron number N. The original Thomas-Fermi method overestimates the total energy because it does not take into consideration the impacts of exchange and correlation, which always lower the energy.

In conclusion, because of the crude approximation, Thomas-Fermi theory misses important physics of electrons in real materials. However, it provides a simple example of using the electron density as a fundamental variable, which was later developed in DFT.

2.2.1 Hohenberg-Kohn Theorem

Eq. 2.3 shows that the ground-state energy is a functional of both the density and external potential. However, if a mapping between the two physical qualities is established, then the total energy would be the only functional of one of these quantities. That is exactly what was done in 1964 by Hohenberg and Kohn[104]. They proved that DFT can be applied to a system of interacting particles in an external potential $V_{ext}(r)$. The two theorems are as follows.

First theorem: For any system of interacting particles in an external potential $V_{ext}(r)$, the potential $V_{ext}(r)$ is determined uniquely, except for a constant, by the ground-state electron density $n(r)$. This means ground-state electron density determines all properties of the system.

Second theorem: There exists a universal functional $F[n(r)]$ of the electron density, independent of the external field potential, such that the global minimum value of the energy functional $E[n(r)] = \int n(r) V_{ext}(r) dr + F[n(r)]$ is the exact ground-state energy of the system and the exact ground-state density $n_0(r)$ minimizes this functional. So the exact ground-state energy and density are fully determined by the functional $E[n(r)]$.

The Hohenberg-Kohn theorems formulate the quantum many body problem in terms of the electron density $n(r)$ as the basic variable. But in practice, it is still impossible to calculate any property of a system because the universal functional $F[n(r)]$ is unknown. This leads to the Kohn-Sham approach, which assumes the ground-state density of the interacting system to be

that of a fictitious non-interacting system with all the difficult many-body terms incorporated into the exchange correlation functional of the charge density. While the exact exchange-correlation functional is still unknown, various approximation can be made, allowing for a practical implementation of DFT within the Kohn-Sham framework.

2.2.2 The Kohn-Sham Ansatz

In 1965, based upon Hohenberg-Kohn theorem, Kohn and Sham [105] introduced a method to minimize the energy functional $E[n(r)]$ with respect to charge density to find the ground state energy under the constraint that the total number of electrons is constant:

$$\frac{\delta}{\delta n(r)}\left[E[n(r)] - \mu \int n(r)dr\right] = 0 \tag{2.4}$$

where μ is a Langrange multiplier. The corresponding Euler equation is:

$$\frac{\delta E[n(r)]}{\delta n(r)} = \mu \tag{2.5}$$

Kohn and Sham separated $F[n(r)]$ into three parts, so that $E[n(r)]$ becomes

$$E[n(r)] = T[n(r)] + \frac{1}{2}\iint \frac{n(r)n(r')}{|r-r'|} + E_{XC}[n(r)] + \int n(r)V_{ext}(r)dr \tag{2.6}$$

where $T[n(r)]$ is defined as the kinetic energy of a non-interacting electron gas with electron density $n(r)$.

Rewriting Eq. 2.5 in terms of an effective KS potential, $V_{KS}(r)$, as follows

$$\frac{\delta T[n(r)]}{\delta n(r)} + V_{KS}(r) = \mu \tag{2.7}$$

where

$$V_{KS}(r) = V_{ext}(r) + \frac{\delta E_H[n(r)]}{\delta n(r)} + \frac{\delta E_{XC}[n(r)]}{\delta n(r)} \tag{2.8}$$

$$= V_{ext}(r) + V_H(r) + V_{XC}(r)$$

and

$$V_H(r) = \int \frac{n(r')}{|r-r'|}dr' \tag{2.9}$$

Now, if we consider a system that is truly of non-interacting electrons with an external potential equal to $V_{KS}(r)$, then the same analysis would lead to exactly the same Eq. 2.7. To find the ground-state energy and density of such a system, one has to solve the one-electron equation

$$\left(-\frac{1}{2}\nabla^2 + V_{KS}(r)\right)\Psi_i(r) = \varepsilon_i\,\Psi_i(r) \tag{2.10}$$

where $\Psi_i(r)$ is the one-electron wavefunction. The electron density is then determined by

$$n(r) = \sum_{i=1}^{N} |\Psi_i(r)|^2 \tag{2.11}$$

Equations (2.8), (2.10) and (2.11) have to be solved self-consistently because $V_{KS}(r)$ depends on the density through the exchange-correlation potential $V_{XC}(r)$ and Hartree potential $V_H(r)$, and the density depends on the wave-function. So far, the Kohn-Sham approach has mapped the original interacting system to a non-interacting system with an effective Kohn-Sham single particle $V_{KS}(r)$, and the two systems have the same ground state density.

In practice, the Kohn-Sham approach is an approximation to the original many-body problem because the exchange-correlation functional $E_{XC}[n(r)]$ is unknown. In order to obtain a satisfactory description of a real system, it is important to have an accurate functional $E_{XC}[n(r)]$.

Two of the most widely used approximations for the exchange-correlation potential are the local density approximation (LDA) [105] and the generalized gradient approximations (GGA) [106].

2.2.3 Exchange-correlation functional

In the LDA, the exchange-correlation energy per electron at a point r is taken to be the same as that for a homogeneous electron gas with density equal to that at point r. The exchange-correlation functional $E_{XC}[n(r)]$ can then be expressed as

$$E_{XC}^{LDA}[n(r)] = \int n(r)\epsilon_{XC}^{hom}n(r)dr \tag{2.12}$$

$$= \int n(r)[\epsilon_X^{hom}(n(r)) + \epsilon_C^{hom}(n(r))]dr$$

$$= E_X^{LDA}[n(r)] + E_C^{LDA}[n(r)]$$

The exchange energy functional $E_X^{LDA}[n(r)]$ can be written analytically using the result for the homogeneous electron gas:

$$E_X^{LDA}[n(r)] = \int n(r)\epsilon_X^{hom}n(r)dr \tag{2.13}$$

$$= -\frac{3}{4}\left(\frac{3}{\pi}\right)^{1/3}\int n(r)^{4/3}dr$$

where

$$\epsilon_X^{hom} = -\frac{3}{4}\left(\frac{3}{\pi}\right)^{1/3} n(r)^{1/3} \quad (2.14)$$

is the exchange energy density. Analytical expression for the correlation energy functional $E_C^{LDA}[n(r)]$ in the homogeneous electron gas is unknown except in the high- and low-density limits. Most LDA formulas use analytic forms for ϵ_C, fit to accurate quantum simulation results of the correlation energy at intermediate density, and reproduce the exact result at the high- and low-density limits.

In principle, the LDA should work best in systems where the density varies slowly. In fact, it turns out to work surprisingly well even in some systems where the electron density is rapidly varying. In general, the LDA tends to underestimate bond-length by 1-2% [107], overestimate binding energies by 10-50% [108,109], and underestimate band gaps by ~50% [110].

The XC energy of an inhomogeneous electron density can be significantly different from that of a homogeneous electron gas. The GGA addresses this problem by allowing the functional to depend on not just the local density, but the local gradient of the density as well. It generally works better than LDA in predicting bond lengths, crystal lattice constants, binding energies, and so on, but often overcorrects. As 2D semiconductors have been studied in the thesis, it is important to discuss the description of semiconductors in DFT, which is a ground state theory. The conduction and valence bands correspond to the excited state of electrons and holes respectively and therefore, DFT does not provide an adequate description of the excited states. As a result, DFT underestimates band gaps, which is well known. Nevertheless, GGA is very good at predicting the trends, e.g., the variation in band gap with strain, thereby substantiating the reliability of GGA. Hybrid functionals have also been employed in the thesis to obtain more accurate band gaps and band edge positions, which are particularly, useful in photocatalytic studies.

2.2.4 Hybrid exchange- correlation functional

In the standard DFT, both the exchange E_X and the correlation E_C energies are treated by a local or semilocal approximations. The errors in the self-interaction and lack of derivative discontinuity present in the local functional leads to the underestimation of electronic bandgaps. However, Hartree-Fock method overestimates bandgaps significantly, which is attributed to the lack of correlation; and the experience of repulsive Hartree potential only by the unoccupied orbitals. Thereafter, a more robust hybrid approach came into being, which was conceptualised by Becke in 1993 [111]. The approach relies on the adiabatic connection proposed by Harris [112] and compared to the standard vanilla function in which a

fraction of the local exchange is replaced by the non-local Fock exchange operator.

In general, the exchange-correlational energy functional for hybrids is written as follows:

$$E_{XC}^{hyb} = aE_X^{local} + (1-a)E_X^{nl} + E_C^{local}$$

where $local$ refers to a (or mix of) vanilla type functional nl is the non-local Hartree-Fock exchange. The mixing parameter a determines how much of the non-local exchange is used in the functional. In parts of present thesis work, HSE06 functional has been used, in which 25% of the short-range exchange interaction of the PBE-GGA has been replaced by the short-range non-local Hartree-Fork exchange interaction [113,114].

2.2.5 Solving Kohn-Sham Equations

The KS equations must be solved self consistently because the KS potential $V_{KS}(r)$ and the electron density $n(r)$ are related. Usually these equations are solved by starting with an initial guess for the electron density. For example, the initial guess could be a superposition of atomic electron densities. Thus, the KS potential $V_{KS}(r)$ is calculated and Eq. 2.10 is solved to obtain the one-electron eigenvalues and wave functions. Given the wave functions, a new electron density is calculated. For stability, the calculated electron density is often mixed the electron density from the previous iteration to get a new density for the next iteration. The KS equations with the new V_{KS} are solved again to obtain the next round of electron density. The iteration continues until a pre-set level of self-consistency is reached. For example, if the change of total energy or electron density between two iterations is smaller than some specified convergence criteria, then after various quantities of interest can be determined.

2.2.6 Plane Waves and Pseudopotential

To solve KS equations, one needs to expand the wave functions in a basis-sets. Plane-wave basis-sets provide a simple unbiased choice of basis-sets in periodic solids and 2D materials. According to the Bloch theorem, the Eigen-functions of the KS equations with wave vector **k** can be written as:

$$\Psi_k(r) = e^{ik.r}\mathrm{u}_k(r) \qquad (2.15)$$

where $\mathrm{u}_k(r)$ is a periodic function with crystal periodicity and it can be expanded in a Fourier series as follows:

$$\mathrm{u}_k(r) = \frac{1}{\sqrt{\Omega}}\sum_G c_k(G)\, e^{iG.r} \qquad (2.16)$$

where G is a reciprocal lattice vector, Ω is the crystal unit cell volume, $c_k(G)$ is the expansion coefficient, and $e^{iG.r}$ is a plane-wave vector G. So, the eigen-function $\Psi_k(r)$ can be expanded

in plane-wave basis as:

$$\Psi_k(r) = \frac{1}{\sqrt{\Omega}} \sum_G c_k(G)\, e^{i(k+G).r} \qquad (2.17)$$

As it is the valence electrons that are significant for the chemical interactions, therefore, it is convenient to treat only valence-electrons, and to use pseudopotentials to represent the interaction between valence-electrons and ion-cores only. In addition, pseudopotential wave-functions are constructed to match the true atomic valence wave-function beyond a given radius, but within the core region they can be much smoother than atomic wave functions. This means that the number of plane-waves needed to expand the wave-function can be significantly reduced. With a plane-wave basis, the accuracy of the calculation can be improved in a systematic and unbiased way by increasing the size of the basis set.

2.3 Density Functional Perturbation Theory (DFPT)

DFPT methods are popular because they can be easily implemented to determine the various important physical parameters which includes the linear response properties and lattice dynamics studies, directly without the need for multiple ground-state calculations. The different types of perturbations that generally includes in DFPT calculations depends upon the response *via* ionic displacements, lattice strain and electric field effects [115]. DFPT methods allow the calculations of corresponding properties such as phonon-dispersion spectra, elastic-stiffness tensors, and dielectric polarization within the DFT framework. Furthermore, DFPT have been shown to give a successful description of the dielectric and piezoelectric properties of a wide range of materials in which electronic correlations are not too strong [116,117]. Therefore, DFPT approach provides the desired response properties in a more systematic, and reliable manner.

2.3.1 Linear response within the Kohn-Sham scheme

The linear response within the DFT[116] scheme can be obtained by standard perturbation techniques under the condition that the effective potential $V_{eff}(r)$ entering in the Kohn-Sham equations depends on the ground-state density itself. Thus, its linear variation is given by:

$$\delta V_{eff}(r) = \delta V_{ext}(r) + \delta V_{scr}(r) = \delta V_{ext}(r) + \int d^3r' I(r,r')\, \delta n(r') \qquad (2.18)$$

$$I(r,r') \equiv \frac{\delta V_{scr}(r)}{\delta n(r')} = \frac{\delta V_H(r)}{\delta n(r')} + \frac{\delta V_{XC}(r)}{\delta n(r')} \qquad (2.19)$$

This induces a first-order variation of the single-particle wave-functions

$$\delta\psi_i(r) = \sum_{j(\neq i)} \frac{< j|\delta V_{eff}|i >}{\epsilon_i - \epsilon_j}\psi_j(r) \tag{2.20}$$

By using a similar expression for $\psi_i{}^*(r)$ gives

$$\delta n(r) = \sum_{i\neq j} \frac{f_i - f_j}{\epsilon_i - \epsilon_j} < j|\delta V_{eff}|i > \psi_i{}^*(r)\psi_j(r) \tag{2.21}$$

Equations (2.19) and (2.21) must be solved self-consistently to obtain the first order variation of the density.

2.3.2 Lattice dynamics approach

For the case of lattice vibrations or phonon studies[116], this perturbation corresponds to the ionic displacements. The standard perturbation is applied to the Kohn-Sham equations. Using the Hellmann-Feynman theorem for the electron density, it is assumed that the potential, subject to small perturbation can be expressed in the form of Talyor expansion:

$$V_\lambda(r) = V_0(r) + \lambda\frac{\partial V}{\partial \lambda} + \lambda^2\frac{\partial^2 V}{\partial \lambda^2} + \cdots \tag{2.22}$$

And the perturbed electron density n(r) and wave-function become

$$n_\lambda(r) = n_0(r) + \lambda\frac{\partial n}{\partial \lambda} + \lambda^2\frac{\partial^2 n}{\partial \lambda^2} + \cdots \tag{2.23}$$

$$\psi_\lambda(r) = \psi_0(r) + \lambda\frac{\partial \psi}{\partial \lambda} + \lambda^2\frac{\partial^2 \psi}{\partial \lambda^2} + \cdots \tag{2.24}$$

Evaluation of the first order terms results in the first-order Schrodinger equation also leading to the Hellman-Feynamn theorem which states that the expectation value of the derivative of the Hamiltonian gives the derivative of the eigenvalues of the Hamiltonian.

$$\frac{\partial E}{\partial \lambda} = < \psi \left|\frac{\partial H}{\partial \lambda}\right| \psi > \tag{2.25}$$

Using the Hellman-Feynman theorem and doing a perturbation expansion to the first order in the electron density, we arrive at an expression for the total energy of the perturbed system:

$$E = E_0 + \sum_i \lambda_i \int n_0(r)\frac{\partial V(r)}{\partial \lambda}dr + \frac{1}{2}\sum_{i,j}\lambda_i\lambda_j \int \left(\frac{\partial n(r)}{\partial \lambda_i}\frac{\partial V(r)}{\partial \lambda_j} + n_0\frac{\partial^2 V(r)}{\partial \lambda_i \lambda_j}\right)dr \tag{2.26}$$

When comparing this expression with the Taylor series expansion of the total energy

$$E = E_0 + \frac{1}{2}\sum_{L,L'}\sum_{i,j} u_i(R_L)u_j(R_{L'})C_{i,j}(R_L, R_{L'}) \tag{2.27}$$

We can identify the second order term connected to the force constants and write as:

$$C_{i,j}(R_L, R_{L'}) = \int \left(\frac{\partial n(r)}{\partial u_i(R_L)} \frac{\partial V(r)}{\partial u_j(R_{L'})} + n_0 \frac{\partial^2 V(r)}{\partial u_i(R_L)\partial u_j(R_{L'})} \right) dr \tag{2.28}$$

here only the 1st order perturbations to the electron density are needed. Further details are available in the reference [116].

Chapter 3

Nanoelectromechanical energy harvesting in Group IVB Janus transition metal dichalcogenide monolayers

Based on the work published in:

Dimple, Nityasagar Jena, Ashima Rawat, Raihan Ahammed, Manish Kumar Mohanta, and Abir De Sarkar, "Emergence of high piezoelectricity along with robust electron mobility in Janus structures in semiconducting Group IVB dichalcogenide monolayers", **J. Mater. Chem. A** 2018, 6, 24885-24898

3.1 Introduction

It is well documented that the semiconducting band gap in MoS_2, one of the most widely studied 2D materials, widens and becomes direct when its thickness is reduced to the level of a monolayer [118]. Interestingly, when bulk MoS_2 is thinned down to the scale of a monolayer, the inversion symmetry in the crystal lattice is broken. As a result, piezoelectricity manifests itself in non-centrosymmetric single-layer MoS_2. Theoretical predictions have preceded experimental confirmation or realization, in many instances. It turns out that piezoelectricity in single layer MoS_2 was first predicted theoretically using first principles based density functional theory calculations [29] and later observed experimentally [55,59]. Since then, piezoelectric properties at the nanoscale, and particularly in 2D materials, have seen a surge in research interest. Alyörük *et al* [119] reported the promising piezoelectric properties of the 1H-phase of Group-IV and VI dichalcogenides and their respective oxides. Lidia *et al* [120] predicted a much higher piezoelectric effect in Group-IV monochalcogenides as compared to hexagonal BN sheets and TMDCs. Ruixiang *et al* [121] predicted enormous anisotropy in the piezoelectric effects in monolayers of Group-IV monochalcogenides such as SnSe, SnS, GeS, GeSe. Huabing *et al* [122] reported extremely high piezoelectric values in hexagonal phase of Group-V binary compounds. Simultaneous occurrence of semiconducting and piezoelectric properties in these nanostructures may induce multifunctionality in them through a synergic coupling between these properties, thereby enabling their potential applications in piezoelectric/piezotronics [59,123], piezophototronics [124] and piezophtotocatalysis [125–127]. Piezoelectricity at the nanoscale is in its infancy and at the level of fundamental research. The insight into the origin of piezoelectricity and its possible merger with other properties needs to be deepened in order to bridge the gap between the current understanding and its implementation in these envisioned practical applications.

Group VI TMDCs have been widely studied from both scientific and application perspectives. The nature of the bonds in these monolayers is polar and covalent. The valence and conduction band edges in these monolayers arise from the hybridization of the metal d-states with the chalcogen p-states. As a result, these 2D monolayers show a direct band gap in their equilibrium lattice structures. The monolayers have also been manipulated both out of scientific interest and for the utilization of properties emanating from it. For instance, substituting the entire upper atomic layer of chalcogen in these monolayers by an atomic layer of another chalcogen introduces the so-called Janus phase, which can bring about new capabilities or functionalities in these layered 2D materials. These type of two-faced structures have been theoretically [128,129] predicted first and then experimentally [15,130] realized in Group-VI TMDCs. Ang-Yu Lu *et al* [131] proposed an innovative synthetic strategy in

synthesizing Janus structures in transition metal dichalcogenides. Zhang *et al* [130] also obtained monolayer Janus SMoSe flakes by well-controlled sulfurization of monolayer $MoSe_2$. Seok *et al*[132] suggested telluriding monolayer MoS_2 and WS_2 *via* alkali metal scooter. Yu *et al*[129] predicted the enhancement in the piezoelectric effect in Janus structures in Group-III (Ga, In) monochalcogenides with respect to their non-Janus [57] structures. Moreover, the breaking of symmetry in the out-of-plane direction could also lead to many applications such as a basal-plane active 2D photocatalysis [133],[134],[135], Rashba-type spin splitting [136],[137],[15], ferromagnetism[138] & robust pieoztronic devices at the 2D or nano level.

The successful experimental [139–141] isolation of atomically thin semiconducting 1T-MX_2 monolayers of Group IVB dichalcogenides has lately attracted a good deal of scientific interest[142]. Due to their semiconducting band gaps together with an appreciable carrier mobility, these monolayers are promising candidates in low-power electronic devices [143]. These type of 2D transition metal dichalcogenide (TMDC) monolayers are completely different from Group VI TMDCs in terms of electronic structure [144]. The interatomic bonds in these monolayers are predominantly of ionic nature. The valence band states are primarily constituted of chalcogen p-states, while the conduction band states are composed of metal d-states. As the band edges are decoupled, the band gaps turn out to be indirect. Furthermore, a parallel-band feature, which is a characteristic of van Hove singularity is induced in the absorption spectra. As a result, strong light-matter interaction is found in Group IVB dichalcogenide monolayers [145]. Moreover, the Group IVB dichalcogenide monolayers are centrosymmetric and, therefore, do not exhibit piezoelectric properties.

In the present chapter, the Janus structures of 1T-MX_2 (M=Zr, and Hf; X=S, Se, and Te) monolayers have been investigated. Inversion symmetry is broken in these 2D Janus structures, which causes the occurrence of piezoelectricity. Piezoelectric material needs to be an insulator or semiconductor with a reasonable band gap in order to avoid current leakage. Therefore, these Janus structures in 1T-TMDC monolayers satisfy this criterion as well. Inversion symmetry broken by the introduction of Janus structure adds a new dimension to piezoelectricity in 2D materials on account of the origin of piezoelectricity in these layered semiconducting nanosheets, which is ionic in nature, in contrast to the electronic nature of piezoelectricity in 2D layered materials studied so far [57,119,146,147]. Although high values of piezoelectricity have been reported for layered materials; however, their carrier mobility has either not been reported or found to be low. Here, Group IVB based Janus structures in monolayers exhibit high piezoelectricity along with robust electronic mobility. The formation of Janus structures breaks the inversion symmetry and induces in-plane as well as out-of-plane

piezoelectricity. Additionally, on account of lower elastic constants in Group IVB based dichalcogenides with respect to Group VI dichalcogenides, significantly high piezoelectric strain coefficient can be speculated.

The present chapter is organized as follows. First of all, the consequences of the reduction in symmetry brought about in the Janus monolayers with respect to the native 1T structure has been discussed. Thereafter, the origin of piezoelectricity has been ascertained and the piezoelectric strength has been ascribed to related parameters such as Born effective charges and elastic stiffness constant. The dynamical stability of these monolayers has also been confirmed by phonon dispersion calculations. Then, the effect of decoupled band edges on the relative magnitude of deformation potential for holes and electrons and that of the anisotropy in carrier effective mass and deformation potential on carrier mobility has been thoroughly investigated for their potential applications in nanopiezotronics.

3.2 Computational Details

First-principles calculations have been carried out using density functional theory (DFT) as encoded in the Vienna Ab-initio Simulation Package (VASP 5.3) [148–150]. The Perdew-Burke-Ernzerhof (PBE) [151] variant of the generalized gradient approximation (GGA)[106] has been used for the exchange correlational functional, while projected augmented wave (PAW) potentials have been employed to describe the interaction between the electrons and ions. In some part of the calculations, the screened hybrid Heyd-Scuseria-Ernzerhof 2006 (HSE06) functional [113,114] has been adopted to secure accurate electronic structures as GGA-PBE exchange correlation functional is known to underestimate the band gap in semiconductors. The electronic wave functions have been expanded within the energy cut off of 500 eV. Both atomic positions and lattice constants have been fully relaxed using the conjugate gradient method. Atomic relaxations have been performed until the Hellmann–Feynman forces on each atom reduced to values below 0.01 eV $Å^{-1}$. The total energy convergence criterion between successive self-consistent cycles was set at 1 $x10^{-4}$ eV. A 7×7×1 Monkhorst-Pack k-mesh sampling have been used to optimize the geometries. A vacuum thickness of more than 13 Å along the z-direction has been adopted to minimize the spurious interactions between the periodic images to a negligible level. In HSE06 functional, 25% of the short-range exchange interaction of the PBE-GGA has been replaced by the short-range non-local Hartree-Fork exchange interaction. For this study, an exchange-screening range separation parameter, ω of 0.2 $Å^{-1}$ was set. To confirm the dynamic stability, the phonon dispersion calculations have been performed within density functional perturbation theory (DFPT) [116], as implemented in the Phonopy code [152]. The relaxed-ion elastic stiffness

coefficients, C_{ijkl}, including both the ionic and electronic components, have been calculated by using a finite difference method, as implemented in the VASP code. The static dielectric constants and Born effective charge tensors have been computed based on the linear response theory. The relaxed-ion piezoelectric stress coefficients have been obtained as the sum of ionic and electronic contributions by using DFPT method as incorporated into VASP [115]. Within DFPT, the VASP code directly gives the electronic and ionic contribution to the piezoelectric stress coefficient.

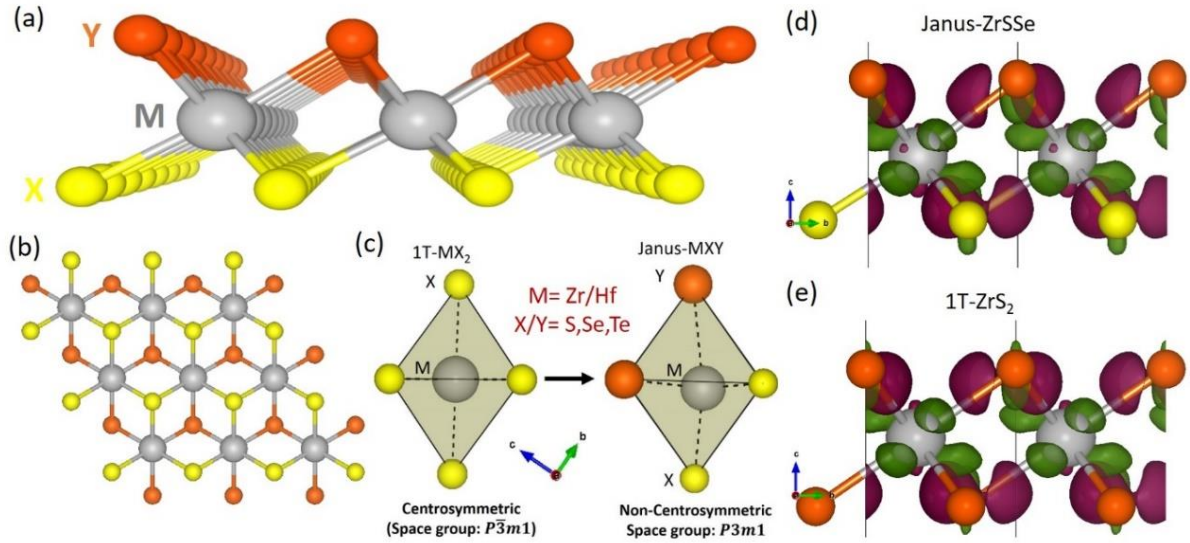

Figure 3. 1 (a-b) Side and top view of Janus structures in semiconducting Group IVB MXY (M= metal; X/Y= chalcogen) monolayers in 1T-phase, (c) the lattice of the Janus structure is devoid of the centre of inversion and hence, exhibits piezoelectricity. Octahedral coordination of the metal atom with chalcogen atoms, i.e., each M atom coordinates with six chalcogen atom in this trilayer structure. For 1T-MX_2, M lies exactly at the centre of this octahedron. However, in Janus structures, M shifts off from the centre of the octahedron and thereby breaks the inversion symmetry. (d)-(e) Bonding charge density of the Janus-ZrSSe and 1T-ZrS_2 monolayer, obtained from the difference in the valence charge density between the monolayer and the superposition of the valence charge density of the neutral constituent atoms. Magenta and green colours indicate regions of electron accumulation and depletion respectively.

3.3 Results and Discussion

3.3.1 Breaking inversion symmetry in centrosymmetric 1T monolayers

Structurally, monolayers of 1T-MX_2 (M=Zr and Hf; X=S, Se, and Te) are similar to those of 1T-CdI_2 [139],[153]. They belongs to a centrosymmetric space group $P\bar{3}m1$ (164). The monolayers have been recently synthesized experimentally [154],[139]-[140]. MX_2 contains a planar M layer sandwiched between two planar X layers, forming a trigonal structure when projected onto the (001) plane. Dynamic and thermodynamic stabilities have been confirmed by carrying out phonon dispersion (see Figure 3.2) and cohesive-energy calculations, as shown

in Table 3.1. All compounds crystallize in the CdI_2 (1T) polytype with octahedral metal coordination, resembling the 1H-MoS_2 structure but with top and bottom layers of chalcogen atoms staggered relative to one another. MX_2 in the 1T phase has an inversion centre at the M atomic sites and belong to the D_{3d} point group. To construct the Janus structure of monolayer 1T-MX_2, the top or the bottom layer of X atoms need to be replaced by the Y atoms, yielding 1T-MXY monolayers, as shown in Figure 3.1 (a). In such a manner, six Janus monolayer structures, ZrSSe, ZrSTe, ZrSeTe, HfSSe, HfSTe and HfSeTe, have been generated.

Experimentally, careful control of heating allows to replace the sulphur atoms in the top planar layer by selenium atoms in the two-dimensional materials [15,130]. Calculations reveal that 1T-phase belongs to centrosymmetric space group whereas the Janus phase belongs to the non-centrosymmetric space group. Polar Janus MXY monolayers possesses trigonal P3m1 (156) space group symmetry. This polar structure is characterized by the absence of mirror planes that are perpendicular to the c-axis. Also, as evident from Figure 3.1, symmetry is lowered in the Janus monolayer structures relative to their 1T pristine monolayers, as the Janus monolayers contain only 6 symmetry operations, while the pure 1T- phase contains 12 symmetry operations.

To visualize the hybridization of electronic states between the transition metal and chalcogen atoms, the electronic charge density distribution has been calculated. The charge density (as shown in Figure 3.1 (d and e) in the bonding states is obtained as the difference between the valence charge density of the MX_2 or MXY nanosheet and the non-interacting electron charge density calculated from a superposition of the valence charge density of the free atoms. This agrees with the earlier reports[155]. Magenta and green colors indicate regions of electronic charge accumulation and depletion respectively. As the lower and upper chalcogen atoms are staggered with respect to each other in 1T-MX_2 and its Janus MXY monolayer, the bonding charge distribution is different from that of 1H-MX_2 or its MXY Group-VI TMDC monolayers where electronic charge accumulation occurs around the centre of the M-X bond, indicating the covalent character of M-X bond[128,156,157]. However, for 1T-MX_2 TMDC monolayers and thier Janus MXY monolayers, the bonding charge distribution is different. Electronic charge accumulation takes place symmetrically around the chalcogen atoms both in the upper and lower layer in 1T-MX_2, whereas for the Janus structures the electronic charge distribution is non-symmetrical. This implies the ionic character of the interatomic bonds in pristine 1T-structures and a mixture of ionic and covalent bonds in the Janus structures. Furthermore, in the Janus monolayers, the difference in the atomic sizes and electronegativities in X and Y atoms gives rise to inequality in the

bond lengths, M-X and M-Y, and in turn, the charge distribution, as shown in Figure 3.1 (d) and (e). More charges are transferred from Zr to S than from Zr to Se, as shown in Fig. 1 (d) and (e) and in Table 3.2. This imbalance breaks the inversion symmetry between the top layered X and bottom layered Y atoms centred on M atom (moreover, in pristine 1T-TMDC monolayers, top and bottom layered X atoms are staggered relative to each other and not vertically aligned, as in 1H-phase), resulting in a lower degree of $3m$ symmetry, instead of $\bar{3}m$, as found in the conventional 1T-MX_2 monolayers. Furthermore, the M/X atom has nominal ionic charge of +4/-2 in the neutral state, however the effective atomic charge was computed to be +2.05e/-1.025e and +1.945e/-1.053e/-0.891e for Zr/S and Zr/S/Se in ZrS_2 and ZrSSe monolayers respectively, according to the Bader charge population analysis, indicating that the bonding between Zr and S is a mixture of covalent and ionic character. Details of Bader charges on each ionic species for all monolayers can be found in Table 3.2.

Table 3. 1 Optimized structure of 2D monolayer nanosheets (2D-NS): lattice constant: a (Å), bond-lengths: d_{M-X} (Å) and d_{M-Y} (Å), bond angle: θ_{X-M-Y} (°), cohesive energy per unit cell, $E_c(eV)$, charge transferred from the metal atom, $\Delta Q_M(e)$ and vertical dipole moment, $\mu_\perp(Debye)$

2D-NS	a	d_{M-X}	d_{M-Y}	$\theta_{X-M-X/Y}$	E_c	ΔQ_M	$\mu_\perp$
ZrS_2	3.69	2.58	--	88.8	-4.62	2.05	0
$ZrSe_2$	3.75	2.69	--	91.4	-3.91	1.86	0
$ZrTe_2$	3.96	2.91	--	94.0	-3.23	1.56	0
ZrSSe	3.73	2.55	2.72	89.7	-4.28	1.95	0.33
ZrSeTe	3.92	2.7	2.94	91.3	-3.69	1.72	0.64
ZrSTe	3.82	2.56	2.94	90.6	-4.59	1.80	1.05
HfS_2	3.65	2.56	--	88.8	-4.73	2.24	0
$HfSe_2$	3.72	2.68	--	91.8	-3.98	2.05	0
$HfTe_2$	3.97	2.9	--	93.4	-3.36	1.73	0
HfSSe	3.68	2.54	2.69	90.3	-4.35	2.13	0.34
HfSeTe	3.87	2.67	2.91	91.5	-3.71	1.87	0.56
HfSTe	3.75	2.53	2.9	91.2	-3.89	1.94	1.03

Table 3. 2 Effective charges on atomic species calculated *via* Bader population analysis

MX2	M	X	X
ZrS_2	+2.0505	-1.0259	-1.0246
$ZrSe_2$	+1.8635	-0.9316	-0.9318
$ZrTe_2$	+1.564	-0.7818	-0.7822
HfS_2	+2.2439	-1.1244	-1.1195
$HfSe_2$	+2.0522	-1.029	-1.0233
$HfTe_2$	+1.7396	-0.8696	-0.8700

MXY	M	X	Y
ZrSSe	+1.9452	-1.0538	-0.8913
ZrSTe	+1.8023	-1.0858	-0.7165
ZrSeTe	+1.7241	-0.9676	-0.7565
HfSSe	+2.1343	-1.1476	-0.9866
HfSTe	+1.9477	-1.1623	-0.7854
HfSeTe	+1.8789	-1.0483	-0.8306

In addition to these properties of Janus strcutures, it is interesting to know the intrinsic dipole moment perpendicular to the plane of nanosheet ($\mu_\perp$), which is calculated by resolving the vector components of the dipole moment. All the Janus monolayer structures show an out-of-plane dipole moment which is zero in their pristine 1T-phase. The calculated results, tabulated in Table 3.1, show a large dipole moment and an electric field perpendicular to the plane of Janus 2D sheet, as compared to the dipole moment, in Group-VI Janus structure[133,134].

3.3.2 Dynamical stability

Even if the total energy of a structure is minimized, its stability cannot be assured. Therefore, frequencies of the vibrational modes of optimized single-layer MX_2 or MXY in 1T or Janus structures have been calculated along the high-symmetry k-points in the BZ to provide a rigorous test for the stability. A structure is taken to be stable only when calculated frequencies of all phonon modes in the BZ are positive; otherwise, imaginary frequencies indicate instability. In such calculations, the long wavelength, out of plane acoustical (ZA) modes are vulnerable to instability. Thus, caution has to be taken in calculating forces with extreme accuracy.

To confirm the dynamical stability, phonon dispersions of 1T-MX_2 and their Janus MXY monolayers have been calculated by using the density functional perturbation theory (DFPT). The results are plotted in Figure 3.2 for all Janus MXY and also for 1T-MX_2 monolayers. No appreciable imaginary vibrational frequency is noticed in the first Brillouin zone, which clearly suggests that monolayers are dynamically stable. Except a small pocket near the Γ point, no trace of imaginary frequencies is observed in the Brillouin zone. This small pocket of instability is extremely sensitive to the details of the calculation and in some cases, it disappears altogether. This suggests that it merely indicates the difficulty in achieving numerical convergence for the flexural phonon branch, which appears to be a common issue in the first principle calculations

for 2D materials [158]. The existence of small regions of phonon instability in the flexural acoustic (ZA) modes around the Γ point has also been observed in graphene, silicone, molybdenum disulfide and gallium chalcogenides. The region of instability shows extreme sensitivity to simulation parameters such as supercell size and k-point sampling. Moreover, the absolute values of the imaginary frequencies are close and vary by the amount by which the acoustic branches of the dispersion curve miss zero when Newton's third law is not imposed on the matrix of the force constants. For these reasons, it is understood that these regions of instability are spurious [158].

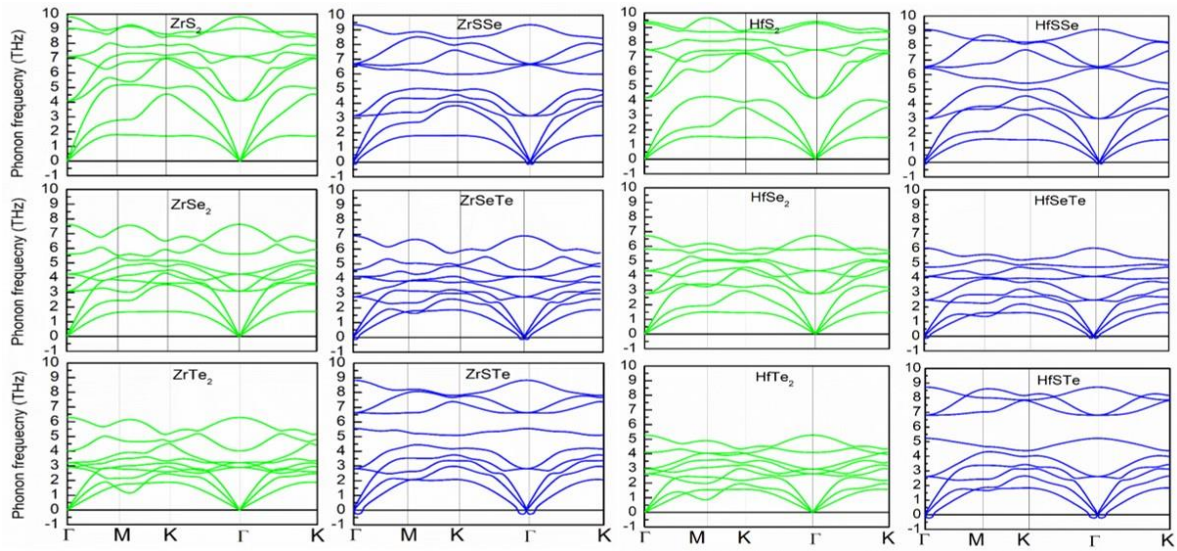

Figure 3. 2 Phonon energy dispersion spectrum of 1T-MX_2 and MXY Janus monolayers.

3.3.3 Electronic structure

The electronic band structure of the pristine and Janus structures in the 1T phase in Group IVB-VIA monolayers is presented in Figure 3.3. Monolayers of ZrS_2, $ZrSe_2$, HfS_2 and $HfSe_2$ are semiconductors with indirect bandgap. DFT at GGA-PBE level is well known to underestimate the band gap. Therefore, more accurate calculations with HSE06 functional have been performed to compute the band gap in all the monolayers. Telluride-based MX_2 monolayers are found to be semi-metallic in nature. Janus structures of Zr and Hf based dichalcogenides are found to be semiconductors with an indirect band gap ranging from 0.15-2.03 eV. The conduction band minimum (CBM) lies at the M-point while valence band maximum (VBM) is located at the Γ point of the Brillouin zone (BZ), which agrees well with the experimental and theoretical findings [139]. A closer inception shows that the incorporation of sulphur imparts to the Janus monolayer a larger band gap relative to $ZrSe_2$ and $HfSe_2$ monolayers. For a deeper understanding, we have probed into the origin of VBM

and CBM. For these monolayers occurring in trigonal structures, the valence bands primarily show p-orbital character arising from the chalcogen atoms, while the conduction bands consist mainly of d-orbitals contributed by the transition metal atoms, as shown in Figure 3.4 (a) and (b). In1H-MX_2 (M=Mo, W; X = S, Se, Te) monolayers, the VBM and

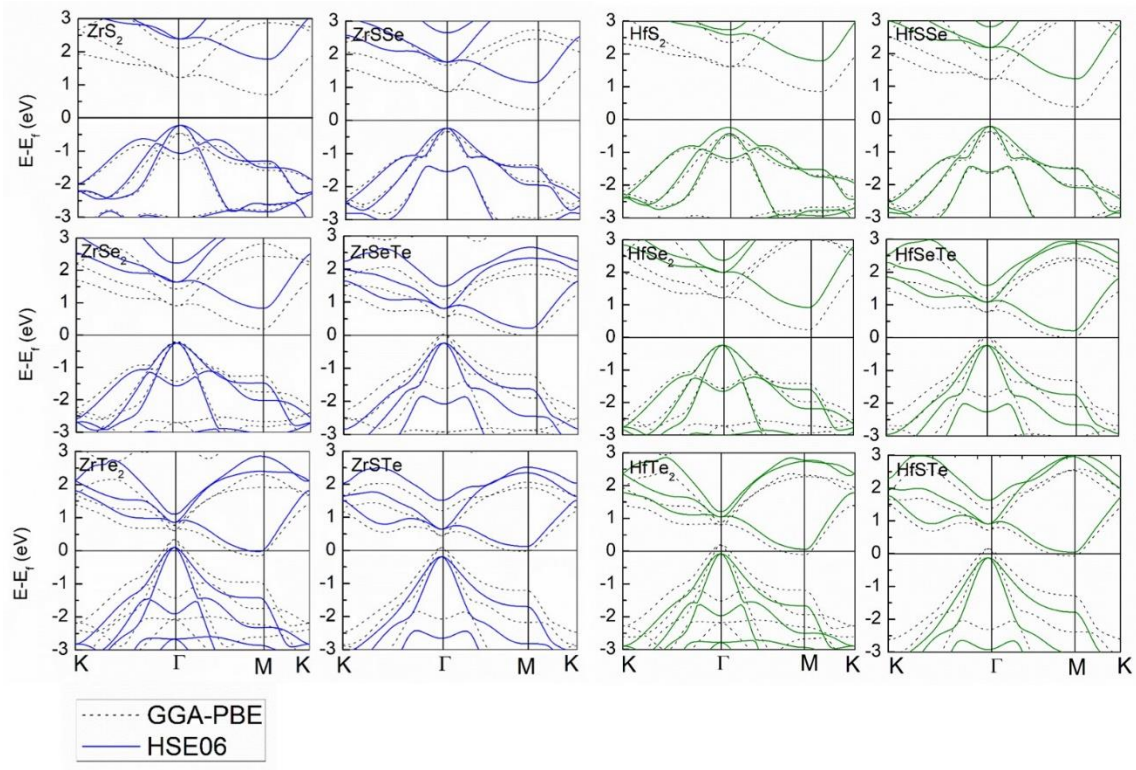

Figure 3. 3 Electronic band dispersion of 1T-MX2 and their corresponding Janus MXY monolayers determined via GGA-PBE (dotted curves) and HSE06 calculations (solid curves). M= Zr, Hf and X=S/Se/Te.

Table 3. 3 Electronic band gap of monolayer MX_2 (M = Zr, Hf; X= S, Se, Te) using GGA-PBE and HSE06 functional.

	ZrS_2	$ZrSe_2$	$ZrTe_2$	ZrSSe	ZrSeTe	ZrSTe
GGA-PBE	1.16	0.38	Metallic	0.66	Metallic	Metallic
HSE06	1.99	1.07	Metallic	1.37	0.43	0.30

	HfS_2	$HfSe_2$	$HfTe_2$	HfSSe	HfSeTe	HfSTe
GGA-PBE	1.33	0.48	Metallic	0.74	Metallic	Metallic
HSE06	2.03	1.16	0.13	1.45	0.44	0.15

CBM are bonding and antibonding states arising from the hybridization of the metal-d and chalcogen-p states. Consequently, the VBM and CBM in 1H-MX_2 (M=Mo, W; X = S, Se, Te) monolayers and their Janus structures are coupled, while these band edges in 1T-MX_2 (M=Zr,

Hf; X=S, Se, Te) monolayers and their Janus structures are decoupled. The coupled (decoupled) band edges cause direct (indirect) band gaps in the former and latter respectively. The orbital projected electronic band structure of monolayer structures of 1T-ZrS_2 and Janus ZrSSe is shown in Fig. 3.4. The projections on the S-p orbitals and Zr-d orbitals reveal that the valence band comprises mainly of p-orbitals of chalcogen atoms, whereas the composition of the conduction band is dominated by the d orbitals of transition metal atoms. Furthermore, for the ZrSSe monolayer, the p-orbital contribution to VBM is mainly made by the Se atom, instead of the S atom. Similar results are obtainable for the other Janus monolayers. Figure 3.5 shows that the detailed band decomposed charge density of the VBM and CBM at the Γ and M point in the BZ for ZrS_2 and ZrSSe monolayers with the contribution of different orbitals in varying percentages agrees with the earlier findings[159].

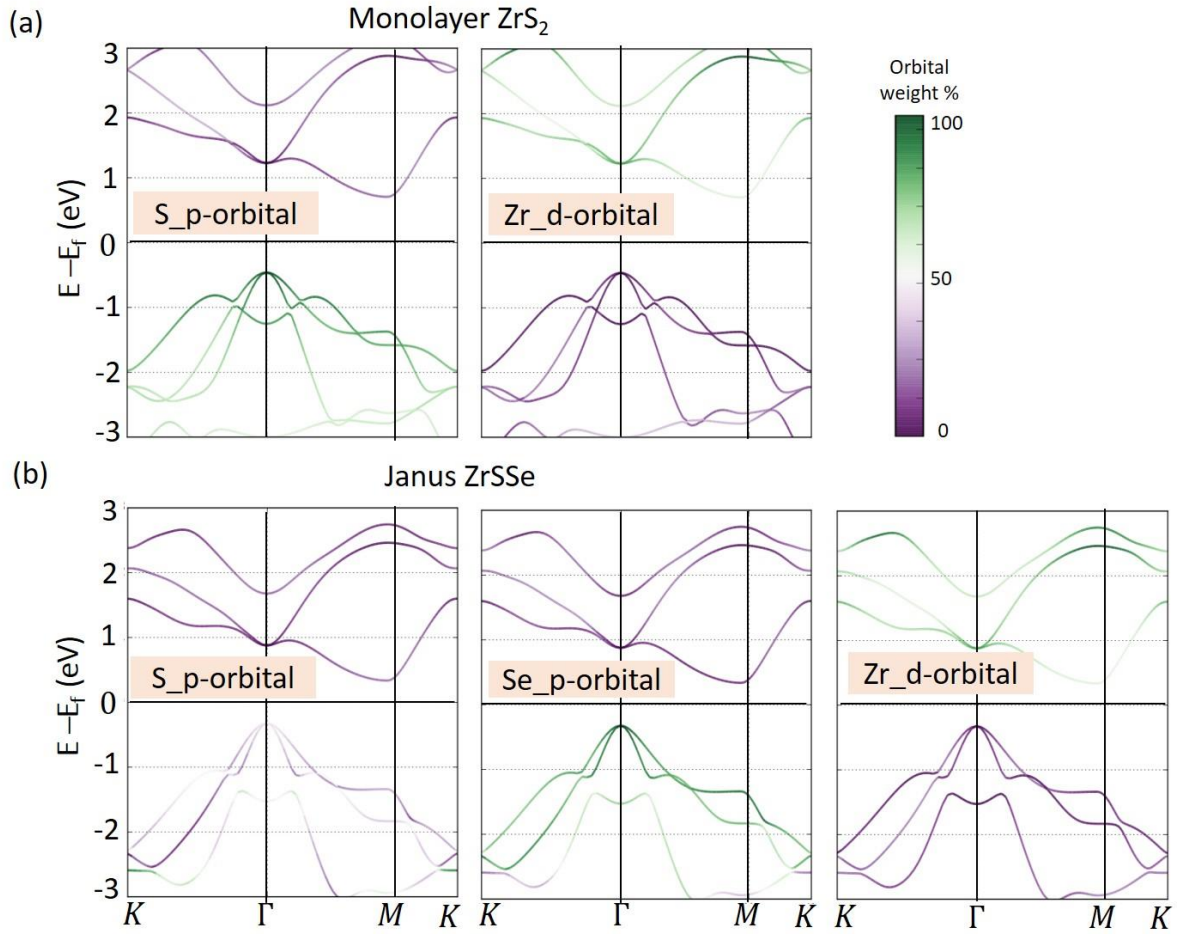

Figure 3. 4 Electronic band structure of monolayers of (a) 1T-ZrS_2 and (b) Janus ZrSSe projected on the p-orbitals of S-atom and d-orbitals of Zr-atom. The valence band shows a predominance of the p-orbital character of chalcogen atoms whereas conduction band shows that of the d-orbital of the transition metal atom. The scale indicates the magnitude of the orbital projection.

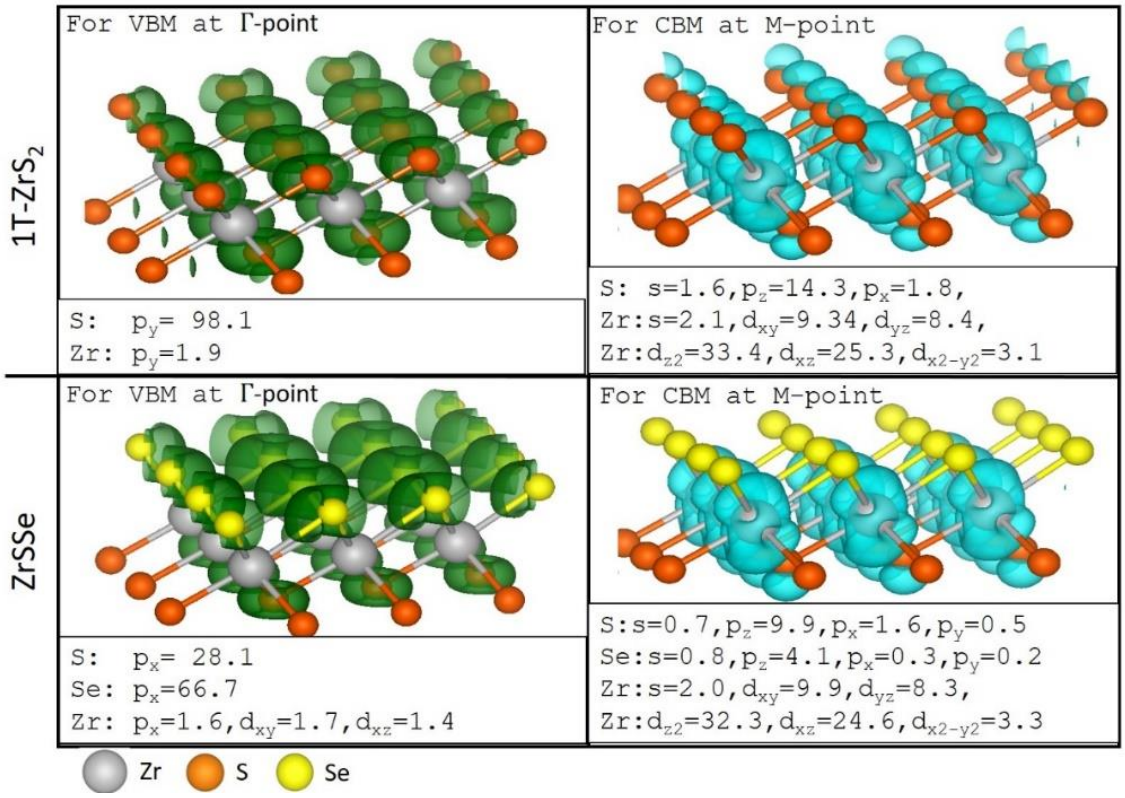

Figure 3. 5 Band decomposed charge density at the VBM (G point) and CBM (M point) in the BZ for ZrS_2 and ZrSSe monolayers.

3.3.4 Elastic properties

A stiffer material will have a lower elongation per unit length for the same magnitude of applied force or strain. Therefore, the stiffer the material, the larger will be its Young's modulus. In such cases, a large force must be applied to bring about a considerable deformation and generate electricity in the piezoelectric material. Therefore, a small Young's modulus is preferable to induce piezoelectric voltages with relative ease. Moreover, in the expressions for piezoelectric strain coefficients, the elastic tensor components occur in the denominator. Therefore, a smaller elastic constant will induce a higher piezoelectric response under the application of uniaxial strain. According to the definition, the total elastic stiffness coefficients, which is the sum of ionic and electronic contributions, can be evaluated as $C_{ijkl} = d\sigma_{ij}/d\varepsilon_{kl} = C_{ijkl}^{ion} + C_{ijkl}^{el}$; where σ_{ij} and ε_{kl} depict the stress tensor and strain tensor respectively. In the Voigt notation, the subscripts i and j for the components of σ_{ij} and ε_{ij} can be indicated as $1 = xx$, $2 = yy$, $3 = zz$, $4 = yz$, $5 = zx$, $6 = xy$. Symmetry analysis based on point group reduces the number of independent components of the elastic tensors. As 1T-MX_2 and Janus MXY monolayers belong to the trigonal $3m$ and $\bar{3}m$ point group, the elastic tensors reduce to

$$C_{kl} = \begin{pmatrix} C_{11} & C_{12} & C_{13} & C_{14} & . & . \\ C_{12} & C_{11} & C_{13} & -C_{14} & . & . \\ C_{13} & C_{13} & C_{33} & . & . & . \\ C_{14} & -C_{14} & . & C_{44} & . & . \\ . & . & . & . & C_{44} & C_{14} \\ . & . & . & . & C_{14} & \frac{C_{11}-C_{12}}{2} \end{pmatrix} \quad (3.1)$$

It is noticed in Table 3.3 and Figure 3.6 that the calculated elastic constants are positive (with exception of $ZrTe_2$) and satisfies the Born-Huang stability criteria for crystals having trigonal symmetry for which the following conditions must be met for mechanically stable trigonal crystals: $C_{11} > 0$ and $C_{11} - C_{12} > 0$.

The 2D Young's modulus of elasticity can be determined using the following relation [160]:

$$Y_{2D} = \frac{C_{11}^2 - C_{12}^2}{C_{11}}$$

The corresponding Poisson's ratio can be obtained as

$$\nu_{2D} = \frac{C_{12}}{C_{11}}$$

Table 3. 4 Electronic and ionic contribution to in-plane elastic stiffness constants, C_{11} (Nm^{-1}), C_{12} (Nm^{-1}), Young's modulus, Y_{2D} (Nm^{-1}), and Poisson's ratio, ν_{2D} of 1T-MX_2 and Janus MXY monolayers in 1T-phase

2D-NS	$C_{11}^{elec.}$	$C_{12}^{elec.}$	C_{11}^{ionic}	C_{12}^{ionic}	C_{11}^{total}	C_{12}^{total}	Y_{2D}	ν_{2D}
ZrS_2	99.65	31.83	-24.08	-16.74	75.57	15.09	72.55	0.19
$ZrSe_2$	92.67	28.77	-23.80	-14.32	68.86	14.45	65.83	0.20
$ZrTe_2$	63.40	24.07	-43.99	8.36	19.40	32.44	-34.89	1.67
ZrSSe	96.17	30.87	-25.84	-15.38	70.32	15.49	66.91	0.22
ZrSTe	79.91	28.61	-40.33	-0.83	39.57	27.78	20.07	0.70
ZrSeTe	72.72	23.74	-24.94	-11.10	47.77	12.64	44.43	0.26
HfS_2	106.66	32.82	-25.89	-17.83	80.77	14.98	77.99	0.18
$HfSe_2$	97.72	29.30	-22.64	-13.75	75.07	15.55	71.85	0.21
$HfTe_2$	66.77	22.60	-32.30	-1.33	34.47	21.27	21.34	0.61
HfSSe	102.34	31.31	-24.45	-15.41	77.88	15.90	74.63	0.20
HfSTe	87.29	31.78	-35.77	-10.52	51.51	21.25	42.74	0.41
HfSeTe	79.69	24.97	-24.92	-11.54	54.76	13.42	51.47	0.24
1H-MoS_2	167.91	52.71	-25.52	-17.36	142.38	35.35	133.60	0.24

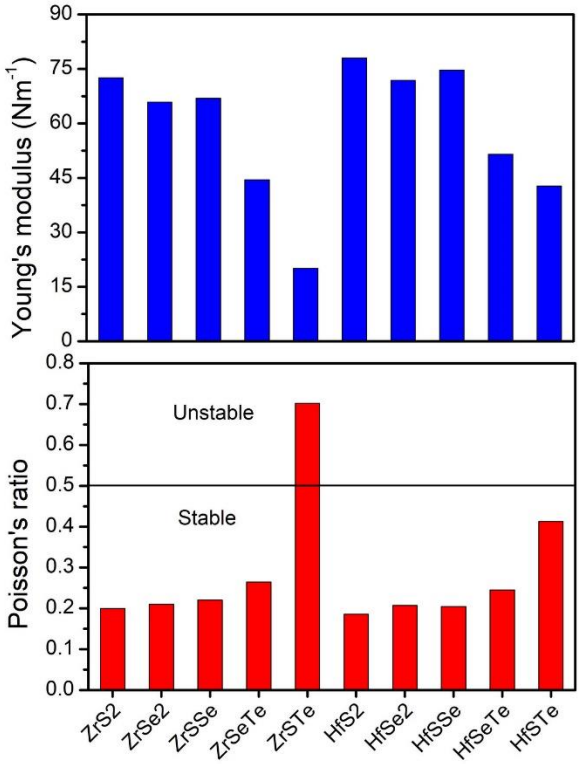

Figure 3. 6 Young's modulus and Poisson's ratio in pristine 1T-MX_2 and its Janus structures, MXY

The calculated elastic stiffness constants and elastic moduli (Y_{2D} and ν_{2D}) agree well with previous reports[161],[162]. The total in-plane elastic stiffness constants (C_{11}, C_{12}) have been split into electronic and ionic components, as shown in Table 3.3. It is observed that the ionic contribution to the elastic constant of Group IVB monolayers such as ZrS_2 and HfS_2 is comparable to the Group-VI monolayers such as 1H-MoS_2. For a systematic comparison, the ionic and electronic contribution to the in-plane elastic stiffness constants in 1H-MoS_2 calculated in the present study agrees with the earlier reports [29,163,164]; however, there is a diminution in the contribution of the electronic component which results in a low elastic stiffness in Group IVB monolayers. From Table 3.3, it is evident that all the materials considered in this study are found to be less stiff than other 2D materials such as graphene [165] (Y=341 N/m), single layer h-BN[166] (Y=275.9 N/m), and most of the TMDCs [162]. The Poisson ratio, ν_{2D} of the Janus structures are slightly larger than that of Group VI TMDCs. Similar to MoS_2 and MoSSe monolayers, the related elastic constants of the ZrSSe monolayer are smaller than those of the ZrS_2 monolayer. Compared to MoSSe, the in-plane strain engineering of a larger magnitude can be easily achieved in ZrSSe monolayer due to its smaller Young's modulus. According to Table 3.3, the elastic stiffness constant and Young's modulus for Janus MXY monolayers are slightly smaller than 1T-MX_2 monolayers. This indicates that MXY monolayers are more flexible than MX_2 monolayers due to smaller Young's modulus. The smaller Young's modulus is due to the weaker M-X/Y bond strength. This opens the scope

for in-plane strain engineering, of a large magnitude, in these monolayers, which is very important in tuning physical properties, such as, bandgap engineering and piezoelectricity.

3.3.5 Piezoelectric properties

Piezoelectricity occurs only in certain non-centrosymmetric materials where an electric dipole moment is generated upon the application of stress or strain. This is often referred to as the direct piezoelectric effect. Conversely, the indirect piezoelectric effect refers to the case when strain or stress is generated in a material upon the application of an applied electric field. The piezoelectric response of a material is ascertained *via* different piezoelectric constants, which are the various Maxwell derivatives of thermodynamic functions such as $e_{ijk} = e_{ijk}^{ion} + e_{ijk}^{el} = \left(\partial P_i/\partial \varepsilon_{jk}\right)_{E,T}$ for the direct piezoelectric effect and $e_{ijk} = e_{ijk}^{ion} + e_{ijk}^{el} = -\left(\partial \sigma_{jk}/\partial E_i\right)_{\varepsilon,T}$ for the converse piezoelectric effect. e_{ijk} is a third-rank piezoelectric stress tensor, P_i is the electric polarisation vector, ε_{jk} is the strain tensor, σ_{jk} is the stress tensor, E_i is the macroscopic electric field, and T is the temperature; $i, j, k \in \{1,2,3\}$ and 1,2,3 corresponds to the spatial x, y and z directions respectively. Besides, the mechano-electrical transduction efficiency is expressed *via* the piezoelectric strain coefficient, d_{ijk}. In two-dimensional materials, in the Voigt notation, the third rank tensors, e_{ijk} and d_{ijk} reduce to second rank tensors, e_{il} and d_{il}, where $l \in \{1,2,\ldots,6\}$. The total number of independent components is reduced due to symmetry constraints, as given in eqn. (3.1)-(3.3). Pristine 1T-MX_2 monolayer possesses centrosymmetric $\bar{3}m$ point group symmetry and therefore, all its piezoelectric coefficients are zero, while symmetry in their Janus MXY monolayers changes to non-centrosymmetric $3m$ point group giving non-zero piezoelectric stress tensors, e_{il} as

$$e_{il} = \begin{pmatrix} . & . & . & . & e_{15} & -e_{22} \\ -e_{22} & e_{22} & . & e_{15} & . & . \\ e_{31} & e_{31} & e_{33} & . & . & . \end{pmatrix} \tag{3.2}$$

and non-zero piezoelectric strain tensor, d_{il} as

$$d_{il} = \begin{pmatrix} . & . & . & . & d_{15} & -2d_{22} \\ -d_{22} & d_{22} & . & d_{15} & . & . \\ d_{31} & d_{31} & d_{33} & . & . & . \end{pmatrix} \tag{3.3}$$

where the dot denotes 0 value.

In Voigt notation, in two-dimensional systems, the non-vanishing components become as follows

$$e_{222} = -e_{211} = -e_{112} = e_{22} = -e_{21} = -e_{16}$$

$$e_{311} = e_{322} = e_{31} = e_{32}$$

$$e_{333} = e_{33}$$

$$e_{113} = e_{212} = e_{15} = e_{24}$$

Based on symmetry analysis, 1T-MXY (M= Zr and Hf; X, Y = S, Se, and Te) Janus monolayers will have four independent piezoelectric tensor components or coefficients, namely, e_{22}, e_{31}, e_{33} and e_{15}.

e_{22} corresponds to the in-plane polarisation inducible by uniaxial in-plane uniaxial strain, while e_{31} and e_{33} represent the out-of-plane polarisation inducible by uniaxial strain along a-axis and c-axis, respectively. e_{15} describes the polarisation inducible by shear strain. Density functional perturbation theory has been used to calculate e_{il}, while d_{il} has been derived using the relation

$$e_{il} = d_{ik} C_{kl} \tag{3.4}$$

where C_{kl} is elastic stiffness tensor. The non-zero components in d_{il} can be derived from the following relationships:

$$d_{22} = \frac{e_{22}}{C_{11} - C_{12}} \tag{3.5}$$

$$d_{31} = \frac{e_{31}}{C_{11} + C_{12}} \tag{3.6}$$

For a systematic and a direct comparison with the experimental piezoelectric response, the calculated piezoelectric stress tensor needs to be converted into piezoelectric strain tensor. Only in-plane piezoelectric coefficients, or d_{22} in MXY (M=Zr and Hf; X=S, Se, and Te) monolayers have a significantly high value, which is comparable to the known bulk piezoelectric materials and 1H-MX_2 monolayers. The piezoelectric strain coefficient, d_{22} values are even much higher than commonly used 3D piezoelectric materials such as α-quartz [167] (d_{11} *= 2.3 pm/V*) and AlN [167] (d_{33}*= 5.6 pm/V*), wurtzite-GaN [167] (d_{33} *= 3.1 pm/V*) implying the importance of the in-plane piezoelectric effects in these monolayer materials. The values shown in Table 3.4 clearly show remarkably high piezoelectric constants of the Janus monolayer and their great potential for application in nanoscale technologies.

Table 3. 5 Piezoelectric stress/strain coefficients or tensor components: e_{22}/d_{22} (in-plane) and e_{31}/d_{31} (out-of-plane) in Janus MXY monolayers in 1T-phase[a].

2D-NS MXY	Ionic contribution				Electronic contribution				Net contribution			
	e_{22}	e_{31}	d_{22}	d_{31}	e_{22}	e_{31}	d_{22}	d_{31}	e_{22}	e_{31}	d_{22}	d_{31}
ZrSSe	2.98	-0.16	5.43	-0.186	0.15	0.165	0.27	0.192	3.13	0.005	5.58	0.006
ZrSeTe	2.78	-0.266	7.91	-0.440	0.76	0.151	2.16	0.250	3.54	-0.115	8.67	-0.190
ZrSTe	2.15	-0.305	18.23	-0.453	-0.43	0.308	-3.65	0.457	1.72	0.003	14.58	0.004
HfSSe	2.68	-0.166	4.32	-0.177	0.22	0.214	0.36	0.228	2.90	0.048	4.68	0.051
HfSeTe	4.81	0.030	11.64	0.044	0.11	0.252	0.00	0.370	4.92	0.282	11.64	0.414
HfSTe	3.37	-0.294	11.14	-0.404	0.52	0.423	1.72	0.581	3.89	0.129	12.86	0.177

[a] The units e_{il} and d_{il} are 10^{-10} C/m and pm/V respectively.

For 1T Janus TMDCs, we need to calculate the in-plane e_{22} component and out-of-plane e_{31} and e_{33} components. The piezoelectric coefficient e_{31} is non-zero here due to the absence of an inversion centre between the two layers of chalcogenides. The corresponding piezoelectric strain tensor, d_{ijk} of each material has been calculated from the relationship, (3.5) and (3.6). For 1T-MX_2 monolayer, a zero piezoelectric coefficient is obtained owing to its centrosymmetric structure. The calculated piezoelectric stress tensor for 1T MX_2 monolayers are all zero as expected from the symmetry of these materials. Table 3.4 shows the results for piezoelectric stress coefficient (e_{ijk}) and piezoelectric strain (d_{ijk}) coefficient of Janus monolayer MXY structures with M=Zr and Hf and X=S, Se, and Te. The calculated values show that the magnitude of the ionic contribution is larger than the electronic contribution for all the considered materials.

Furthermore, to explore the maximum possible enhancement in the piezoelectric coefficients in these Janus monolayers under the application of strain, the HfSSe monolayer has been subjected to both uniaxial and biaxial strain. The Janus HfSSe monolayer has been judiciously chosen here, as it shows the lowest e_{22} and d_{22} values among the six Janus monolayers studied in this work. Yet, a colossal enhancement in its piezoelectric coefficients is observed at 9% of uniaxial tensile strain (e_{22}=78.49 × 10^{-10} C/m; d_{22}=123.04 pm/V) applied along the arm-chair direction, as shown in Figure 3.7 (a), while e_{22} =16.74 ×10^{-10} C/m; d_{22}=37.67 pm/V is reached at 7% of biaxial tensile strain, as shown in Figure 3.7 (b). Out of all the strain types investigated, the application of uniaxial strain along the arm-chair direction has been found to cause the largest enhancement in e_{22} and d_{22}, which reach as high as the ones in the state-of-the-art perovskites. Uniaxial strain applied along the zig-zag direction is not found to cause any noticeable change in e_{22} or d_{22}, as shown in Figure 3.8.

A smooth rise (drop) in d_{33} (d_{31}) in the state-of-the-art perovskites bulk $BaTiO_3$

($PbTiO_3$) with the application of hydrostatic-pressure was reported [168]; however, the peak in d_{33} (d_{31}) was not reached, as the application of pressure was limited to 4 GPa in that study. Nonetheless, the peak in d_{31} (d_{33}) in $PbTiO_3$ was reported to reach around 8 GPa and 13 GPa respectively in a later work by Wu and Cohen [169], based on local density approximation (LDA). Subsequently, Kvasov et al.[170] verified experimentally the enhancement in piezoelectric coefficient under negative pressure, which was predicted by first principles calculations. In that work, the maximum enhancement in longitudinal piezoelectric coefficient (d_{33}) and hydrostatic piezoelectric coefficient (d_H) was simultaneously found to occur at -1 GPa, -2 GPa and -7 GPa in bulk $PbTiO_3$, $Pb(Zr,Ti)O_3$ and $BaTiO_3$ respectively.

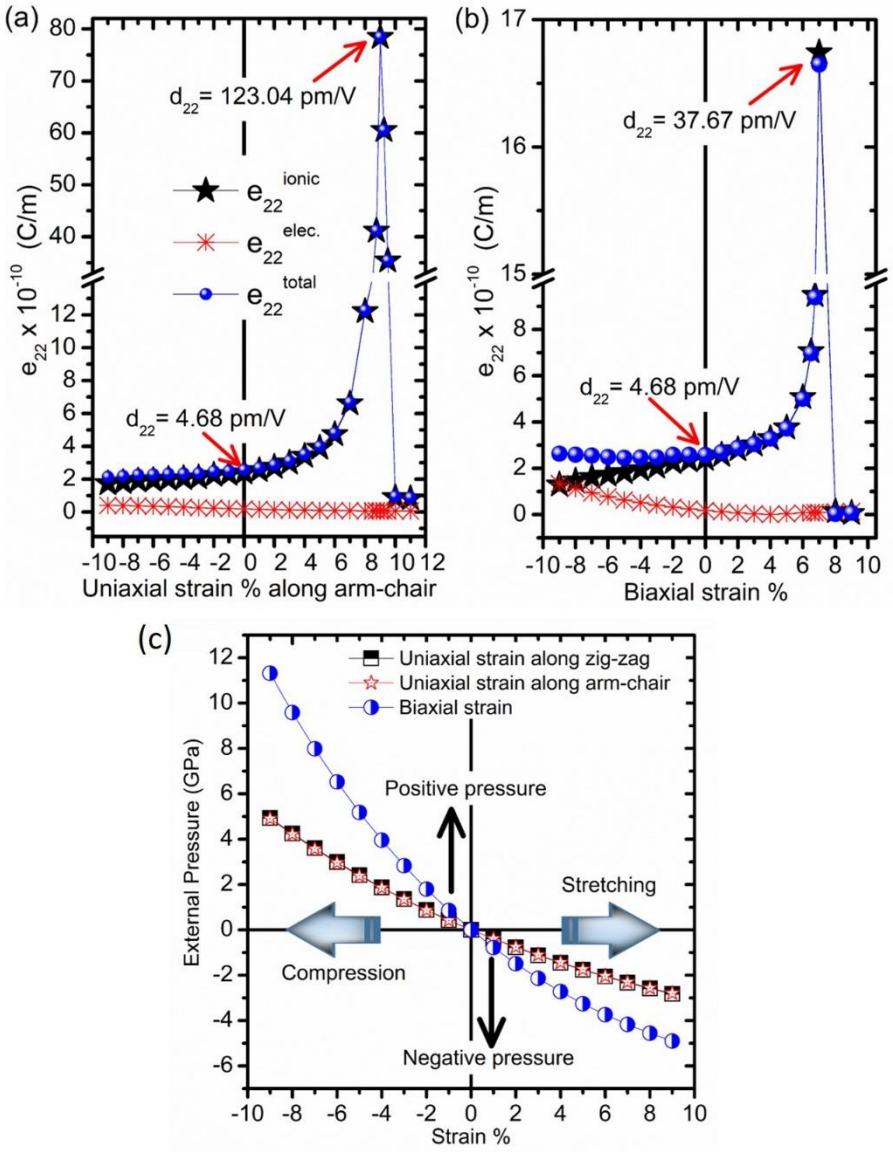

Figure 3. 7 Variation in the piezoelectric stress coefficient, e_{22} in Janus HfSSe monolayer with the application of (a) uniaxial strain along the arm-chair direction and (b) biaxial strain. [The peaks are found to occur at 9% uniaxial tensile strain applied along arm-chair direction and at 7% biaxial tensile strain.] (c) Strain induced pressure on the basal plane in Janus HfSSe monolayers.

The pressure induced on the basal plane of HfSSe monolayer by the application of mechanical strain, as computed in this work, has been provided in Figure 3.7 (c). Tensile (compressive) strain is found to bring about negative (positive) pressure on the basal plane.

-2.8 GPa and -4.2 GPa correspond to the pressure induced on the basal plane in HfSSe monolayer by the application of 9% uniaxial tensile strain applied along the arm-chair direction and 7% biaxial strain respectively, where the piezoelectric coefficients reach their peak values.

Janus HfSSe monolayers are found to remain mechanically stable under these types and magnitude of strain, as confirmed by the satisfaction of Born-Huang stability criteria. Moreover, Young's modulus and Poisson's ratio tabulated in Table 3.6. Interestingly, band gap changes from indirect to direct at these type and magnitude of strain, as tabulated in Table 3.6.

Table 3. 6 Elastic stiffness constants, C_{11} (N/m), C_{22} (N/m), C_{12}(N/m), Young's modulus, Y_{2D} (N/m) & Poisson ratio, ν_{2D} along zig-zag (zz) and arm-chair (ac) directions, piezoelectric stress coefficients, e_{22} & e_{31} (10^{-10} C/m), piezoelectric strain coefficients, d_{22} & d_{31} (pm/V), external pressure, $P_{ext.}$ (GPa) and HSE06 Bandgap, E_g in unstrained and strained HfSSe monolayer

HfSSe	C_{11}^{total}	C_{22}^{total}	C_{12}^{total}	Y_{zz}	Y_{ac}	ν_{zz}	ν_{ac}	e_{22}	e_{31}	d_{22}	d_{31}	$P_{ext.}$	$E_{g,HSE06}$
Unstrained	77.88	77.88	15.90	74.63	74.63	0.20	0.20	2.90	0.005	4.68	0.051	0	1.45 (I)
Uniaxial tensile along arm-chair at 9% strain	73.48	53.77	9.69	72.20	52.03	0.13	0.18	78.49	0.69	123.04	0.83	-2.8	1.61 (D)
Biaxial strain at 7% strain	55.22	54.15	10.79	53.11	51.99	0.19	0.20	16.74	0.14	37.67	0.21	-4.2	1.99 (D)

The state-of-the-art perovskites show a major anisotropy in piezoelectricity between its crystal orientations, e.g, between the [001] and [111] directions in $BaTiO_3$ [171]. However, in this work on Janus monolayers, Table 3.4 shows e_{31} and d_{31} to be so small as to be ignorable. As d_{22} is considerable and d_{31} is ignorable, piezoelectricity in the pristine, unstrained Janus monolayers may essentially be regarded as in-plane. Nevertheless, d_{31} is found to reach its maximum value of 0.83 pm/V at 9% uniaxial tensile strain applied along the arm-chair direction, as shown in Figure 3.8. Therefore, under this type and magnitude of strain, a mild anisotropy in piezoelectricity is found to arise between the in-plane arm-chair direction and the out-of-plane z direction. In nanopiezotronic FET devices, the Janus monolayers need to interface the source and the drain along its arm-chair direction. d_{22} will then be able to facilitate and control the flow of carriers considerably along the arm-chair direction in response to uniaxial tensile strain applied along the same direction, while d_{31} can bring about top gating effects *via* the build-up of piezopotential along the z direction in response to uniaxial mechanical strain applied along the zig-zag direction. d_{31} will also ease the separation of electron and holes along the z direction. Mild polarization along the z direction may also help

to attract and adsorb polar molecules both on the top and bottom side of the Janus monolayers, thereby enabling its sensing applications as well.

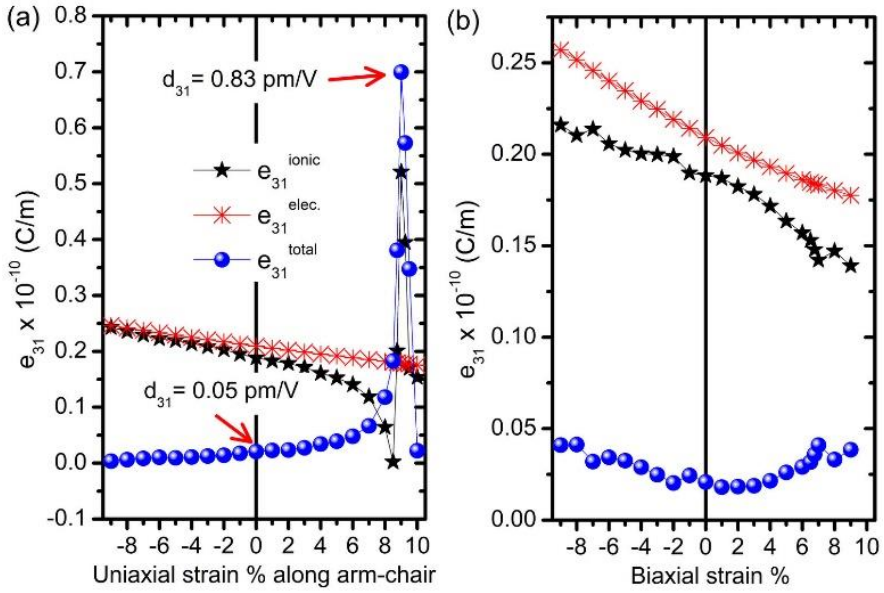

Figure 3. 8 Variation in the out-of-plane e_{31} piezoelectric coefficients with the application of (a) uniaxial strain along the armchair direction and (b) biaxial strain.

3.3.6 Born effective charges

Born effective charges (BEC), Z_{ij}^{*} are derivatives of the intrinsic polarisation vector (P_i) with respect to the strain or the derivatives of the atomic forces with respect to the applied electric field, as given below.

$$Z_{ij}^{*} = \Omega/e\left(\partial P_i/\partial u_j\right) = 1/e\left(\partial F_i/\partial E_j\right),$$

where $i, j = x, y, and\ z$, Ω is the unit cell volume, u is the strain, E is electric field and F is the Hellmann-Feynman forces.

Therefore, BEC elucidates the physical picture or the mechanism underlying the piezoelectric properties. The macroscopic current and electronic polarisation change due to displacement of ions can be quantified through Z_{ij}^{*}. For all studied monolayers, off diagonal elements of Z_{ij}^{*} are zero and the values obey the acoustic sum rule with negligible error. The 1T-MX_2 (M=Zr and Hf; X=S, Se, and Te) monolayers are in stark contrast to 1H-MX_2 (M=Mo and W; X = S, Se, and Te) monolayers, as the sign of the static charge and the BEC are counterintuitive [172]. However, like perovskite materials [173,174], the BEC charges in 1T-MX_2 and their Janus monolayers are found to be enormously large with respect to their static nominal charges as shown in Figure 3.9. The high Z_{ij}^{*} magnitude is consistent with previous findings [175] and confirms the high piezoelectric coefficients.

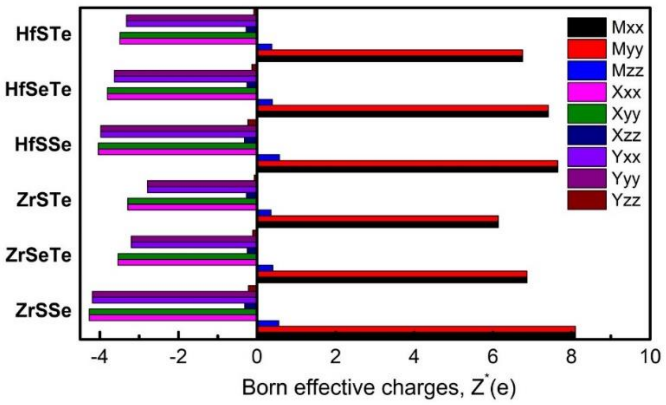

Figure 3. 9 Born effective (or dynamical) charge tensors on each ionic species in Janus structures in Group IVB transition metal dichalcogenide monolayers or MXY

3.3.7 Robust charge carrier mobility for piezotronics

The possibilities for a seamless and an adaptive merging of piezoelectric properties with the semiconducting properties and high charge carrier mobility make 2D 1T-MX_2 monolayers suitable for piezotronic applications[59],[123]. Furthermore, high carrier mobility in the semiconducting materials is necessary to guarantee a low power dissipation and a high switching rate in the electronic device [143]. The room temperature carrier mobility has been calculated in this work by using longitudinal acoustic phonon-limited carrier scattering model within the framework of effective mass and deformation potential approximation originally formulated by Bardeen and Shockley [176] (eqn. (3.7)) and recently modified by *Lang et al* [177] (eqn. (3.8)). The latter is a quantum leap beyond the former as it incorporates the anisotropy in the elastic stiffness constants, deformation potential and effective mass along both the longitudinal charge transport direction and the in-plane transverse direction. In inorganic semiconductors, the coherent wavelength of thermally agitated carriers at room temperature is much larger than their lattice constants and is close to acoustic phonon modes at the zone center of the BZ. Therefore, the coupling between electron and acoustic phonons dominates the carrier scattering in the low energy regime. Therefore, in this limit, carrier mobility can be effectively derived from the effective mass and deformation potential approximation. Both the formulations have been used in the present work in the calculation of longitudinal acoustic phonon limited charge carrier mobility.

$$\mu_{\alpha x}^{(1)} \approx \frac{2e\hbar^3 C_{x_{2D}}}{3k_B T m_{\alpha x}^{*2} E_{\alpha x}^2} x10^4 \; cm^2 V^{-1} s^{-1} \qquad (3.7)$$

$$\mu_{\alpha x}^{(2)} \approx \frac{e\hbar^3\left(\frac{5C_{x_{2D}}+3C_{y_{2D}}}{8}\right)}{k_B T(m_{\alpha x})^{\frac{3}{2}}(m_{\alpha y})^{\frac{1}{2}}\left(\frac{9E_{\alpha x}^2+7E_{\alpha x}E_{\alpha y}+4E_{\alpha y}^2}{20}\right)} x10^4\ cm^2V^{-1}s^{-1} \quad (3.8)$$

where $\alpha = e, h$ denotes the type of carriers (electrons or holes), effective mass of carriers in the units of rest mass of electron m_0 along the x and y directions are designated by $m_{\alpha x}$ and $m_{\alpha y}$ respectively and calculated by using the relation: $m_\alpha = \hbar^2[\partial^2 E(k)/\partial k^2]^{-1}$, deformation potential of the carriers along the x and y directions are denoted by $E_{\alpha x}$ and $E_{\alpha y}$ respectively and 2D elastic stiffness coefficients along the x and y directions are designated by $C_{x_{2D}}$ and $C_{y_{2D}}$ respectively. All the mobility calculations have been carried out at 300 K. The other component $\mu_{\alpha y}$ of mobility can be easily calculated by simply interchanging x and y in eqn (3.8).

The results on carrier mobility are summarized in Table 3.6. The carrier mobility is highly sensitive to the deformation potential, as the former is inversely proportional to the square of the latter. The deformation potential of electrons (holes) is given by the slope of the CBM (VBM) energies with the application of infinitesimal magnitude of strain about the equilibrium lattice constant [178–180]. Therefore, the physical origin of the differences in deformation potential between holes and electrons can be clearly understood from the nature and composition of the band edges, i.e., the CBM and VBM.

Table 3. 7 Parameters along the zigzag (x) and armchair (y) directions used in the carrier mobility calculations on different 2D monolayer nanosheets (2D-NS).

2D-NS	$m_e^*(x)$	$m_e^*(y)$	$C_{11}(x)$	$C_{11}(y)$	$E_e(x)$	$E_e(y)$	$\mu_e^{(2)}$(x)	$\mu_e^{(2)}$(y)	$\tau_e(x)$	$\tau_e(y)$	$\mu_e^{(1)}$(x)	$\mu_e^{(1)}$(y)
ZrS2	0.283	1.998	75.57	75.57	-3.71	-3.65	120.11	2.42	19.32	2.75	973.37	20.17
ZrSe2	0.187	1.813	68.86	68.86	-2.67	-3.66	597.66	5.64	63.54	5.82	3921.98	22.2
ZrSSe	0.24	2.21	70.32	70.32	3.57	3.33	186.53	2.25	25.45	2.83	1360.07	18.43
ZrSeTe	0.138	2.122	47.77	47.77	-5.56	-5.36	278.96	1.19	21.88	1.44	1152.1	5.24
ZrSTe	0.194	4.101	39.57	39.57	-4.05	-5.79	56.60	0.11	6.243	0.25	910.11	0.99
HfS2	0.238	2.382	80.77	80.77	2.82	2.83	308.36	3.07	41.72	4.16	2545.9	25.23
HfSe2	0.164	2.11	75.07	75.07	2.56	2.58	1195.79	7.20	111.50	8.64	6047.04	35.96
HfSSe	0.197	2.407	77.88	77.88	2.73	2.72	556.85	3.73	62.37	5.11	3823.07	25.79
HfSeTe	0.145	3.039	54.76	54.76	3.34	3.32	520.56	1.18	42.91	2.05	3314.96	7.63
HfSTe	0.151	4.085	51.51	51.51	4.15	4.22	205.10	0.27	17.60	0.64	1862.45	2.46
2D-NS	$m_h^*(x)$	$m_h^*(y)$	$C_{11}(x)$	$C_{11}(y)$	$E_h(x)$	$E_h(y)$	$\mu_h^{(2)}$(x)	$\mu_h^{(2)}$(y)	$\tau_h(x)$	$\tau_h(y)$	$\mu_h^{(1)}$(x)	$\mu_h^{(1)}$(y)
ZrS2	0.443	0.445	75.57	75.57	-8.69	-4.54	37.87	47.36	9.54	11.98	72.4	262.88
ZrSe2	0.28	0.28	68.86	68.86	-10.25	-4.56	167.08	221.25	26.59	35.22	118.69	599.74
ZrSSe	0.33	0.332	70.32	70.32	-9.52	-4.46	195.84	356.94	36.74	67.37	101.16	455.38
ZrSeTe	0.124	0.124	47.77	47.77	-6.04	-4.45	6740.51	7559.98	475.21	532.99	1209.15	2227.59
ZrSTe	0.111	0.111	39.57	39.57	-4.04	-5.59	11604.15	10274.14	732.34	648.40	2793.84	1459.28
HfS2	0.469	0.47	80.77	80.77	-8.81	-3.62	34.64	46.70	9.238	12.48	67.17	396.17
HfSe2	0.321	0.321	75.07	75.07	-6.6	-5.59	179.99	191.70	32.85	34.98	237.47	331.03
HfSSe	0.375	0.376	77.88	77.88	-6.74	-7.15	80.50	78.29	17.16	16.73	173.09	152.99
HfSeTe	0.191	0.192	54.76	54.76	-6.18	-8.96	741.95	639.23	80.57	69.78	558.03	262.71
HfSTe	0.147	0.148	51.51	51.51	-7.37	-7.68	1906.56	1851.60	159.34	155.80	623.11	566.09

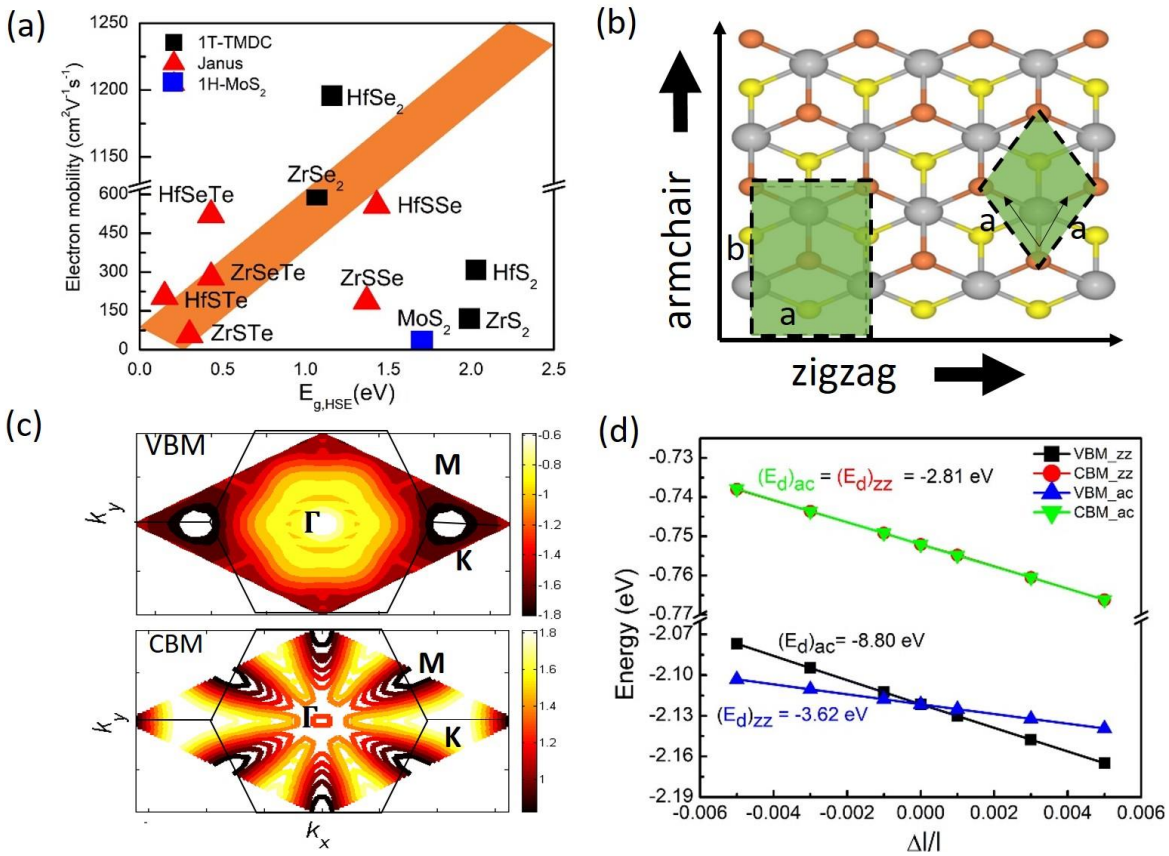

Figure 3. 10 (a) Acoustic phonon-limited electron mobility and energy band gap calculated using the formulation of Lang et al.[177] and HSE06 respectively. The color bar inclined at 45° is for guiding the eye. (b) Schematic diagram of the optimized structure used to calculate charge carrier mobility using a supercell having an orthorhombic symmetry. (c) Contour plots for momentum dependent energy dispersion of valence band maximum (VBM) and the conduction band minimum (CBM) in the BZ. Energy is in units of eV. (d) Variation in VBM and VBM energies with uniaxial strain applied along in-plane transverse directions, namely, zig-zag (zz) and arm-chair (ac). E_d denotes the deformation potential and is given by the slope of the lines in the figure.

In 1H-MX_2 (M=Mo and W; X = S, Se, and Te) monolayers, the VBM and the CBM are bonding and anti-bonding states arising from the hybridization between metal-d and chalcogen-p states. However, in 1T-MX_2 (M=Zr and Hf; X=S, Se, and Te) monolayers, the VBM and CBM are decoupled, as the former and the latter are primarily comprised of chalcogen-p and metal-d states.

Strain brings about two kinds of effects on the absolute energies of the VBM and CBM. First of all, the kinetic energy (KE) of the state, which is proportional to the k^2 or $(2\pi/l)^2$ (k is reciprocal-lattice vector in the extended BZ and l is the interatomic bond length) decreases when the interatomic lattice constant of the 2D material increases with the application of uniaxial tensile strain [181]. Secondly, how the band edges shift with the application of strain determines the relative magnitude of the deformation potential for holes and electrons. The

shift in the band edges with strain is controlled by the nature and composition of the band edges.

The valence and conduction band edges, VBM and CBM, are coupled in 1H-MX_2 monolayers. With the application of tensile strain, the orbital overlap between metal-d and chalcogen-p states decreases. As a result, the CBM(VBM) shifts down(up) in energy to reduce the energy splitting between the band edges[182],[180]. The upshift in the VBM partially counteracts the downshift in its kinetic energy, resulting in a small deformation potential for holes. While the downshift in CBM adds to the drop in its kinetic energy, thereby causing a large deformation potential for electrons. As the carrier mobility is inversely proportional to the square of the deformation potential, the hole mobility is higher than the electron mobility in 1H-MX_2 monolayers.

On the other hand, the band edges are decoupled in 1T-MX_2 monolayers. The band width of the conduction and valence bands narrows with the application of tensile strain [144]. Consequently, the absolute energy of CBM (VBM) shift up (down) with the application of strain, leading to an increase in the energy splitting between CBM and VBM. The upshift in CBM energy partially neutralizes the drop in its kinetic energy, thereby causing a low deformation potential for electrons. The downshift in VBM energy and the drop in its kinetic energy add up, resulting in a large deformation potential for holes. As a consequence, the electron mobility becomes higher than the hole mobility, as clearly depicted in Figure 3.10 (d). The electron mobility in Group IVB dichalcogenide monolayers and their Janus counterparts is much higher than that in Group-VI dichalcogenide monolayers [178,183],[180], owing to lower deformation potential in the former. Among all Janus monolayers, HfSSe and HfSeTe show the highest electron mobility.

The deformation potential for holes is found to be highly anisotropic, while the same for electrons is isotropic, as shown in Figure 3.10 (d). The large deformation potential for holes along the arm-chair direction will lower the hole mobility considerably along the arm-chair direction.

The hole effective mass is found to be isotropic, whereas electron effective is anisotropic. This is attributable to the anisotropy in the momentum dependent energy distribution of the conduction band and isotropy in the same for the valence band about their extrema, as shown in Figure 3.10 (c). As the VBM in 1T-monolayers lie at the Γ point, the valence band energy gets isotropically distributed around the Γ point of BZ along the k_x and k_y directions, while the occurrence of CBM at the M point in the BZ causes an anisotropic distribution in the conduction band energy and its curvature around the M point along the k_x and k_y directions in momentum space. As a result, this causes an anisotropy in the electronic effective mass. The

electron effective masses along the k_x (zig-zag) direction are found to be nearly $1/10^{th}$ of that along the k_y (arm-chair) direction, which is consistent with earlier findings [183]. This significantly lowers the electron mobility along the arm-chair direction. The detailed parameters leading to the calculation of charge carrier mobilities in 1T-Group IVB semiconducting monolayers and their Janus counterparts are tabulated in Table 3.6. It may be noted here that the large anisotropy in the effective mass for electrons and the deformation potential for holes can be captured in the more robust formalism for the calculation of carrier mobility introduced by Lang *et al.* [eqn. (3.8)] and not in the original one by Bardeen and Shockley [eqn. (3.7)]. Therefore, eqn. (3.7) is found to overestimate the carrier mobility relative to the experimentally measured ones in Group IVB based TMDCs. The advanced formulation by Lang et al. [eqn. 3.8] lowers the carrier mobility estimate with respect to the one given by Bardeen and Shockley [eqn. (3.7)]. The former agrees with the experimentally measured ones in Zr and Hf based dichalcogenides [140,143,184,185] in the order of magnitude. Takagi formulation, based on the original one by Bardeen and Shockley, adopted in our work [183] incorporates the anisotropy in effective mass and not the same in deformation potential and the elastic constants. However, the erroneously small deformation potential used in an earlier work [183] has given a disputably high electron mobility in the Group IV B TMDCs.

3.4 Conclusion

In summary, inversion symmetry in centrosymmetric Group IVB transition metal dichalcogenide (TMDC) monolayers occurring in 1T phase is broken upon the formation of its Janus structures and in turn, piezoelectricity is induced. The atomic scale origin of the high level of piezoelectricity induced in these Janus structures in Group IVB TMDC monolayers has been ascertained *via* first-principles density functional perturbation theory. Quantitatively, the piezoelectric constants have been split into their electronic and ionic components in order to highlight the dominance of the ionic contribution to the piezoelectric coefficient. Piezoelectric coefficient (d_{22} = 4.68 - 14.58 pm/V) in the Janus structures in Group IVB TMDC monolayers are found to be much higher than that in single layer 1H-MoS_2 (d_{11} = 2.99 pm/V). Dynamical, mechanical and thermodynamic properties confirm the all-around stability of these monolayers. The monolayers are more flexible with a Young's modulus much smaller than other 2D materials, such as graphene and Group VI TMDCs, e.g., the most widely studied MoS_2. The smaller Young's modulus in these materials resulting from the weaker M–X/Y bond strength imparts an enhanced flexibility to these materials, making them a good choice for their practical applications in-plane strain engineering. A colossal enhancement in the piezoelectric coefficients in Janus HfSSe is observed under the application of uniaxial tensile strain along the arm-chair direction, where d_{22} reaches 123.04 pm/V at 9% strain, which reaches the level

of the piezoelectric coefficients in the state-of-the-art perovskites. The advanced formulation of Lang *et al*.[177] is able to incorporate the anisotropy in the electron effective mass and hole deformation potential in calculating the acoustic phonon limited carrier mobility. Therefore, the carrier mobility computed using this formulation reaches closest to the experimentally measured ones in 1T Group IVB TMDC monolayers [140,143,184,185]. Takagi formulation [183] has been used in the calculation of electron mobility in 1T Zr and Hf-based disulphides and diselenides. Although the Takagi formulation considers the anisotropy in effective mass along the longitudinal and the in-plane transverse direction, the erroneously low deformation potential calculated in that work has overestimated the experimentally measured electron mobility in these 1T TMDC monolayers by an order of magnitude. The remarkable electronic, piezoelectric and mechanical properties predicted in the Janus structures in 1T Group IVB TMDC monolayers along with the robust electron mobility will hopefully be confirmed experimentally in the near future.

Chapter 4

Scavenging waste heat into electricity in selected 2D materials

The thermoelectric figure of merit consists of the thermoelectric power-factor (TPF) scaled by the thermal conductivity (k). Results and discussions on TPF and k are distributed into two sections 4.1 and 4.2.

Section 4.1 deals with avenues to raise the thermoelectric power factor in 2D materials. It is devoted to the study of strain-sensitive and temperature dependent thermoelectric properties in monolayer MoS_2.

Section 4.2 illustrates the lattice vibrational analysis of Hafnium (Hf) dichalcogenide monolayers and reaches the origin of ultralow lattice thermal conductivities (k_L).

4.1

Strain sensitive thermoelectric properties in single layer MoS_2

Based on the work published in:

Dimple, Nityasagar Jena, and Abir De Sarkar, "Compressive strain induced enhancement in thermoelectric-power-factor in monolayer MoS_2 nanosheet", ***Journal of Physics: Condensed Matter*** 2017, 29, 225501

4.1.1 Introduction

An in-depth understanding of the nanoscale Physics in 2D materials may open up new avenues for designing high performance thermoelectric materials [186]. Graphene, the first two dimensional material discovered and studied, shows extraordinary electronic properties such as ultrahigh mobility [187] as well as super high thermal conductivity [188]. However, the pristine graphene, is a Dirac semi-metal, having zero band gap [189] and a very small value of Seebeck coefficient (S) [190], which precludes its application in electronics and thermoelectric devices. Layered transition metal dichalcogenides (TMDCs) such as MX_2 (M=Mo, W etc.; X= S, Se, Te) have drawn a great deal of attention owing to their stable crystal structure at ambient conditions and intrinsic semi-conducting nature. TMDCs retain hexagonal honeycomb motif in their lattice structures, without undergoing any surface reconstruction even after they are thinned down to monolayers. Among the family of TMDCs, MoS_2 has been most widely studied [10,16,17,191–199]. The thermoelectric properties in a few layer to bulk MoS_2 have been theoretically investigated [200–202]. ML-MoS_2 has been found to be a reasonably good thermoelectric material among these 2D materials [65]. Kedar et al. [203] have observed the thermoelectric power factor of ML-MoS_2 to be 8.5 mW/mK^2 in their experiments conducted at room temperature, which is the highest among all thermoelectric materials and twice that of commercially used bismuth telluride (Bi_2Te_3). Hasan et al. [204] found poor response in the thermoelectric power factor in ML-MoS_2 supported on substrates. Contrarily, they found the thermoelectric power factor in suspended ML-MoS_2 to reach high values of up to ~ 28 mW/mK^2 at 300 K, corresponding to an electron concentration of 10^{12} cm^{-2}. Zelin et al. reported the thermal conductivity and ZT of ML-MoS_2 to be 116.8 W/mK and 0.26 at 500 K [65]. Large Seebeck coefficient in ML-MoS_2 has been experimentally demonstrated by Buscema et al. [33] to be tunable between -4x10^2 μV/K and -1x10^5 μV/K *via* a controlled application of the external electric field. Thermoelectric properties in TMDCs which stabilize in 1T phase have also been explored: 1T-$SnSe_2$ monolayer shows a higher thermoelectric performance with p-type doping than with n-type doping [76]. Monolayer TMDCs have been found to be superior to the nanotubes in the thermoelectric (TE) performance [206]. Hybridization and doping are commonly explored avenues in improving the TE performance. SiGe alloys, hybrid BN/graphene and MoS_2/WS_2 nanoribbons show higher thermoelectric properties than single nanostructures [207]. It has been generally observed that the thermoelectric power factor or figure-of-merit of a material is enhanced upon doping. This enhancement in TE power-factor is found to be maximized at an optimal doping concentration of p or n type dopants. However, introducing hybrid interfaces or doping is accompanied by the complexity of these processes,

which are in no way benign. Moreover, a permanent change is brought about in the material by these processes. Properties in nanomaterials are reversibly alterable by the application of mechanical strain within the elastic limits. Additionally, the application of strain is a gentle and a simple technique, and free from harsh treatments. Recently, enhancement in thermoelectric properties have been reported in monolayer ZrS_2 and $PtSe_2$ nanosheets *via* the application of mechanical strain [208,209]. This work focuses on optimizing the thermoelectric response of ML-MoS_2 nanosheet by the application of mechanical strain. To the best of our knowledge, no prior study was done to alter or improve the thermoelectric properties in ML-MoS_2 by adopting approaches other than doping. Therefore, in this chapter, the variation in the thermoelectric properties in ML-MoS_2 with different types of strain has been elucidated and the underlying mechanism has been unveiled through a thorough and a systematic theoretical investigation.

4.1.2 Computational Details

First-principles calculations have been conducted using *ab-initio* density functional theory (DFT) in conjugation with all-electron projector augmented wave potentials [151] and the Perdew-Burke-Ernzerhof (PBE) generalized gradient approximation (GGA) [106,210] for the electronic exchange and correlation, as implemented in the Vienna Ab initio Simulation Package (VASP) [149,150,211,212]. A $16 \times 9 \times 1$ Γ-centered k-mesh was sampled to optimize the geometry of ML-MoS_2. The energy cut-off for the expansion of the electronic wave functions in plane-wave basis was chosen to be 500 eV throughout the calculations. All atomic co-ordinates were relaxed until the atomic forces reached 0.01 eV/Å, while the total energy convergence criterion between successive self-consistent cycles was set at 10^{-5} eV. A vacuum thickness of more than 14 Å was used to minimize the spurious interactions between the periodic images of the slab. For all the strained systems, only the ionic relaxations have been carried out while the scaled lattice constants have been held fixed.

For the investigation of thermoelectric properties, semi-classical Boltzmann transport theory was used, which enables calculation of the temperature and doping level-dependent thermo-power and other thermoelectric (TE) parameters such as Seebeck coefficient, electronic conductivity, Hall coefficients etc. on the basis of electronic structure calculations performed using VASP. All the TE properties have been calculated within the constant scattering time approximation (CSTA). The CSTA is based on the assumption that the scattering time is weakly sensitive to energy. It is valid so long as the electron relaxation time does not vary strongly with energy on a scale of $k_B T$, and the rigid band model as implemented in BoltzTraP [213] code holds good. By using Fourier series expansion, the BoltzTraP code fits the ab-initio electronic band structure to an analytic function while maintaining the crystal symmetry as

such. As ML-MoS_2 is found to be structurally stable up to 900 K [214]; so, the present study has been confined within the temperature limit of 900 K.

The acoustic phonon limited electron mobility calculated in an independent study [179] and partially presented here is based on effective mass and deformation potential approximation proposed by Bardeen and Shockley [176]. This approach has been extensively used [178,215–217] to study charge carrier mobility in 2D materials using the relation, $\mu(\text{mobility}) = 2e\hbar^3 C_{2D}/3k_B T|m^*|^2 E_{2D}^2$, where in-plane elastic stiffness constant is designated as C_{2D}, effective mass as m^* in units of rest mass of electron m_e, acoustic phonon limited deformation potential as E_{2D} and relaxation time as $\tau = m^*\mu/e$.

4.1.3 Results and Discussion

This section is systematically organized into the following sub-sections.

4.1.3.1 Structural parameters

ML-MoS_2 nanosheet consists of a hexagonal honeycomb motif akin to graphene, in which Mo sub-lattice layer is sandwiched between two S sub-layers on either side. It shows strong covalent bonding forming a trigonal prismatic co-ordination in which each Mo atom is coordinated with six S-atoms, bringing about 1H-phase. While bulk MoS_2 shows 2H-phase belonging to D_{6h} point group. To realize the application of mechanical strain along two non-equivalent lattice directions namely, the zigzag (ZZ) and the armchair (AC) directions, the hexagonal primitive unit cell geometry has been purposefully changed into an orthorhombic supercell (rectangular in 2D) which contains two Mo atoms and four S atoms. Upon geometry optimization, supercell lattice dimension reach a=3.17Å and b=5.50 Å, as shown in Figure 4.1.1, which agrees well with the lattice constants reported using GGA-PBE XC functional [155]. To study the effect of different types of mechanical strain such as uniaxial strain, biaxial strain and shear mode of strain, the lattice constants have been varied from 0 to ± 9% with respect to the unstrained value in steps of 1%. The phonon dispersion at 9% tensile and compressive strain provided in Fig. 4.3.2 shows the dynamical stability in ML-MoS_2 under the application of ±9 % strain. ML-MoS_2 is found to be unstable for strain greater than 9% [164]. Positive and negative strain % corresponds to tensile and compressive strain respectively. Besides, two types of shear strain, namely, Type-I and Type-II have been studied. In Type-I, tensile strain is applied along the zig-zag direction, while compressive strain of the same magnitude is applied simultaneously along the arm-chair direction. While Type-II is the other way around, where the ML-MoS_2 is compressed along the zig-zag direction while it is stretched

by the same magnitude along the arm-chair direction.

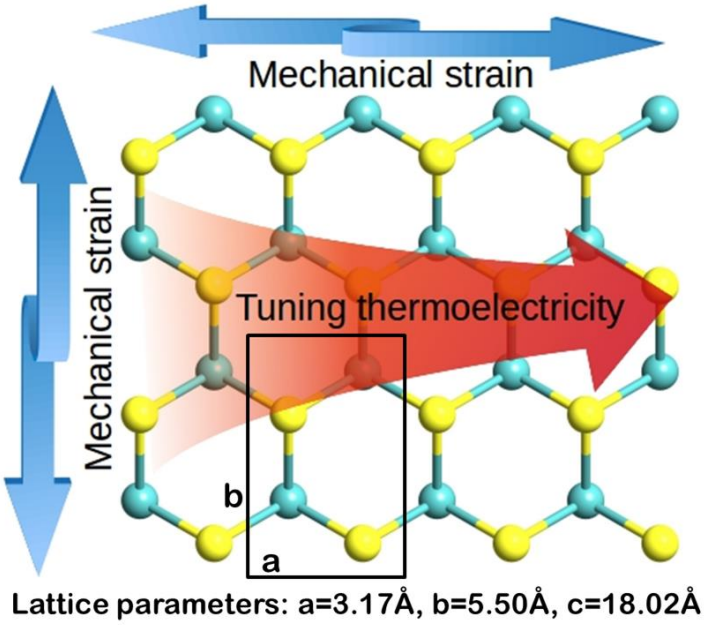

Figure 4.1. 1 Optimized geometry of monolayer MoS_2 nanosheet (Top view). The Mo and S atoms are represented by cyan and yellow color respectively. The arrows indicate tunability in the thermoelectric properties *via* application of mechanical strain.

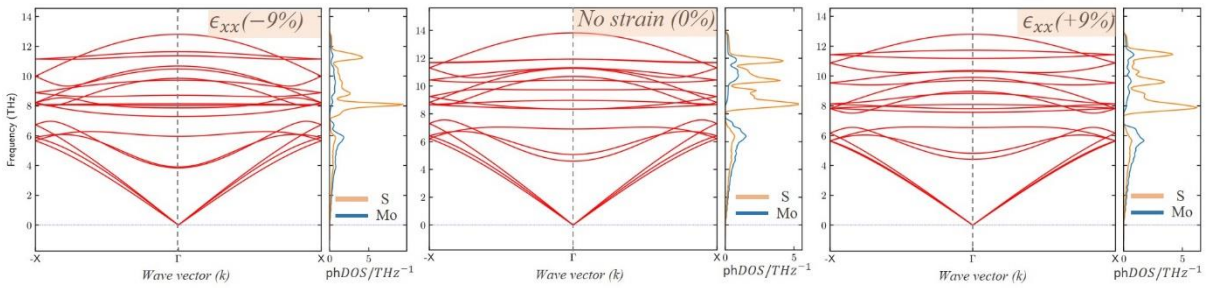

Figure 4.1. 2 Phonon band structure at no strain (0%) and under a compressive and tensile strain of 9% along the zig-zag direction in ML-MoS_2. The absence of any imaginary frequency confirms the dynamical stability in ML-MoS_2 under ±9% strain.

4.1.3.2 Thermoelectric transport properties

The thermoelectric transport coefficients such as Seebeck coefficient (S), electrical conductivity (σ) and relaxation time-scaled thermoelectric (TE) power factor ($S^2\sigma/\tau$) have been calculated as a function of chemical potential (μ) and plotted in Figure 4.1.2. The high Seebeck coefficient of 2688 μV/K at $T = 300\ K$ arises mainly from its large band-gap of 1.68 eV. The value of $S^2\sigma/\tau$ in the n-region (i.e., for μ > 0) is found to be 11.82 x 10^{10} $Wm^{-1}K^{-2}s^{-1}$ (i.e., 1.182 $mWm^{-1}K^{-2}$ or 1.182x10^{14} $\mu Wcm^{-1}K^{-2}s^{-1}$) at 300 K which agrees with the findings of Keder *et*

al. (8.5mWm^{-1}K^{-2}) [203]. It turns out to be slightly smaller than San-Dong's work (3.2x10^{14} μWcm^{-1}K^{-2}s^{-1}) [47] due to a different exchange correlation functional, namely LDA, used in their investigations. To raise the $S^2\sigma/\tau$, which lies low at 300 K, its variation with temperature has also been explored. The peak value of $S^2\sigma/\tau$ is found to rise by an order of magnitude as temperature increases from T = 300 to 900 K, while the peak value of S declines from 2688 to 869.79 μV/K, as shown in Figure 4.1.2. The S and $S^2\sigma/\tau$ values obtained in n-type region (μ > 0) are higher than the ones found in the p-type region (μ < 0) which indicates the higher effectiveness of n-type doping relative to p-type doping in improving the thermoelectric response. A small shift in the peak values of $S^2\sigma/\tau$ towards lower chemical potential has also been observed with the rise in temperature for both types of doping, as shown in Figure 4.1.2

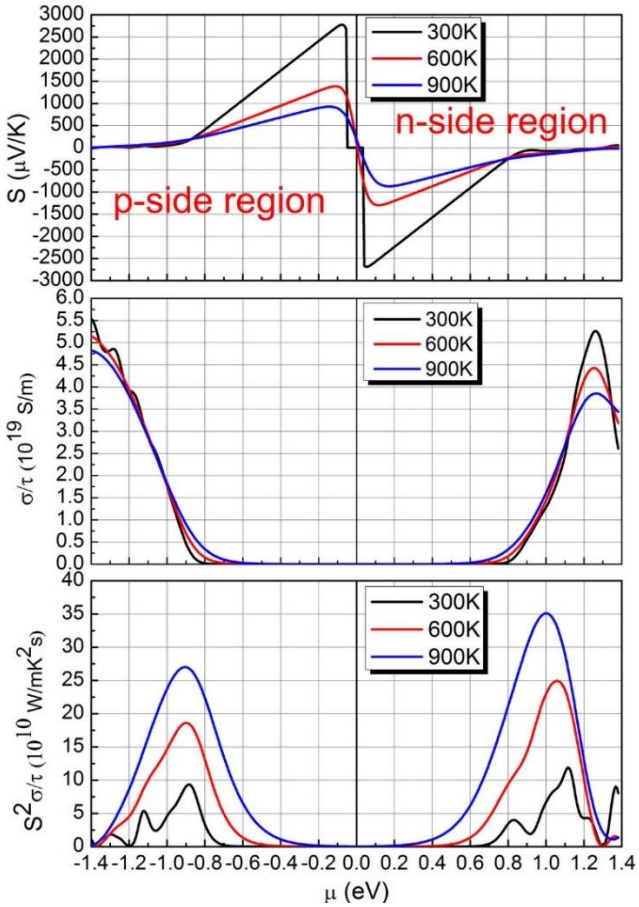

Figure 4.1.3 Variation in Seebeck coefficient, electrical conductivity and relaxation time-scaled thermoelectric power factor with chemical potential, μ at different temperatures (300 K, 600 K and 900 K). μ > 0 corresponds to n-type doping or higher electron concentration relative to the pristine monolayer MoS_2 nanosheet (where μ = 0), while μ < 0 applies to p-type doping or lower electron concentration. μ is the chemical potential.

Seebeck coefficient (S) of monolayer MoS_2 varies dramatically with mechanical strain, indicating the efficacy of strain in controlling thermoelectric (TE) performance in ML-MoS_2,

as shown in Figure 4.1.3. It is found that the value of S increases from 2688 to 2905 μV/K under 3% of uniaxial compressive strain applied along zigzag direction and thereafter it decreases gradually. Similar trend has been observed for 3% of uniaxial compressive strain applied along the armchair direction in which the value of the S rises from 2688 μV/K to 2889 μV/K. For all types of tensile strain, S decreases. S is found to remain insensitive to the application of Shear Type-I and Type-II strain. It is evident from the Figure 4.1.3 that S is more strain sensitive at lower temperatures.

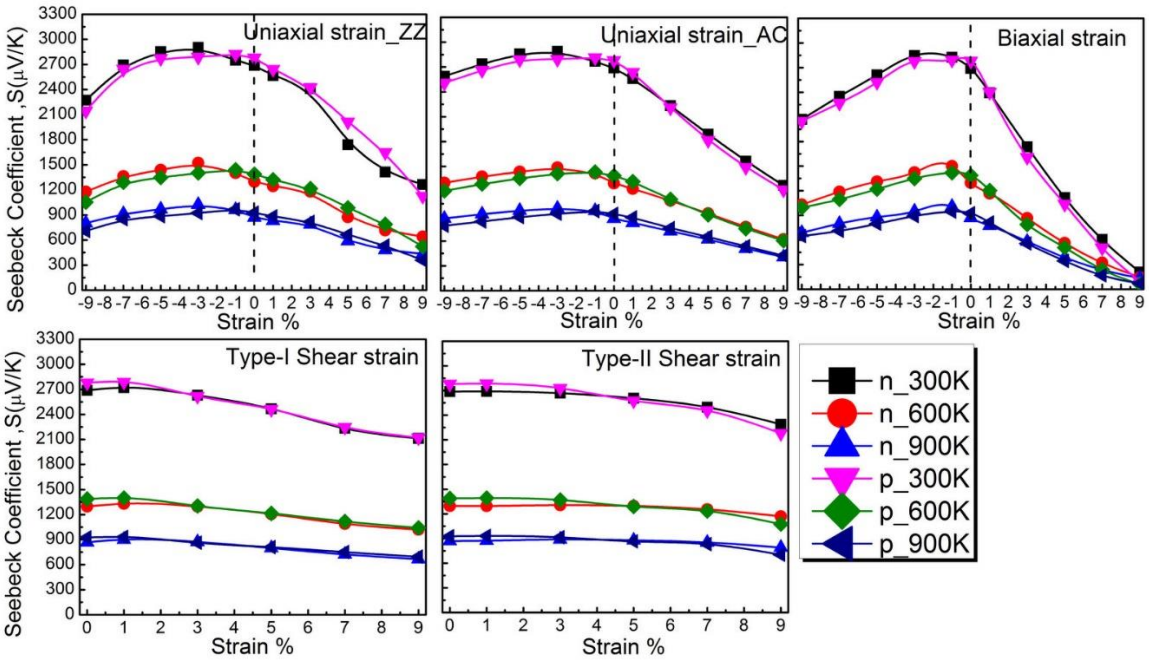

Figure 4.1. 4 Variation in Seebeck coefficient for n-type (μ > 0) and p-type (μ < 0) doping with various types of strain at different temperatures (300 K, 600 K and 900 K), where μ is the chemical potential. Shear strain of type I corresponds to the simultaneous application of tensile strain along the zig-zag direction and compressive strain of equal magnitude along the arm-chair direction. Shear strain of type II is the other way round. Figure labels represent the doping type (n or p) together with the temperature in K.

For an efficient thermoelectric material, $S^2\sigma/\tau$ needs to be high. $S^2\sigma/\tau$ is found to be higher for n-type doping (i.e. μ > 0) than for p-type doping (i.e. μ < 0) and this trend has been observed for all strain types at different temperatures, as shown in Figure 4.1.4. This is attributable to the intrinsic n-type semiconducting nature in ML-MoS_2.

As ML-MoS_2 is intrinsically an n-type semiconductor, strengthening of its intrinsic n-type nature by compressive strain is found to be favorable. Moreover, the increase in band gap and Seebeck coefficient acts in concert as compressive strain increases to 3%. As a result, $S^2\sigma/\tau$ for n-type doping (i.e. μ > 0) undergoes maximal enhancement when the band gap and the Seebeck

coefficient reaches its maximum at 3% uniaxial compressive strain. Of all the three types of compressive strain shown in Figure 4.1.4, uniaxial strain along the zig-zag direction is found to be most effectual. This is attributable to the higher electron mobility and its sensitivity to lattice compression along the zig-zag direction. Band gap of ML-MoS_2 is remain direct under 3% uniaxial compressive strain applied along zig-zag direction, while the electron mobility along this direction drops abruptly from 73.08 $cm^2V^{-1}s^{-1}$ in unstrained, pristine ML-MoS_2 nanosheet to 44.15 $cm^2V^{-1}s^{-1}$ at 3% strain at room temperature (300 K). Along the arm-chair direction, electron mobility reduces to 35.67 $cm^2V^{-1}s^{-1}$ relative to 62.39 $cm^2V^{-1}s^{-1}$ in the unstrained, pristine ML-MoS_2 nanosheet.

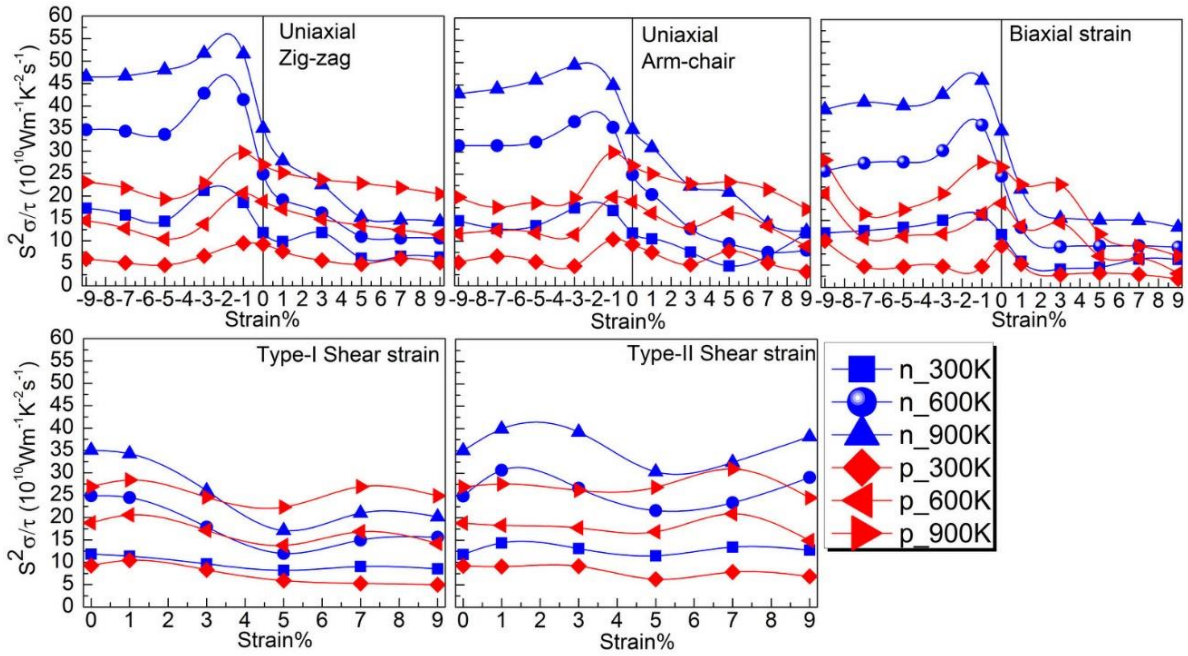

Figure 4.1. 5 Variation in relaxation time-scaled thermoelectric power factor in optimally n and p doped monolayer MoS_2 nanosheet with various strain modes at different temperatures (300 K, 600 K and 900 K). Figure labels represent the doping type (n or p) and the temperature in K.

At T = 300 K, $S^2\sigma/\tau$ increases with uniaxial compressive strain along zigzag and armchair direction and maximizes at 3% strain. $S^2\sigma/\tau$ rises from 11.82 x 10^{10} $Wm^{-1}K^{-2}s^{-1}$ in the strain free condition to 21.25 x 10^{10} $Wm^{-1}K^{-2}s^{-1}$ and to 17.45 x 10^{10} $Wm^{-1}K^{-2}s^{-1}$ under the application of 3% uniaxial compressive strain along the zig-zag and arm-chair direction respectively. $S^2\sigma/\tau$ also increases with temperature. For 3% of uniaxial compressive strain along zigzag direction, $S^2\sigma/\tau$ rises to 42.85 x 10^{10} $Wm^{-1}K^{-2}s^{-1}$ and 51.75 x 10^{10} $Wm^{-1}K^{-2}s^{-1}$ at T = 600 K and 900 K respectively. For 3% of uniaxial compressive strain along armchair direction, $S^2\sigma/\tau$ reaches 36.78 x 10^{10} $Wm^{-1}K^{-2}s^{-1}$ and 49.43 x 10^{10} $Wm^{-1}K^{-2}s^{-1}$ at T = 600 K and 900 K respectively. $S^2\sigma/\tau$ drops down with all types of tensile strains. $S^2\sigma/\tau$ remains insensitive to Type-I shear

strain; however, it increases marginally with the application of 1 to 3 % shear strain of type-II at high temperatures only. In this context, the findings on monolayer ZrS_2 (ML-ZrS_2) are relevant for a meaningful comparison. Although monolayer ZrS_2 is intrinsically an n-type semiconductor; the maximization in its electronic band gap and Seebeck coefficient occurs at 6% tensile strain, which favors the enhancement in $S^2\sigma/\tau$ *via* p-type doping (i.e. $\mu < 0$) in strained ML-ZrS_2 [208] unlike ML-MoS_2. In a theoretical study on a few layer to bulk MoS_2, trilayer and bilayer MoS_2 have been found to experience the maximum improvement in $S^2\sigma/\tau$ under vertical inter-layer compression and biaxial tensile strain respectively, which have been ascribed to the modification in the dispersion in the band edges [200].

The mathematical Goldsmid-Sharp relation given as, $E_g=2e|S|_{max}T_{max}$ [219] is found to hold good, as the variation in band gap follows the same trend as that of the Seebeck coefficient with strain. In this relationship, E_g is the band gap, while S_{max} is the maximum value attained by the Seebeck coefficient at that temperature. The above relation has been found to be valid with all types of strain studied, as shown in Figure 4.1.5. This signifies the sensitivity of both electronic and thermoelectric parameters to strain. Figure 4.1.5 (a) shows that the band gap (E_g) as well as *S* increases with uniaxial lattice compression along zigzag direction which reaches its maximum at 3% strain, and then decreases upon further compression. Similar trend has been found for uniaxial strain applied along the armchair direction. 3% of uniaxial compressive strain along zigzag direction and armchair direction increases the band gap from 1.68 eV in unstrained, pristine ML-MoS_2 to 1.82 eV and 1.85 eV respectively; however, the band gap decreases with tensile stain.

To realize the application of uniaxial compressive strain in actual experiments, MoS_2 monolayer nanosheet needs to be deposited first on a flexible substrate like polyethylene terephthalate (PET) [59]. Then, the substrate needs to be bent mechanically upward [7,220] in order to induce uniaxial compressive strain in the MoS_2 monolayer nanosheet.

Finally, in order to realize a good thermoelectric performance or a high figure of merit, the thermal conductivity needs to be lowered, in addition to enhancing the thermoelectric power factor. In this context, the lattice heat capacity of ML-MoS_2, which is mainly contributed by phonons, has been calculated. It is found to be 63.1 J/mol/K, which agrees well with previous theoretical findings [221]. The lattice specific heat is found to drop to 62.82 and 62.71 J/mol/K under 3% uniaxial compressive strain applied along zig-zag and arm-chair directions respectively. Under the application of 3% biaxial compressive strain, the same reduces to 62.31 J/mol/K. As the thermal conductivity, *k* is directly proportional to specific heat, the reduction

in specific heat implies an attenuation in thermal conductivity and in turn, a high ZT.

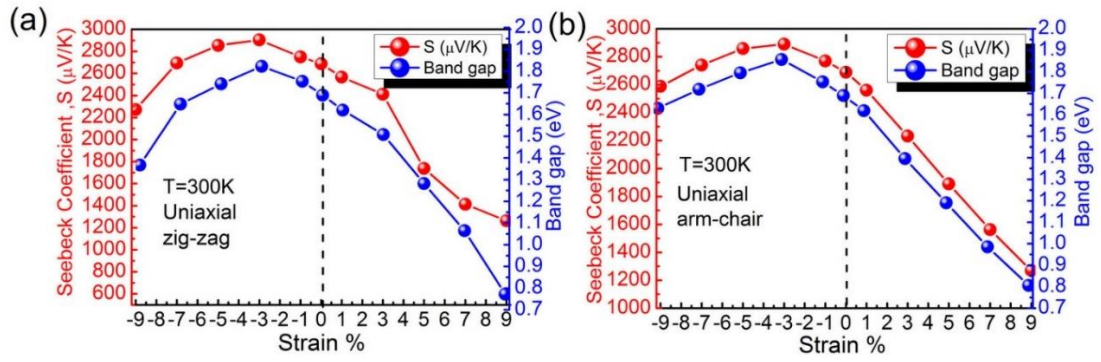

Figure 4.1. 6 Variation in (a) Seebeck coefficients and (b) electronic band gap with uniaxial strain applied along zig-zag and arm-chair directions, showing the validity of Goldsmid-Sharp relation

4.1.4 Conclusion

Thermoelectric (TE) properties in monolayer MoS_2 (ML-MoS_2) nanosheet have been found to be sensitive to the application of mechanical strain, implying that strain can serve as an important avenue in tuning the thermoelectric properties in 2D semiconducting transition metal dichalcogenides. Of all the strain types studied, compressive strain is found to be most effective. Again, out of the three modes of compressive strain, uniaxial strain along the zig-zag direction is found to be most effectual due to the higher electron mobility and its sensitivity to lattice compression along this direction. Relaxation time-scaled thermoelectric power factor is found to be higher upon n-type doping as compared to p-type doping. As a result, the maximal enhancement in $S^2\sigma/\tau$, upon optimal n-type doping, is found to occur under the application 3% of uniaxial compressive strain, when the electronic band gap and Seebeck coefficient, S reaches its maximum. At T = 900 K and 3% of compressive strain along zig-zag direction, the thermoelectric power factor is found to attain its maximum value of 51.75 x 10^{10} $Wm^{-1}K^{-2}s^{-1}$.

4.2

Low lattice thermal-conductivities in Hafnium based TMDCs

4.2.1 Introduction

Apart from the thermoelectric power factor, the term occurring in the denominator of the figure of merit is equally important in thermoelectrics. Lowering the thermal conductivity (k_L) is necessary for enhancing its thermoelectric figure of merit (ZT). Therefore, the factors responsible for a low or ultralow k_L in a thermoelectric material is essential for the purpose of designing a novel thermoelectric material with a superhigh ZT. Group VI MX_2 (M = Mo, W; X = S, Se, Te) monolayers have captivated a great deal of research interest due to their superior electronic and optical properties as compared to their corresponding bulk counterparts. Typical monolayers of MoS_2 and WSe_2 exhibit ZT values of 0.11 [65] and 0.7 [222] at elevated temperatures > 500-900K. The main cause of such a low ZT is high k_L, which is as large as 100 $Wm^{-1}K^{-1}$ for MoS_2 [65] at 300K and larger than 40 W m^{-1} K^{-1} for WSe_2 [222]. It is worth noting that all of these explored monolayer TMDCs have a hexagonal 1H-type crystal structure. Akin to 1T-CdI_2 type structure, the Group IVB TMDCs 1T-MX_2 (M = Zr, Hf; X=S, Se) monolayers, which have been synthesized recently, show great air-stability in thier 1T-phase [223],[141],[224]. These monolayers have been predicted to have much lower k_L value of 3.29 $Wm^{-1}K^{-1}$ for 1T-ZrS_2 [208], 1.2 W m^{-1} K^{-1} for 1T-$ZrSe_2$ [225], 2.92 $Wm^{-1}K^{-1}$ for 1T-HfS_2 [226] and 1.8 W m^{-1} K^{-1} for 1T-$HfSe_2$ [225] at 300 K. Till now, such low k_L values are found in the well-known peer thermoelectric materials such as PbTe [227] (2.2 $Wm^{-1}K^{-1}$), Bi_2Te_3 [228] (1.6 $Wm^{-1}K^{-1}$) and SnSe [229] (2.6 $Wm^{-1}K^{-1}$). Concomitantly, the application of external mechanical strain have been shown to induce energy valley degeneracy [84,226,230–236], i.e. multiple extrema in the band edges around the same energy due to their degenerate orbitals and multiple pockets of a single band in the Brillouin zone (BZ), which facilitates thermoelectric properties such as high thermoelectric Seebeck coefficient. These findings indicate that monolayer TMDCs with CdI_2 type structure may have better thermoelectric performance due to their much lower k_L than those of 1H-type Group VI TMDCs monolayers. In the earlier theoretical analysis, primarily the focus was put on the electronic part of thermoelectric properties and the depth of details of favorable low lattice thermal conductivities was found missing in the existing literature [225,226,237–239]. Therefore, there is still clearly a need for the detailed study of phonon transport properties of these monolayers.

In this chapter, the mechanism underlying the ultralow k_L in 1T-CdI_2 type Hf dichalcogenide monolayers, such as HfS_2 (2.19 $Wm^{-1}K^{-1}$), $HfSe_2$ (1.23 $Wm^{-1}K^{-1}$) and their Janus derivative HfSSe (1.78 $Wm^{-1}K^{-1}$) at 300 K has been revealed. Earlier theoretical studies were limited to either electronic part of the *ZT* or the magnitude of k_L only. Those studies have addressed neither the cause nor the effect of ultralow k_L in such ionic (polar) materials [225,226,237–239]. In the present study, an in-depth study on k_L has been performed, which has been strongly supported by our benchmarking studies on pure 1T-HfS_2 and 1T-$HfSe_2$ systems. We set out calculations by means of first-principles density functional theory driven by linearized phonon Boltzmann transport equations, which are conceptually related to the phonon-phonon interaction strength, as well as vibrational frequency dispersion analysis. The magnitude of Debye temperature and lattice specific heat capacity is found to be lower than the Group-VI TMDCs such as MoS_2. Apart from this, large Γ-point LO-TO splitting is arising from substantially high phonon-electric field coupling which is rooted in the domination of ionic bond character and high Born-effective charges. This effect imparts a striking difference in the lattice thermal conductivities upon incorporation of non-analytical correction (NAC) term. The possible impact of optical phonons on the thermoelectric properties has been discussed. Small magnitudes of phonon lifetimes combined with reduced group velocities lead to severely low lattice thermal conductivities, as found in this work. Besides, the calculated mode Grüneisen parameter is found as high as ~ 2.0 at $300\ K$, which is a fairly large value in 2D materials, indicating a strong anharmonicity in these monolayers.

4.2.2 Computational Details

First-principles based density functional theory has been employed to calculate accurate second-order harmonic and third-order anharmonic interatomic force constants (IFCs) via finite-displacements and total energy calculations as implemented in Vienna Ab-initio Simulation Package (VASP)[148–150,240]. The projected augmented wave (PAW)[151] method and the generalized gradient approximation (GGA) with the Perdew-Burke-Ernzerhof (PBE) [241] exchange-correlation functional have been used. Supercells of $2 \times 2 \times 1$ have been used to obtain the second and third-order IFCs. The valence electronic states have been expanded in the plane-wave basis-sets with an energy cut-off of 400 eV. The energy tolerance of $10^{-8} eV$ has been used for an accurate calculation of the force constants. The BZ integration were performed with $7 \times 7 \times 1$ Monkhorst-Pack grids. The displacement amplitude employed in the calculation of finite displacement was set to $0.03 Å$. These forces are employed to calculate the phonon transport properties, including phonon dispersion relations and phonon-phonon interactions. k_L is calculated with q-mesh of $11 \times 11 \times 1$, and a tetrahedron method is

employed in calculating the imaginary part of self-energy and the phonon lifetime. The phonon dynamics information is then used as the inputs for phonon Boltzmann transport equation (PBTE) calculations, which considers the balance between phonon diffusion driven by small temperature difference and phonon scattering due to various scattering mechanisms. k_L is determined by studying the phonon-phonon interaction processes at different temperatures (See Appendix I). Mode Gruneisen parameter is calculated from the third-order force constant using Phono3py [242] (See Appendix II). We also examined the elastic stiffness of these materials by applying the finite difference method as implemented in VASP [148–150,240].

The splitting between transverse optical and longitudinal optical phonon modes at the zone-centre has been calculated based on the NAC approach [243,244] as implemented in Phonopy [152] and Phono3py [242] (See Appendix III). The static dielectric tensors and Born effective charges required for these calculations are calculated by using density functional perturbation theory (DFPT) as implemented in VASP [115].

4.2.3 Results and Discussions

4.2.3.1 Structure

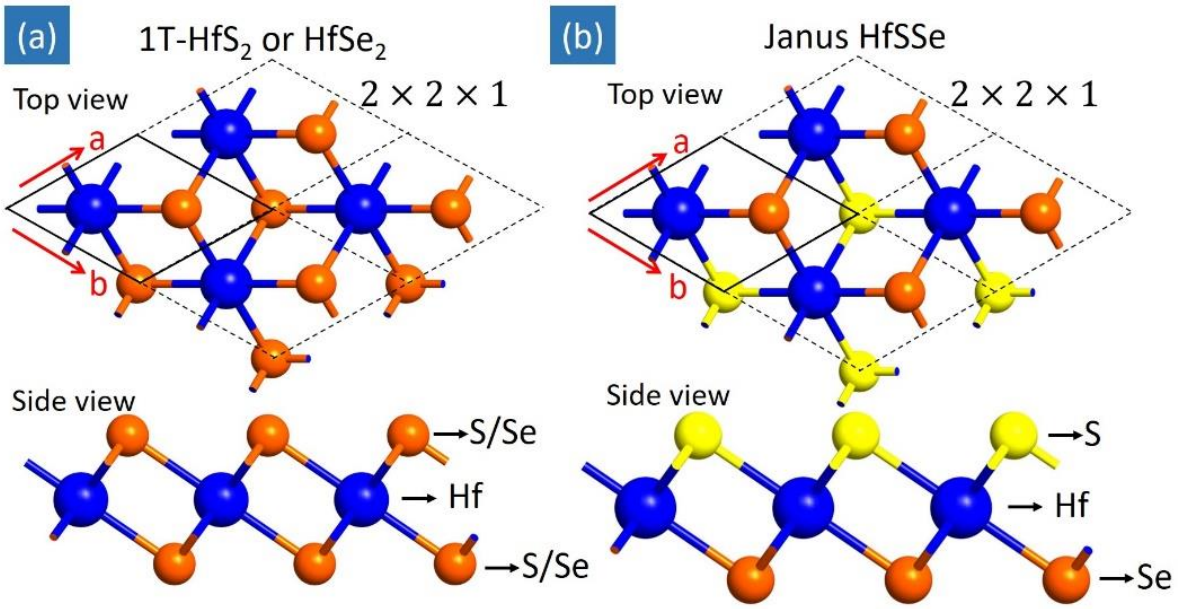

Figure 4.2. 1 Ball and stick model of the optimized atomic structure of 1T-CdI_2 type monolayers (a) HfS_2 or $HfSe_2$ and (b) Janus HfSSe.

As shown in Figure 4.2.1, each of HfS_2 and $HfSe_2$ monolayers share the same trigonal 1T structure akin to 1T-CdI_2 with a centrosymmetric space group $P\bar{3}m1(164)$, whereas Janus monolayer structure of HfSSe (see Figure 4.2.1b) has been created from pristine monolayers by replacing one chalcogen layer (S) by other chalcogen (Se) element. The equilibrium lattice

of monolayer Janus monolayer HfSSe belongs to the non-centrosymmetric space group $P3m1(156)$ which is polar in nature. The PBE-GGA exchange correlation result in the optimized lattice constants of HfS_2 (3.65 Å), $HfSe_2$ (3.72 Å), and HfSSe (3.68 Å), respectively. Our optimized lattice constants for HfS_2 and $HfSe_2$ are consistent with the earlier experimental [245],[246],[247] and theoretical reports [248],[249],[250]; however, the Janus monolayer HfSSe has not been experimentally synthesized as of yet.

4.2.3.2 Lattice thermal conductivity w/o NAC correction

Our k_L calculations are based on harmonic second-order and anharmonic third-order IFCs, which have been calculated using Phono3py [242] code (see APPENDIX I for details) interfaced with VASP [148–150,240]. Temperature is one of the most important controlling parameter which significantly affect the k_L. Figure 4.2.2, demonstrates the temperature dependent of k_L for monolayer HfS_2, $HfSe_2$ and HfSSe on a scale of 100-1000K. At $300\ K$, k_L is $2.19\ Wm^{-1}K^{-1}$ for HfS_2, $1.23\ Wm^{-1}K^{-1}$ for $HfSe_2$ and $1.78\ Wm^{-1}K^{-1}$ for HfSSe. This magnitude of k_L found in monolayer HfX_2 is much lower as compared to their respective bulk counterparts, ~ 7.5 $Wm^{-1}K^{-1}$ for bulk HfS_2 [239] and 8.5 $Wm^{-1}K^{-1}$ for $HfSe_2$ [239]. So far, such a low magnitude of k_L has been observed in the well-known bulk thermoelectric systems such as Bi_2Te_3 [228](1.6 $Wm^{-1}K^{-1}$), PbTe [251],[227] (2.2 $Wm^{-1}K^{-1}$) and SnSe (2.6 $Wm^{-1}K^{-1}$)[229] at 300 K. In Fig. 2, the k_L is decreasing with rise in temperature, as expected for a phonon-dominated crystalline material. At 900 K, k_L reaches its minimum, 0.71 $Wm^{-1}K^{-1}$ for HfS_2, 0.41 $Wm^{-1}K^{-1}$ for $HfSe_2$ and 0.59 $Wm^{-1}K^{-1}$ for HfSSe.

In Figure 4.2.2 (b), the cumulative lattice thermal conductivities (k_c) have been calculated which can explain, how different phonon modes contribute to the total k_L. The curve reflects a slow start in the acoustic mode regime, which grows to the relevant magnitudes, followed by the somewhat steep linear regime and finally a less steep plateau towards the maximum. For this, we normalized the mode-dependent k_C with respect to their respective total k_L. This gives the percentage of each phonon mode towards the k_L. The normalized acoustic-modes phonon frequencies reaching their maximum at 0.44, 0.49 and 0.40 for HfS_2, $HfSe_2$ and HfSSe respectively, contribute of 91%, 89% and 90% respectively. Average contribution of optical phonons to the k_L is about ~12%, which is much higher than the optical phonons of monolayer Group VI MX_2, where it is almost negligible and hence generally ignored. The more details about the phonon mode effects on k_L, will be explained in Section III E.

In the remaining chapter, the various possible aspects that are responsible for low k_L in these monolayers have been explored.

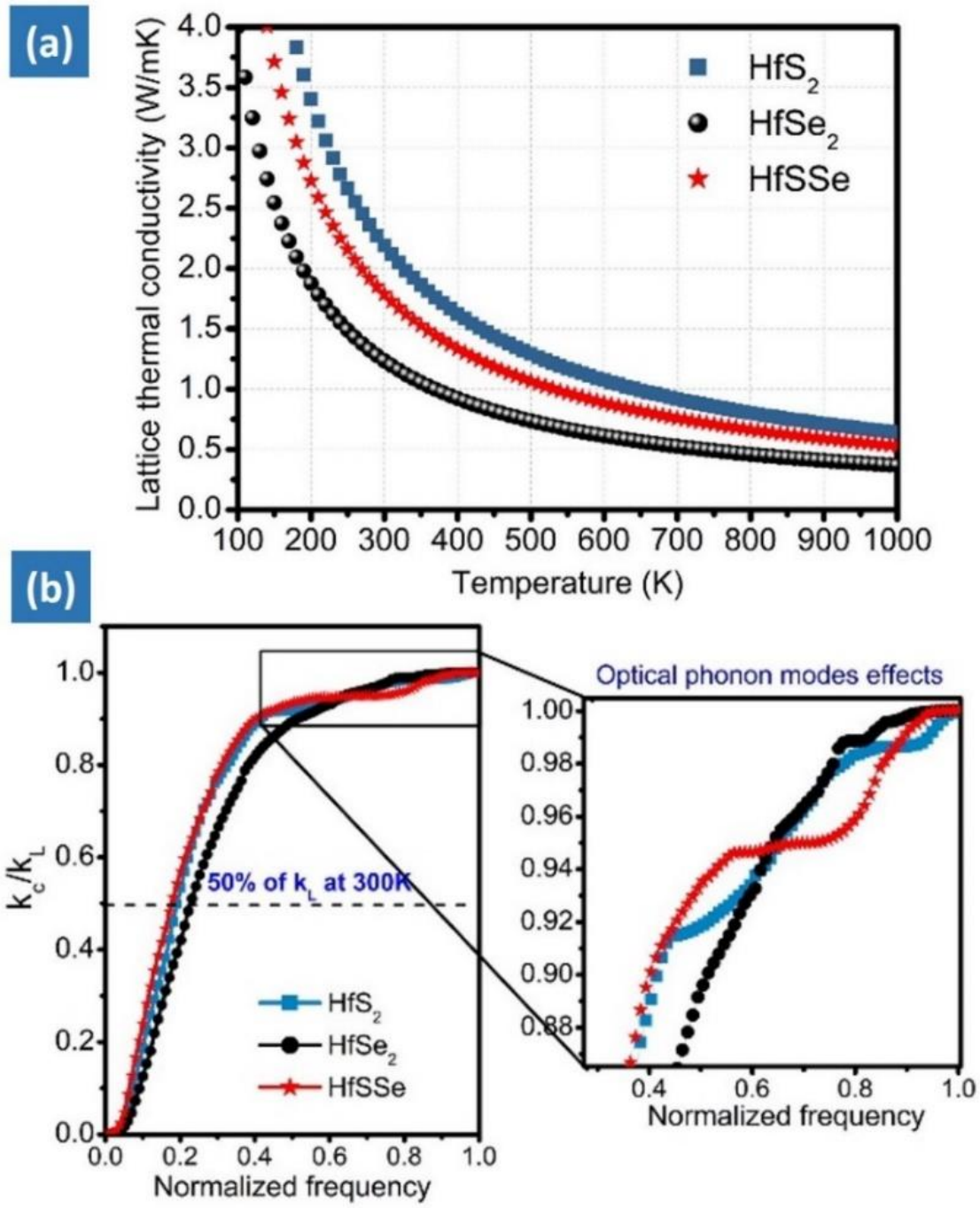

Figure 4.2. 2 (a) Calculated temperature dependent lattice thermal conductivities (k_L) of monolayer HfS_2, $HfSe_2$, and Janus HfSSe. (b) Normalized mode dependent cumulative lattice thermal conductivities (k_C) with respect to an average k_L. The zoom-in view represents some kind of anomaly in k_L, originated from the effect of optic phonon modes.

Table 4.2. 1 Calculated relaxed/optimized lattice constant (a), Average atomic mass ($\bar{M}$) of primitive unit-cell, Young's modulus (Y_{2D}), Debye temperature (θ_D), Born-effective charge tensors, $Z^*_{Hf/S/Se}$ and In-plane ($\epsilon^{\parallel}$) & out-of-plane ($\epsilon^{\perp}$) high frequency static dielectric tensor of HfS_2, $HfSe_2$, and Janus HfSSe monolayers.

Parameters	HfS_2	$HfSe_2$	HfSSe
a (Å)	3.65	3.72	3.68
$\overline{M}$ **(u)**	80.87	112.13	96.50
Y_{2D} **(Nm^{-1})**	79.99	71.85	74.63
θ_D **(K)**	185.20	167.97	166.21
$Z^*_{Hf,xx}$	6.71	7.37	7.01
$Z^*_{Hf,zz}$	0.66	0.52	0.56
$Z^*_{S,xx}$	-3.35	_	-3.62
$Z^*_{S,zz}$	-0.33	_	-0.33
$Z^*_{Se,xx}$	_	-3.68	-3.39
$Z^*_{Se,zz}$	_	-0.26	-0.23
$\epsilon^{\infty,\parallel}$	5.09	7.15	6.34
$\epsilon^{\infty,\perp}$	1.58	1.62	1.61

4.2.3.3 Debye temperature and specific heat capacity

Traditionally, the Debye temperature (θ_D) is known as an important fundamental parameter which is related to the thermal vibrations. It is closely linked to the specific heat capacity and elastic stiffness constant (see Table 4.2.1). In our calculations, we obtained θ_D for different systems by fitting the phonon density of states (PhDOS) at low frequency range, based on Debye-model as implemented in Phonopy code[152]. A generic understanding is based on the fact that materials with low θ_D gives low k_L. The calculated θ_D of $HfSe_2$ (167.97 K) and HfSSe (166.21 K) is comparable to its well-known thermoelectric peer PbTe (164 K)[252]. The lowest θ_D for $HfSe_2$ is resulting from the heavy atomic-mass (178.49u of Hf and 78.96u of Se) and due to low elastic stiffness constants as shown in Table 4.2.1. Actually, low θ_D is advantageous for TEMs because for the temperatures above θ_D, all phonon modes get excited, leads to strong three-phonon scattering process and lowered k_L, while below θ_D, phonon modes begin to freeze out.

Figure 4.2.3 shows the temperature dependency of lattice specific heat capacity. It is observed that the specific heat capacity for these systems follows a T^3 law which is an expected

behaviour in the low-temperature limit and attains saturation values (3R) at high temperatures, which is known as Dulong and Petit classical limit. At 300 K, the specific heat capacity is 17.14 $JK^{-1}mol^{-1}$, 17.57 $JK^{-1}mol^{-1}$, and 18.02 $JK^{-1}mol^{-1}$ for HfS_2, $HfSe_2$, and HfSSe respectively. These values are smaller than single-layer MoS_2 (30.76 $JK^{-1}mol^{-1}$)[253].

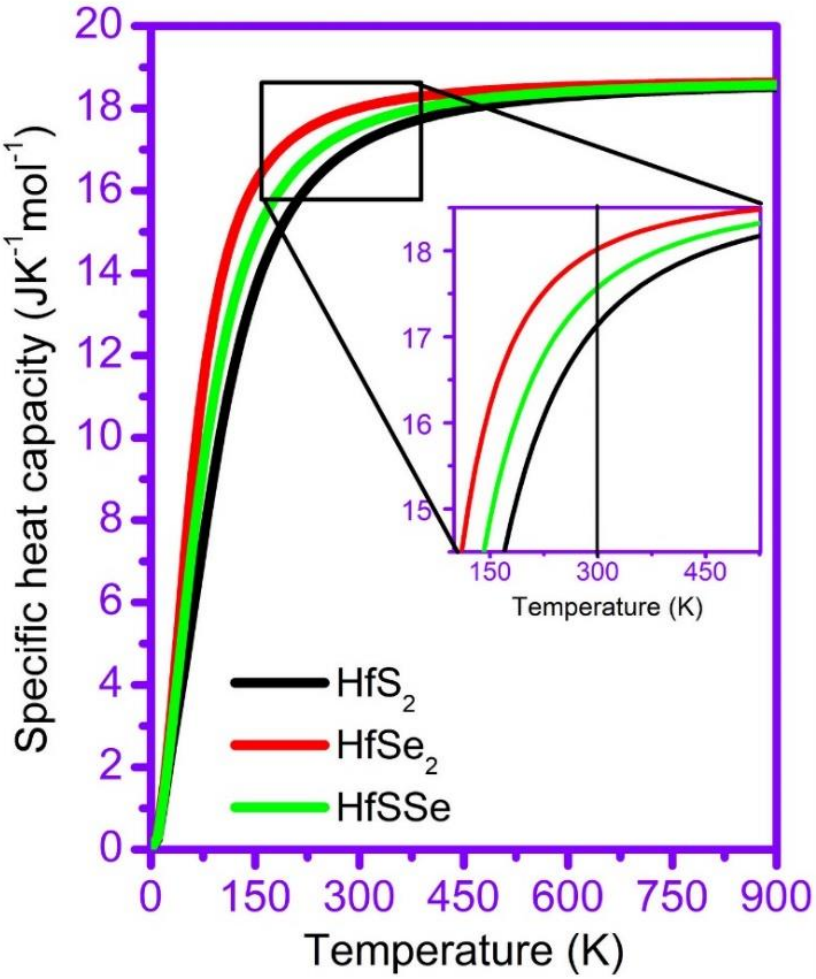

Figure 4.2. 3 Variation in specific heat-capacity of HfS_2, $HfSe_2$ and HfSSe monolayers with temperature. The difference in magnitude at the temperature range of 150 K to 450 K is shown in the inset.

4.2.3.4 Analysis of Phonon Dispersion

Apart from the aforementioned classical description based on θ_D and lattice specific-heat capacity; in this section we analyse the harmonic phonon dispersion and phonon density of states (PhDOS) in order to have a deeper insight into the underlying mechanisms that leads to the low k_L in these monolayers. Figure 4.2.4 (a) depicts the phonon dispersion of HfS_2, $HfSe_2$, and HfSSe monolayers. The absence of imaginary phonon branch in the entire first BZ suggests lattice dynamical stability in these monolayers.

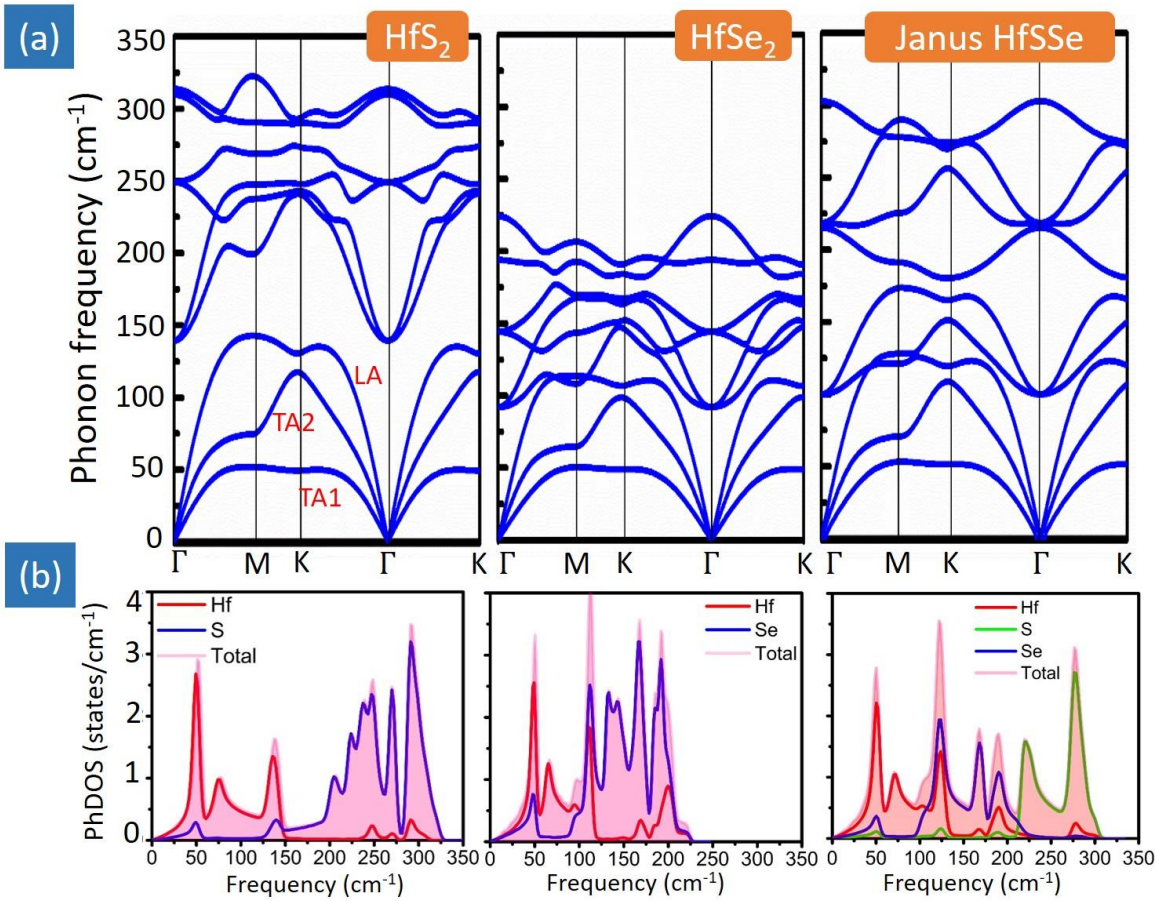

Figure 4.2. 4 (a) Phonon dispersion of monolayer HfS_2, $HfSe_2$, and HfSSe. The least elevated frequency scale is obtained for $HfSe_2$ (b) Atom projected phonon density of states (PhDOS) reveals that low-frequency acoustic modes originate largely due to the vibrations of heavy Hf atoms whereas optical modes originate due to the vibrations of lighter atoms (S and Se).

At a first glance, the observed elevated frequency scale for HfS_2, $HfSe_2$ and HfSSe is 322 cm^{-1}, 224 cm^{-1}, 302 cm^{-1} respectively. The magnitude of this scale is caused by the strength of interatomic bonding forces that facilitate the thermal conduction by increasing acoustic phonon velocities which in turn reduces the phonon scattering rates. Our earlier computational study and other scientific literature on these 2D crystals demonstrate the interatomic bonding in HfS_2, $HfSe_2$, and HfSSe are ionic in nature owing to decoupled or non-hybridised bands in the electronic band structure [254]. In case of $HfSe_2$, the heavy metal/non-metal atom greatly suppresses the phonon dispersion frequencies in $HfSe_2$ and thereby slows down the speed of heat-carrying phonons.

The avoided crossing of acoustic and optic phonon branches is another indication of decoupled acoustic-optical (a-o) phonons. Thus, decoupled a-o scattering is noticable in all the studied monolayers. However, in the monolayer MoS_2, bunching in the acoustic phonon modes is noticed. It leads to the violation of the law of conservation of energy and momenta, which is

necessary for the three-phonon scattering mechanism. Therefore, non-dispersive bunching of acoustic phonon modes in monolayer MoS_2 largely suppresses the scattering mechanism, thereby reducing the scattering rate of acoustic phonons in particular, and in turn, results in a high magnitude of k_L. Acoustic branches in 1T-monolayers are well separated within the BZ, thus, allowing the acoustic phonons to participate in the scattering mechanism. So, high scattering rate of phonons give a low value of k_L. The larger frequency scale, a-o gap between acoustic and optic phonon branches combined with the bunching of acoustic phonon modes in Group VI monolayers considerably reduce the phonon scattering mechanics, which causes a relatively high magnitude of k_L.

Furthermore, in order to identify the phonon branches that affects the k_L, we examine the PhDOS as shown in Fig. 4.2.4 (b). The atom projected PhDOS reveals the low-frequency acoustic modes in these systems to arise mainly from the vibrations of heavy Hf atoms and the optical modes originate due to the vibrations of lighter atoms (S and Se).

4.2.3.5 Phonon-Electric field coupling effect and k_L

A high value of Born effective charges and a large dielectric permittivity in these systems can impact its LO-TO splitting significantly, as shown in Figure 4.2.5 (a) (See Appendix III for numerical details). A large LO-TO splitting is due to a simultaneous coupling between the vibrating ions in the lattice and the polarization field created by atomic vibrations in a polar/ionic crystal in the long-wavelength phonon limit where phonon wave-vector $q \to 0$. In such cases, the behaviour of phonon dynamic matrix get changed at $q \to 0$ and an additional NAC term correction is required for the correct estimation of k_L(see Appendix III). In case of a ML-MoS_2, the Born effective charges (BEC) on Mo and S are small. The polarization field associated with LO-TO phonon branches are very weak (only 2 cm^{-1} LO/TO splitting is due to small mode oscillator strength). Therefore, a weak electronic screening leads to a smaller LO/TO splitting in MoS_2 which is safely ignorable for its contribution to the k_L[255]. On the other hand, in the phonon dispersion of Hafnium based dichalcogenide with (Figure 4.2.5a) and without (Figure 4.2.4a) NAC term the long-range Coulomb interactions are found to have a much stronger effect on its LO mode than other phonon branches. The LO-TO splitting for HfS_2, $HfSe_2$ and HfSSe are 147.7 cm^{-1}, 101.9 cm^{-1} and 59.8 cm^{-1} respectively.

Upon incorporating the NAC term, the magnitude of k_L for HfS_2, $HfSe_2$ and HfSSe are found to increase slightly to 4.1 $Wm^{-1}K^{-1}$, 1.7 $Wm^{-1}K^{-1}$ and 2.2 $Wm^{-1}K^{-1}$ respectively. The LO-TO splitting pushes the LO mode to higher frequencies, which then is no longer available at low temperatures to contribute to phonon scattering. The reduction in the phonon

scattering channel is therefore responsible for the slight rise in thermal conductivity upon the incorporation of NAC term. The LO-TO splitting is larger in HfS_2 than $HfSe_2$. As a result, the rise in lattice thermal conductivity upon incorporation of NAC term is higher in HfS_2 than in $HfSe_2$.

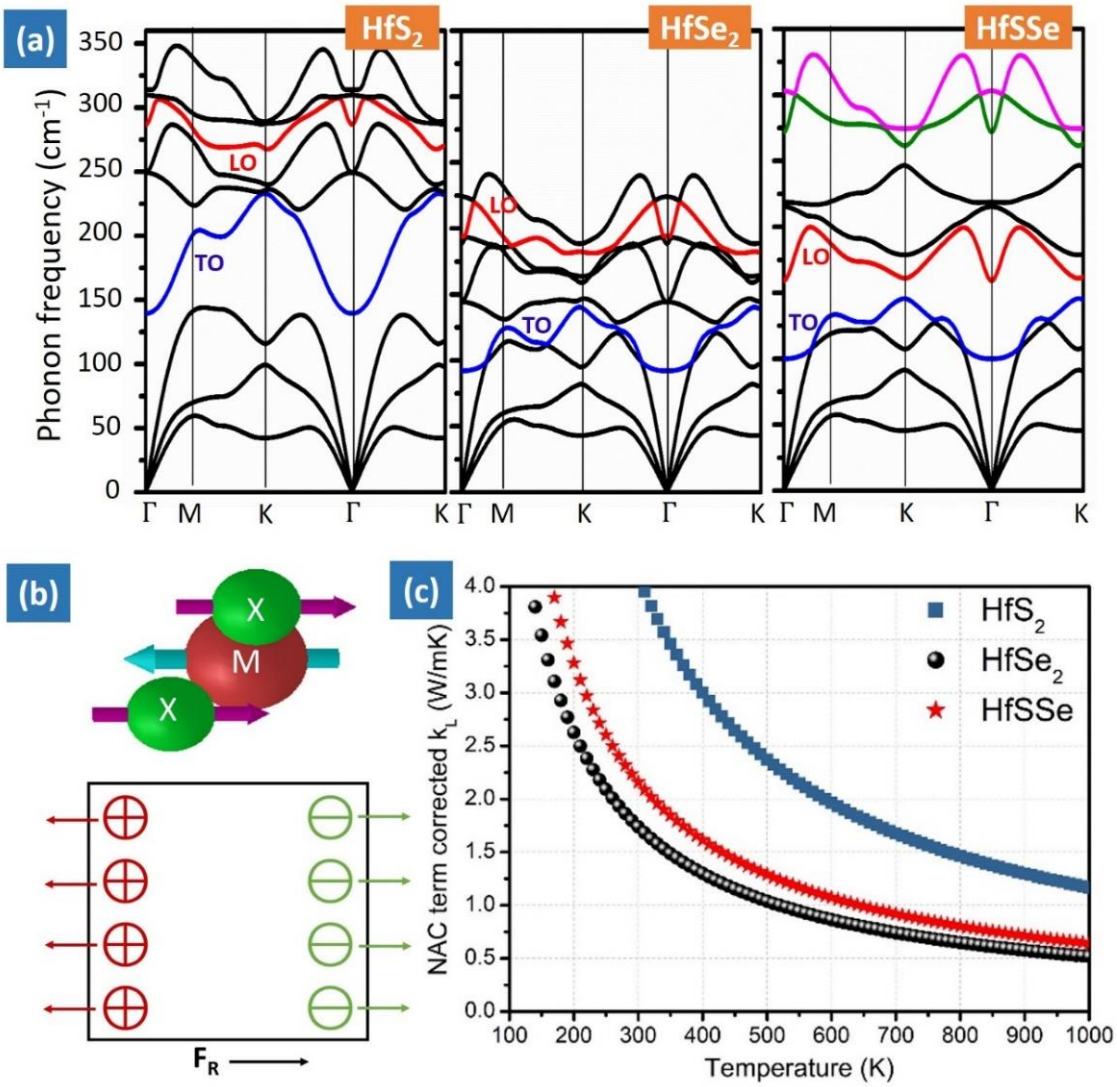

Figure 4.2. 5(a) Non-analytical term corrected (NAC) phonon dispersion spectra of monolayer HfS_2, $HfSe_2$, and HfSSe. The red curve indicate frequency degeneracy lifting LO branch whose frequency gets most affected with NAC, whereas the blue curve is TO branch that remains unaffected. (b) Schematic shows the reverse vibrational motion of positive and negative ions that can be analogous to two oppositely charged parallel plates of a capacitor. The additional restoring force (F_R) associated with LO branch is thus responsible for the lifting of the degenerate LO and TO into non-degenerate singlet branch (c) Lattice thermal conductivity by incorporating the NAC term for each case.

4.2.3.6 Mode specific phonon group velocity

Each phonon mode has a band index (α) and q-dependent phonon group velocity, $v_\alpha(\lambda)$. This mode-specific phonon group velocity can be obtained directly from the phonon eigen-value

equation (Appendix I). Figure 4.2.6 (a-c) represents the x and y components of mode-specific phonon group velocities which follows the order HfS_2> HfSSe >$HfSe_2$. The phonon group velocities are nearly isotropic along x- and y- direction and their magnitude is smaller compared to Group VI MX_2 monolayers. Figure 4.2.6 (d) shows the large zone-centre phonon softening of TO-branch in HfS_2 owing to the long-range interactions. It is responsible for the high optical phonon velocities that are comparable to acoustic phonon velocities and thus, contribute to the k_L. Therefore, the magnitude k_L is found higher in HfS_2 than that of $HfSe_2$ and HfSSe. Furthermore, the low lying TO-branch of $HfSe_2$ and HfSSe are flattened and their energies are much lower than TO-branch of HfS_2, thus have low group velocities as shown in Figure 4.2.6 (d). Existence of a-o gaps in monolayers such as ML-MoS_2 prohibits the optical phonon scattering, resulting in a large phonon group velocities and high magnitude of lattice thermal conductivities at low temperatures.

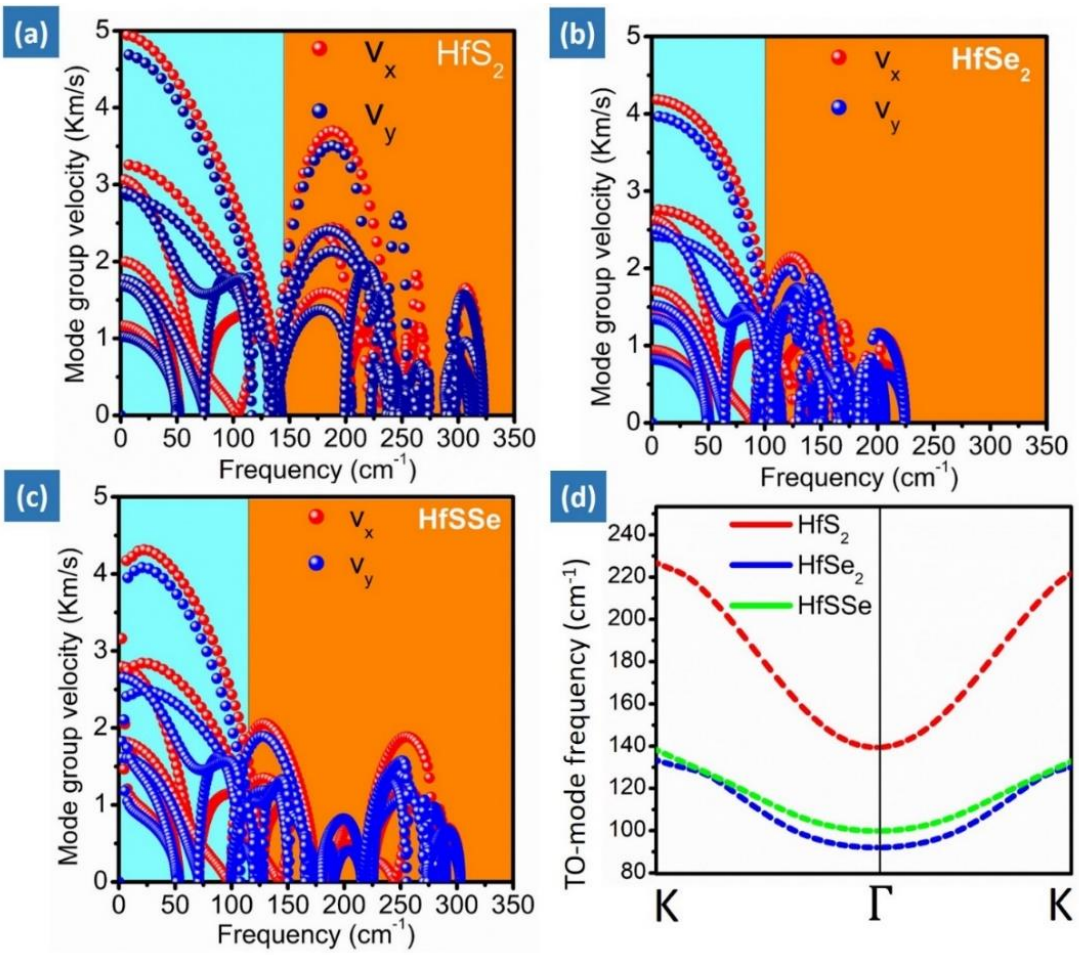

Figure 4.2. 6 (a-c) Mode dependent phonon group velocities of HfS_2, $HfSe_2$, and HfSSe monolayers. Background cyan color indicates acoustic branch and optical phonon in orange. (d.) A comparison of transverse optical (TO) mode for all three monolayers. Large zone-center phonon softening of TO-mode of HfS_2 causes a higher optical phonon velocity which is comparable to the acoustic phonon velocities (as in Figure 4.2.6a).

4.2.3.7 Phonon lifetime distribution

Phonon lifetime plays a vital role in determining the anharmonic phonon scattering rates in a crystalline solid. A finite k_L is an outcome of phonon-phonon scattering. The single-mode relaxation time, τ_λ^{SMRT} can be approximated by the phonon lifetime τ_λ, which is reciprocal of phonon linewidth, $2\Gamma_\lambda(\omega)$:

$$\tau_\lambda^{SMRT} = \tau_\lambda = \frac{1}{2\Gamma_\lambda(\omega)}$$

where $\Gamma_\lambda(\omega)$ takes the form analogous to that of Fermi Golden rule,

$$\Gamma_\lambda(\omega) = \frac{18}{\hbar^2}\sum_{\lambda'\lambda''} |\Phi_{-\lambda\lambda'\lambda''}|^2 \{(n_{\lambda'} - n_{\lambda''} + 1)\delta(\omega - \omega_{\lambda'} - \omega_{\lambda''}) + (n_{\lambda'} - n_{\lambda''})[\delta(\omega + \omega_{\lambda'} - \omega_{\lambda''}) - \delta(\omega - \omega_{\lambda'} + \omega_{\lambda''})]\}$$

where n_λ is the phonon occupation number at the equilibrium,

$$n_\lambda = \frac{1}{\exp(\hbar\omega_\lambda / k_B T) - 1}$$

and $\Phi_{-\lambda\lambda'\lambda''}$ is the strength among three phonons λ, λ' and λ''involved in the scattering event.

In a generic scenario, optic phonons do not directly participate in thermal transport processes due to their low group velocities, yet they can provide essential scattering channels for heat-carrying acoustic phonons. We looked into the distribution of phonon lifetimes at 300 K as a function of phonon frequency with the use of Seaborn Python visualization library as shown in Figure 4.2.7. A smaller lifetime will result in a smaller k_L (See equation in Appendix I). The phonon modes are represented by black dots against the background colour. Regions with a high density of phonon modes are represented by red/orange colour. On the basis of phonon lifetime distributions as shown in Figure 4.2.7(a), it is evident that for HfS_2 there exist two clusters centred about the point where phonon frequency is 7 THz and 8.5 THz. As evident in Figure 4.2.7 in the range of 4-6 THz, the calculated phonon lifetimes of TA LA and TO phonon modes are significantly shortened due to the strong a-o phonon scattering.

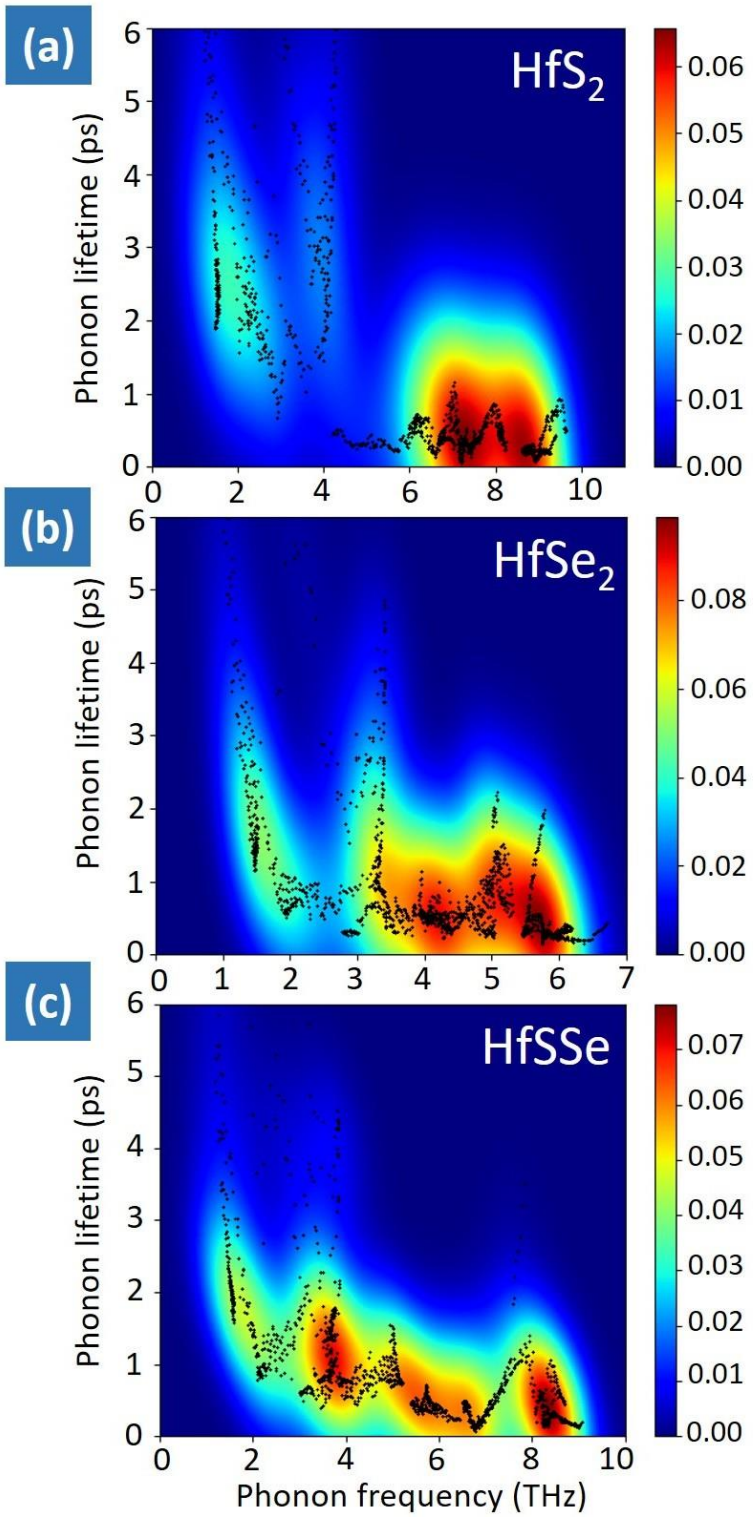

Figure 4.2. 7 Distribution of phonon lifetimes as a function of phonon frequency at temperature 300 K for the monolayer HfS_2, $HfSe_2$, and Janus HfSSe, calculated with the use of Seaborn Python visualization library tool. Phonon lifetime is measured in picoseconds (ps) and phonon frequency is calculated in terahertz (THz). The black dots reflect the original phonon modes on the coloured background profile. Regions with a high density of phonon modes in the frequency-lifetime plot are calculated by using Gaussian-KDE (kernel density estimation) which is represented by red color.

4.2.3.8 Mode Grüneisen parameter with NAC term

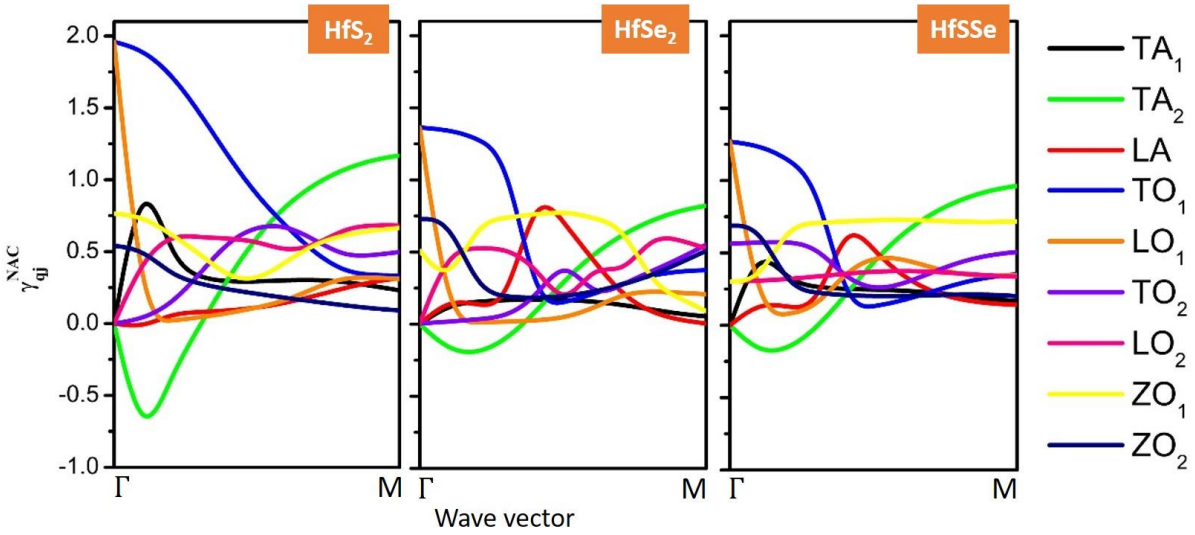

Figure 4.2. 8 Non-analytical term corrected mode Grüneisen parameter, (γ_{qj}^{NAC}) which is derived from third-order force constants for (a) HfS_2 (b) $HfSe_2$ and (c) HfSSe monolayers. Different coloured curves represent different phonon modes.

The Grüneisen parameter, γ_{qj} which describes the thermal expansion of a crystal also provides anharmonicity in crystal potential. Understanding the phonon dynamics, corresponding phonon anharmonicity, and its relationship with a low k_L is critical for the development of better thermoelectric materials. Systems with intrinsically strong anharmonicity in their lattice vibrations assist to decouple phonon and electronic transport behaviour of solids. In Figure 4.2.8, the non-analytically term corrected mode Grüneisen parameter (γ_{qj}^{NAC}) for acoustic and optical modes of monolayer HfS_2, $HfSe_2$ and HfSSe reflect the mode-dependent strength of anharmonicity (See Appendix II for numerical details). A large Grüneisen parameter is an indicator of strong anharmonic phonon vibrations. As depicted in the phonon dispersion in Figure 4.2.6(d), the lowest TO-mode exhibits an apparent drop into the acoustic phonon regime around the BZ centre (near Γ point) that results in the flattening of the TO-mode around the Γ point in the BZ. This leads to an abrupt change in calculated γ_{TA} due to avoided crossing between TA and low-lying optic phonons. In comparison, LA mode is better able to retain its dispersion around the BZ boundary without undergoing a drastic softening. Accordingly, the calculated γ_{LA} curve exhibits some small bumps when LA crosses the low-lying optic phonon with slight fluctuation in its slope. In Figure 4.2.5(a), the transverse optical (TO) phonon mode is found to be well dispersed round the Γ-point. In HfS_2, the TO mode is found to be dispersed over more than 50 cm^{-1} along the Γ-M pathway. Likewise, Figure 4.2.8 shows the Grüneisen parameter for the TO1 mode on HfS_2 to be dispersed over more than 1.5 unit along the Γ-M pathway. In Figure 4.2.5, LO-TO splitting is found be larger on HfS_2 than on $HfSe_2$.

Correspondingly, a larger dispersion in the phonon modes is noticed in Figure 4.2.8 on HfS_2. This high sensitivity of the TO mode at Γ-point to the volume change indicate a large coupling between the TO modes and longitudinal acoustic LA modes where the intrinsic scattering of LA modes would facilitate in lowering the k_L. Thus one could expect that a strong coupling between low lying optical phonons and TA/LA phonons should play an important role in determining the thermal conduction in these solids.

4.2.4 Conclusion

A systematic investigation on ultralow k_L in monolayer HfS_2, $HfSe_2$ and their Janus derivative HfSSe have been carried out *via* second-order harmonic and third-order anharmonic interatomic force-constants. Domination of ionic character in the interatomic bonding together with the high Born-effective/dynamical charges bring about a substantially high phonon-electric field coupling, which in turn, induces a large longitudinal optic-transverse optic (i.e. LO-TO) splitting around the Γ-point in these monolayers crystals. This incorporation of NAC term imparts a striking difference in the lattice thermal conductivities, k_L , as it is fairly high in such systems. A small magnitude of phonon lifetimes in combination with a low phonon group velocity causes an ultralow k_L in these monolayers. The calculated mode Grüneisen parameter is found to be as high as ~ 2.0 at $300\ K$, which is fairly large for a 2D material, indicating strong anharmonicity in lattice vibrations. It is favourable for enhancing phonon scattering and in turn, lowing its thermal conductivity. Our calculations unveil the importance of the considering of phonon-electric field coupling in ionic (polar) materials while designing thermoelectric systems, particularly, *via* impacting the magnitude of k_L.

Chapter 5

Artificial Photosynthesis in Single Layer MoS_2

Based on the work published in:

Dimple, Nityasagar Jena, Ashima Rawat, and Abir De Sarkar, "Strain and pH facilitated artificial photosynthesis in monolayer MoS_2 nanosheet", ***J. Mater. Chem. A*** 2017, 5, 22265-22276

5.1 Introduction

MoS_2 has been extensively studied as a promising electro-catalyst for H_2 evolution due to its high HER (Hydrogen evolution reaction) activity and can be regarded as a promising alternative to Pt due to its high abundance and low cost [256–261]. Using μ-Raman spectroscopy, under water stability of single layer MoS_2 has also been verified [262]. Xiao el al. has demonstrated the high efficiency of crystallinity controllable monolayer (ML) MoS_2 for solar hydrogen production [263]. Doping of MoS_2 with different types of dopants has also been investigated [264–266]. On the basis of experimental investigation, Liu et al. reported flower-like N-doped MoS_2 for water pollution treatment [265]. Li et al. have explored the potential of phosphorus based p-type dopant in water-splitting. MoS_2 based hetero-structures has also been widely investigated [267–270] in this regard. Wang et al. [271] predicted that type-II band alignment in hybrid g-C_3N_4/MoS_2 nanocomposite may enhance photo-catalytic activity. Recently, Abbasi et al. [272] achieved lowest onset potential for CO_2 reduction by Nb-doped vertically aligned MoS_2. Asadi et al. [273] have unveiled that layer-stacked bulk MoS_2 shows superior carbon dioxide reduction performance relative to the noble metals such as Au and Ag in terms of a high current density and low over potential (54 mV) in an ionic liquid. A few more strategies consisting in nanostructural engineering, such as alloying [274,275] and doping [266,276], have also been adopted to improve the photocatalytic water splitting by tuning the band edges. Notwithstanding the ease of applying mechanical strain reversibly, strain effects have been relatively sparsely explored.

Strain arises naturally in heterostructures and core-shell structures due to lattice mismatch at the interfaces. However, strain effects are usually masked by other effects. The influence of strain on the electrocatalytic activity, e.g., the hydrogen evolution reaction (HER) in Pt, Cu and Ni films, has been reported, where the effect of strain has been isolated from other factors [277]. In this combined experimental and theoretical study [277] elastic strain has been demonstrated to play a crucial role in controlling HER. Strain effects on the photocatalytic activities have been relatively scarcely studied experimentally. For instance, modulation in photocatalytic properties *via* strain in 2D BiOBr nanosheets have been studied [278]. In an experimental study, enhancement in photocatalytic HER in MoS_2 nanosheet has been attributed to increased specific surface area or tensile strain induced by the lattice mismatch at the MoS_2/TiO_2 interface [279]. Despite a limited number of studies on the role of strain in catalytic reactions [278,280–283], an in-depth investigation of the same on photocatalysis in 2D materials which adequately addresses the interplay of all the controlling factors is conspicuously missing. Moreover, in ab initio studies, photocatalytic activities have mainly been assessed in terms of band gap

engineering or alignment of the band edges of the photocatalytic material with the redox potential for water splitting and CO_2 reduction,[266,275,284–286] which have undoubtedly advanced our scientific understanding. However, the efficiency in photocatalytic activity is governed by the collective operation of a multitude of factors such as suitable band edges straddling the redox potentials, high optical absorbance and conductivity, small exciton binding energies, high carrier mobility, large carrier mobilities ratio for prolonging carrier lifetimes or lowering carrier recombination rates. The interconnections between all these factors and their variation with strain of all kinds have been comprehensively studied in this chapter using density functional theory to calibrate the photocatalytic response and in turn, ascertain the magnitude and type of strain under which the artificial photosynthetic activity of single layer MoS_2 is optimally enhanced. Besides a detailed study on strain effects, the role of pH has been carefully addressed to find the appropriate pH for optimum solar energy harvesting in the photoconversion of CO_2 with H_2O. To the best of our knowledge, this was the first study on artificial photosynthesis in single layer MoS_2. Our insightful findings are understood to motivate experimental work on strain controllable photocatalytic activity.

5.2 Computational Details

First-Principles calculations have been carried out using Vienna Ab-initio Simulation Package (VASP) [149,150,211,212], which is based on density functional theory (DFT). Electronic structure calculations have been performed using the generalized gradient approximation (GGA)[106] variant of the Perdew–Burke–Ernzerhof (PBE) functional. A cut off energy of 500 eV for the plane wave basis set has been used throughout all the calculations. Both atomic positions and lattice constants were fully relaxed using conjugate gradient method. Atomic relaxations have been performed until the Hellman–Feynman forces on each atom reached less than 1 meV/Å. The total energy convergence criterion between successive self-consistent cycles was set at 1×10^{-5} eV. A $16x9x1$ and $9\times9\times1$ Γ-centred k-mesh have been sampled respectively for the supercells in orthorhombic and hexagonal symmetry to optimize the geometry of ML-MoS_2. A vacuum thickness of more than 14 Å along the z direction was adopted to reduce the spurious interactions between the periodic images to a negligible level. For all the strained systems, only the ionic relaxations have been carried out, while the scaled lattice constants have been held fixed, as routinely pursued in earlier works [87,179,287]. Shear strain of type-I corresponds to the application of tensile strain and compressive strain of the same magnitude along the zigzag (zz) and armchair (ac) directions respectively, while shear strain of type II is the other way round.

G_0W_0 or the quasiparticle (QP) approximation [36] is known to compute the band gap and band

edges more accurately and reliably as compared to the routinely used DFT functionals. Therefore, to get around the computationally demanding and time consuming QP calculations, the following assumptions have been reasonably made to combine the speed of GGA-PBE with the accuracy of QP.

1. Electronic band structure for both strain-free and strained ML-MoS_2 has been calculated by using GGA+PBE XC functional and the energy of the band edges obtained from G_0W_0 approximation[36] in an earlier study has been used as a valuable input in the current study.

2. Band structure for all the strained geometries have been calculated by using GGA-PBE as XC functional.

3. GGA-PBE is good at predicting trends, e.g., the variation in band edges, band gap, absorbance peaks, etc with strain. Therefore, the strain induced shift in the band edges calculated using GGA-PBE has been added to the band edges of the pristine and unstrained MoS_2 single layer obtained from G_0W_0 or quasi particle (QP) approximation [36] corresponding to the different levels and types of strain.

Optical properties of ML-MoS2 have been determined by the frequency dependent complex dielectric function, $\varepsilon(\omega) = \varepsilon_1(\omega) + i\varepsilon_2(\omega)$, which represents a linear response of the system to an external electromagnetic field. The dielectric function $\varepsilon(\omega)$ consists of two contributions: a Drude-like intraband contribution and an interband contribution. The imaginary part of the interband contribution involves the interband matrix elements of the momentum operators, and can be evaluated directly in DFT.[288]

$$\varepsilon_2(\omega) = \varepsilon_{\alpha\beta}^{(2)}(\omega) = \frac{4\pi^2 e^2}{\Omega} \lim_{q\to 0} \frac{1}{q^2} \sum_{c,v,k} 2w_k \delta(\epsilon_{ck} - \epsilon_{vk-}\omega) \times \langle u_{ck+e\alpha q} | u_{vk} \rangle \langle u_{ck+e\beta q} | u_{vk} \rangle^*$$

where the indices c and v refer to the conduction and valence band states respectively and u_{ck} is the cell periodic part of the orbitals at the k-point.

Its real part can then be calculated using Kramers-Kronig transformation.

$$\varepsilon_1(\omega) = \varepsilon_{\alpha\beta}^{(1)}(\omega) = 1 + \frac{2}{\pi} P \int_0^\infty \frac{\varepsilon_{\alpha\beta}^{(2)}(\omega')\omega'}{\omega'^2 - \omega^2 + i\eta} d\omega'$$

Where *P* denotes the principle value and a small complex shift (η) of 0.1 has been used for slight smoothening of the real part of the dielectric function, which is routinely used in most of the calculations.

Several optical parameters such as Absorbance, Reflectivity, EELS (electron energy loss spectra) function, Extinction function and optical conductivity etc can be derived from $\varepsilon_1(\omega)$ and $\varepsilon_2(\omega)$. Optical properties of ML-MoS_2 are calculated from the complex dielectric function. The absorption coefficient ($\alpha_{abs.}$) is given by

$$\alpha_{abs} = \sqrt{2}\omega\left(\sqrt{\varepsilon_1^2(\omega) + \varepsilon_2^2(\omega)} - \varepsilon_1(\varepsilon)\right)^{1/2},$$

where $\varepsilon_1(\omega)$ and $\varepsilon_2(\omega)$ are the real and imaginary parts, respectively of the frequency dependent dielectric function, $\varepsilon(\omega)$. By taking the tensor nature of $\varepsilon(\omega)$ into account, $\varepsilon_1(\omega)$ and $\varepsilon_2(\omega)$ have been averaged over the three polarization vectors (along x, y, and z directions).

5.3 Results and discussion

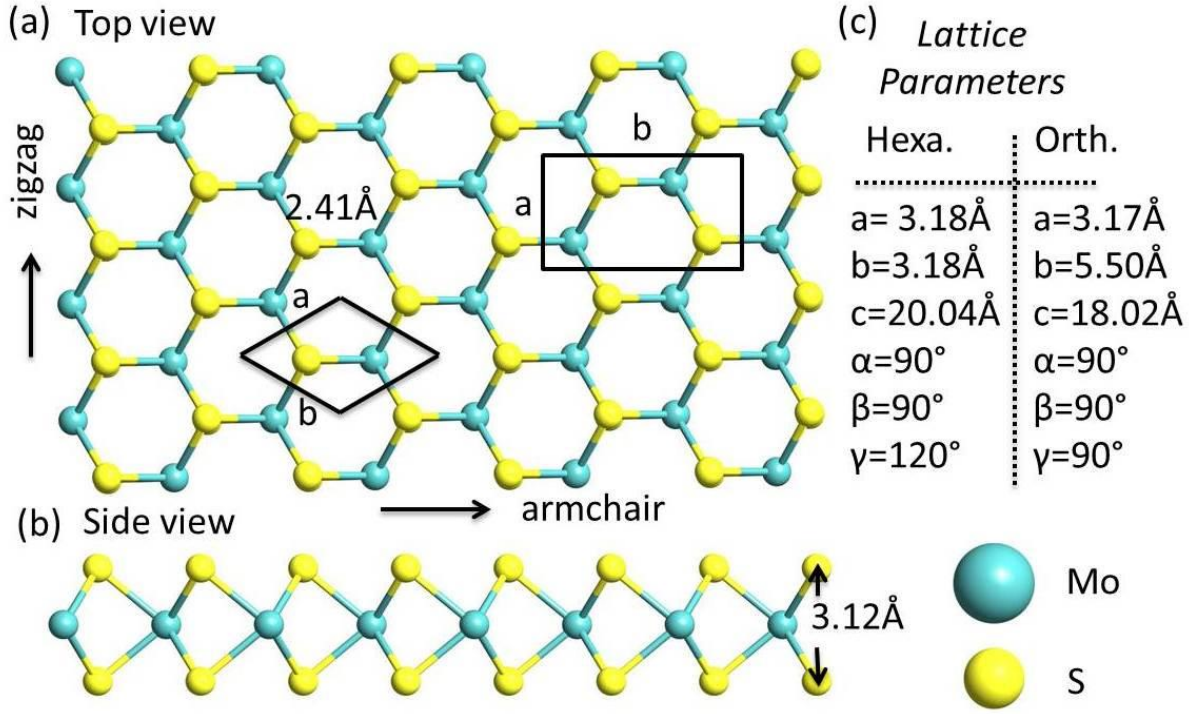

Figure 5. 1 (a) Ball and stick model of optimized geometry of single layer MoS_2 in supercells with hexagonal and orthorhombic symmetry [Top view], (b) side view of layered structure and (c) optimized geometry parameters for orthorhombic and hexagonal supercell

Naturally occurring MoS_2 can be found in two major polytypes: 2H and 3R phase. Out of these two, 2H phase having D_{6h} point group symmetry is more abundant. 2H-phase can be converted into 1H-phase with D_{3h} point group by exfoliating it from its bulk. In 1H-MoS_2, each Mo (IV) centre occupies a trigonal prismatic coordination sphere that binds to six sulphide ligands and each sulphur centre is pyramidal and is connected to three Mo atoms forming the trigonal prismatic layered structure. ML-MoS_2 nanosheet is highly flexible and its electronic properties can be extensively tuned *via* the application of strain. To realize the application of mechanical

strain, we initialized the atomic positions in the 2D MoS_2 nanosheet in a hexagonal honeycomb lattice with two different symmetries, namely, hexagonal and orthorhombic (rectangular in plane), as shown in Figure 5.1 (a), for a systematic investigation. The lattice constants in the hexagonal supercell along the two equivalent lattice directions, namely, the zz direction, are equal (a=b), whereas the orthorhombic supercell has a rectangular symmetry and shows two non-equivalent directions, namely, zz and ac directions along its x and y axes respectively. The optimized lattice constants for both supercells are shown in Figure 5.1 (c), which is in agreement with earlier findings [29,249,255,289–295]. The Mo-S bond length is found to be 2.41 Å and vertical S-S distance is 3.12 Å, which is consistent with the previous reports [29,249,255,289–295].

5.3.1 Optical properties

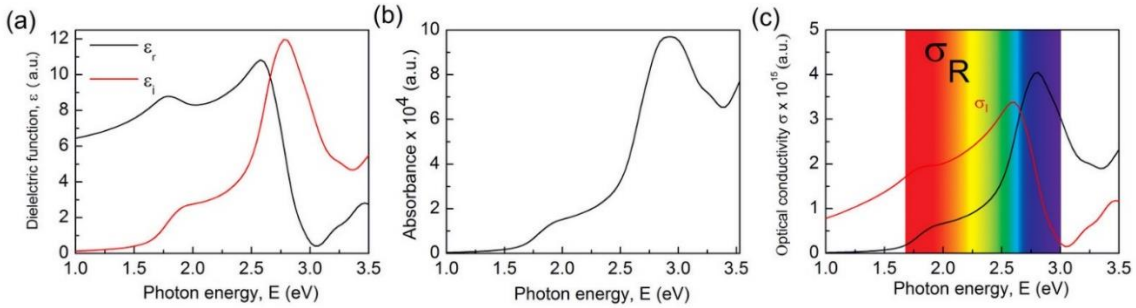

Figure 5. 2 (a) Real $\varepsilon_1(\omega)$ and imaginary $\varepsilon_2(\omega)$ part of the frequency dependent dielectric function (b) Absorption spectra, $\alpha_{abs.}$, (c) Real, $\sigma_r(\omega)$ and imaginary, $\sigma_i(\omega)$ part of optical conductivity in pristine unstrained single layer MoS_2

Photo-catalytic properties of inorganic semiconducting materials are significantly controlled by their optical response. Therefore, the fundamental optical properties such as frequency dependent dielectric function and absorbance spectra of strain-free pristine ML-MoS_2 nanosheet have been calculated first, which is shown in Figure 5.2 (a)-(b). In pristineML-MoS_2 nanosheet, the prominent absorption peak in the absorbance spectra occurs at 2.7 eV with its low excitonic peaks at around 1.8 to 2.1 eV. The low energy excitonic peaks are not well resolved under the independent particle approximation as it does not take into account the local field and the excitonic effects. However, this approximation has been found to be good enough to predict trends in the perturbative response of the optical properties, e.g., under the application of electric field or strain [296,297]. The absorbance along the zz direction reaches its maximum at 3% uniaxial tensile strain applied along the zz direction; however, corresponding to uniaxial tensile strain applied along the ac direction, maximum value is attained along the ac direction at the same percentage of strain. For biaxial tensile strain, the absorbance peaks up at 1% along both the zz and ac directions.

The redshift in the absorbance peaks with the application of tensile strain of both kinds, uniaxial and biaxial, agrees with the trends in PL observed experimentally [296,297]. For shear strain of type I, the maximum in absorbance is attained along the zz direction at 3% strain; however, the maximum switches to the ac direction for shear strain of type-II (see Figure 5.3) corresponding to the same strain %.

Furthermore, optical conductivity in pristine, strain free ML-MoS_2 nanosheet have been calculated using the relation $\sigma_1(\omega) = \frac{\omega\varepsilon_2(\omega)}{4\pi}$ and $\sigma_2(\omega) = \frac{\omega\varepsilon_1(\omega)}{4\pi}$, where $\sigma_1(\omega)$ and $\sigma_2(\omega)$ are real and imaginary part of the optical conductivity and $\boldsymbol{\omega}$ is the frequency of the incident photon as shown in Figure 5.2 (c). Calculated optical conductivity correctly reproduces all main features measured experimentally [298] and calculated theoretically [299] based on the

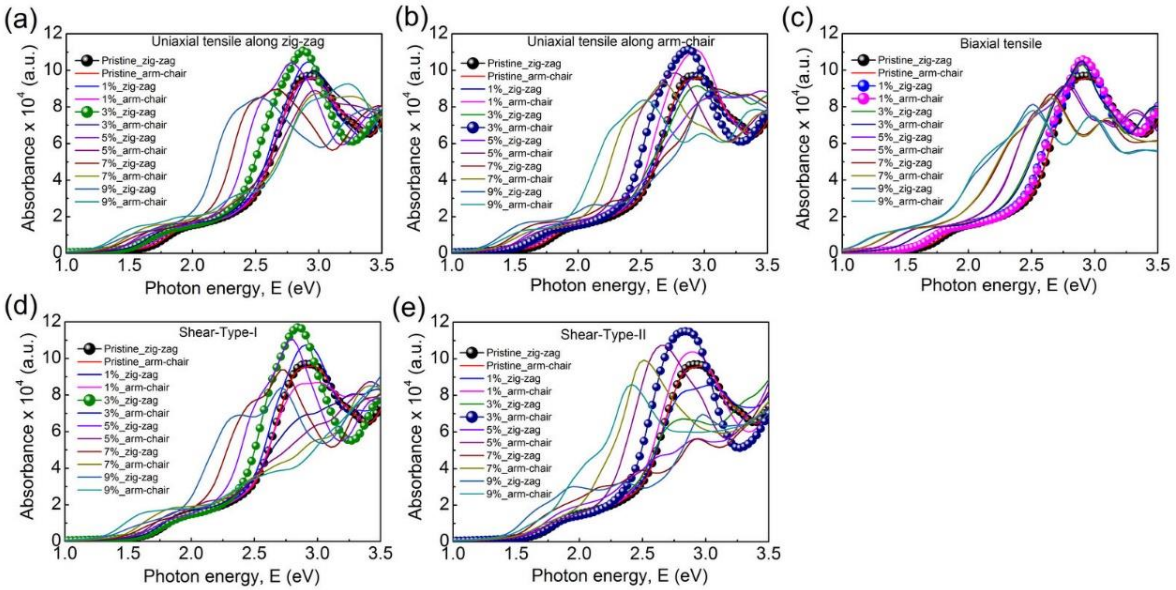

Figure 5. 3 Variation in the absorbance spectra with different kinds of applied mechanical strain

empirical Sellmeier equation between refractive index and incident photon energy. A sharp rise or a peak at $\hbar\omega = 2.7eV$, shown in Figure 5.1 (c), has been observed on account of the interband transition. The real and imaginary part of the optical conductivity, $\sigma_1(\omega)$ and $\sigma_2(\omega)$ signifies the dissipation of electromagnetic energy and the screening of the applied field respectively. The peak in $\sigma_1(\omega)$ attains its maximum value along the zz direction at 3% of uniaxial tensile strain applied along the zz direction. For uniaxial tensile strain applied along the ac direction, $\sigma_1(\omega)$ shows peak up at 1% of strain along the ac direction. For biaxial tensile strain, $\sigma_1(\omega)$ reaches its maximum along zz direction at 1% strain. Upon the application of shear strain of type-I, the peak in $\sigma_1(\omega)$ is found to reach its maximum at 3% strain along the zz direction, whereas for shear type-II, maximum is attained along the ac direction, as shown in Figure 5.4. Shear strain is found to be more effective as compared to the tensile and biaxial

strain in enhancing the magnitude of $\sigma_1(\omega)$ significantly.

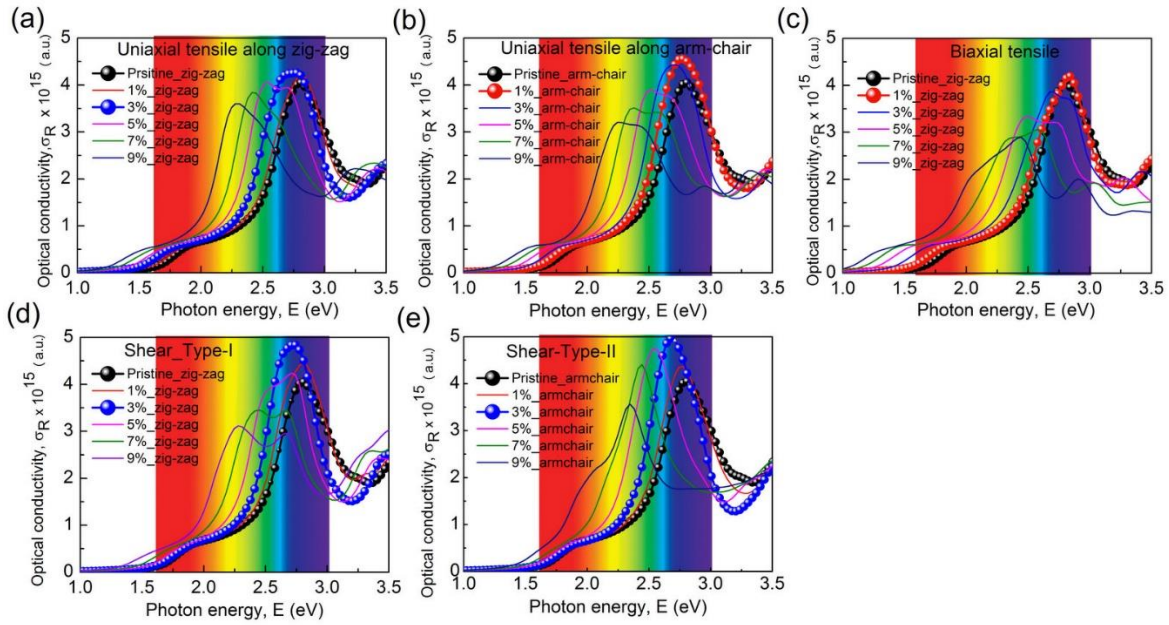

Figure 5. 4 Variation in optical conductivity with various types of mechanical strain. The vertical color bars correspond to different regions in the visible light spectrum. The optimum value of strain where the optical conductivity maximizes is highlighted in the figure.

5.3.2 Exciton binding energy

Furthermore, exciton binding energies under different types and magnitude of strain have been investigated. Small exciton binding energies are desirable to facilitate the splitting of excitons into free charge carriers (electrons and holes). Mott-Wannier exciton hydrogenic model has been considered to calculate the excitonic binding energy using the formula: $E_B^{exciton} = \frac{4\times13.6\,\mu_{ex}}{m_0\varepsilon^2}\,(eV)$, where m_0 is the the electron rest mass, $\mu_{ex}^{-1} = m_e^{-1} + m_h^{-1}$ is the excitonic effective mass and $\boldsymbol{\varepsilon}$ is the macroscopic static dielectric constant. The calculated value of excitonic binding energy for ML-MoS_2 is 0.41eV which is in good agreement with the previous reports [300,301]. It is very important to note the variation in exciton binding energy with applied mechanical strain. High excitonic binding energies hinder electron-hole separation. In Figure 5.5, the variation in excitonic binding energy with uniaxial strain (well agreed with theoretical results [302,303]). The excitonic binding energy reaches 0.65 eV at 1% uniaxial tensile strain applied along the zz and ac directions while it decreases from 0.65 eV to 0.41eV when uniaxial tensile strain is varied from 2 to 9%. At 5% of uniaxial compression, it reaches its highest value of 0.91eV. The exciton binding energy decrease for uniaxial compression higher than 5% and reaches 0.7eV at 9%. Under the application of biaxial tensile strain, its value reaches its maximum, 0.65eV at 1% strain and declines for strain greater than 1%. It reaches 0.29eV at 9% strain, as shown in Figure 5.6. Its value also increases with biaxial

compression and reaches its maximum, 0.68eV at 4% of biaxial compression and then decreases and reaches 0.35 eV at 9%. However, a sharp drop in excitonic binding energy along the zz direction, from 0.41eV to 0.27eV, is found to occur at 8% shear strain of type-II, as shown in Figure 5.5.

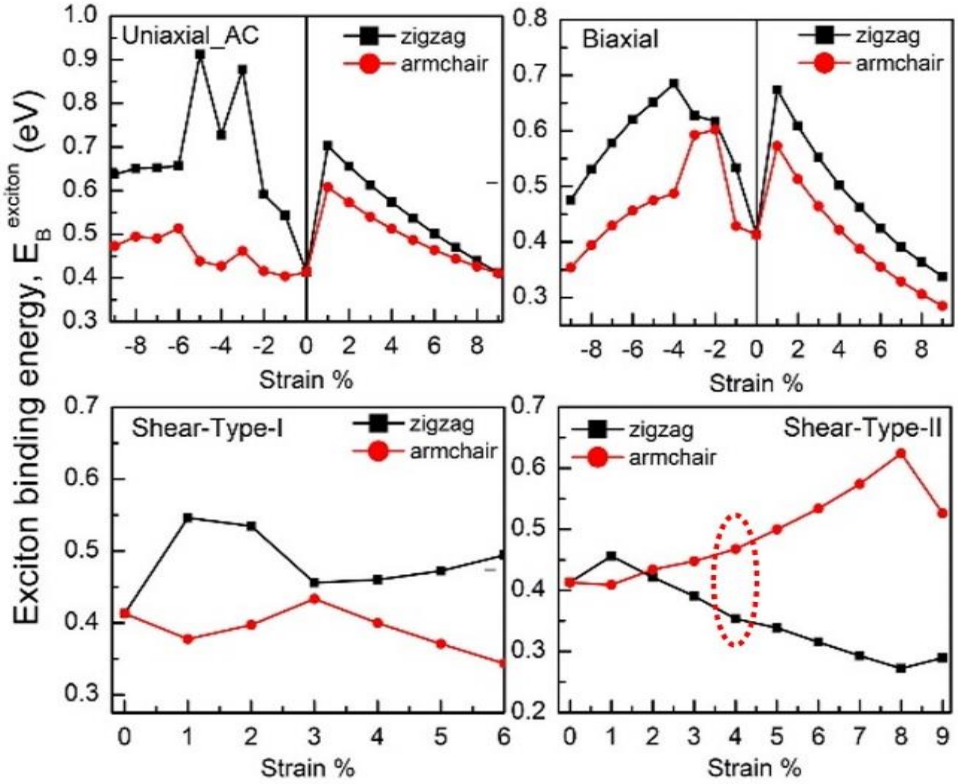

Figure 5. 5 Variation in excitonic binding energies with strain applied on to the ML-MoS_2 nanosheet. (Shear strain of type-I corresponds to the application of tensile strain and compressive strain of the same magnitude along the zigzag and armchair directions respectively. While shear strain of type-II is the other way round: application of tensile and compressive strain of equal magnitude along the armchair and zigzag directions respectively.) The exciton binding energies are small at 3-4% strain, when the optical absorbance/conductivity reaches its maximum

5.3.3 Electronic properties: band edges relative to redox potentials

For an inorganic semiconductor to function as an efficient photo-catalyst, proper alignment of the energy levels with respect to the redox level is a must. A photocatalytic material needs to be semi-conductor with a minimum band-gap (E_g) of 1.23eV in order to be able to absorb incident photons having energy $E=h\nu \geq 1.23$eV, i.e. a wavelength $\lambda \leq 1010$nm at standard conditions (T=298 K, P=1 bar and pH=0). However, thermo-dynamical losses have to be realistically taken into account, implying that the minimum band gap needs to be at least 1.5eV that allows absorption of a large portion of the solar spectrum. Also, the photo-catalyst must have suitable band edges to straddle the redox potential of water to drive the kinetics of the

half-cell reactions, hydrogen evolution (reduction) and oxygen evolution (oxidation) reactions. On the absolute vacuum scale, at pH=0, this minimum band gap value of 1.23 eV corresponds to the situation where the CBE would ideally lie at -4.44eV, the reduction potential (RP) for hydrogen evolution reaction (H^+/H_2) and the VBE would remain at -5.67 eV, the oxidation potential (OP) for oxygen evolution reaction (H_2O/O_2). If CBE and VBE energy levels are positive and negative relative to the reduction and oxidation potentials, the water splitting reaction will be favoured. Likewise, CO_2 reduction with water is thermodynamically favourable when the band edges straddle the reduction potentials of CO_2 and the oxidation potential of H_2O. The minimum band gap required for CO_2 reduction is 1.43 eV, which is 0.2 eV higher than the one needed for water splitting. This is due to the fact that the highest reduction potential for CO_2 which corresponds to the reduction of CO_2 reduction to HCOOH lies at -4.24 eV.

The magnitude of the band gap in ML-MoS_2 is larger than 1.23 eV and its band edges do straddle the reduction potentials for hydrogen evolution reaction (H^+/H_2) or CO_2 reduction reaction (CO_2/HCOOH), and oxidation potential for oxygen evolution reaction (H_2O/O_2).

As the CBE in ML-MoS_2 lies above the CO_2 reduction level and thereby CO_2 reduction is also thermodynamically favorable, in presence of CO_2. Therefore, it turns out that ML-MoS_2 is suitable not only for H_2O reduction but also for CO_2 reduction. For water splitting to occur, which leads to the evolution of H_2 and O_2, the following criteria is required to be satisfied at pH = 7.[304]

$$\boldsymbol{E_{VBM} < E^0_{ox,H_2O/O_2} = +0.82\ V}$$

$$\boldsymbol{E_{CBM} > E^0_{red,H^+/H_2} = -0.41\ V}$$

Whereas for CO_2 reduction to HCOOH, HCHO, CH_3OH, or CH_4, at pH = 7, the criteria changes to the following.

$$\boldsymbol{E_{CBM} > E^0_{red,CO_2/HCOOH} = -0.61\ V}$$

$$\boldsymbol{E_{CBM} > E^0_{red,CO_2/HCHO} = -0.48\ V}$$

$$\boldsymbol{E_{CBM} > E^0_{red,CO_2/CH_3OH} = -0.38\ V}$$

$$\boldsymbol{E_{CBM} > E^0_{red,CO_2/CH_4} = -0.24\ V}$$

Here $\boldsymbol{E^0}$ represents the standard reduction potentials for different species.

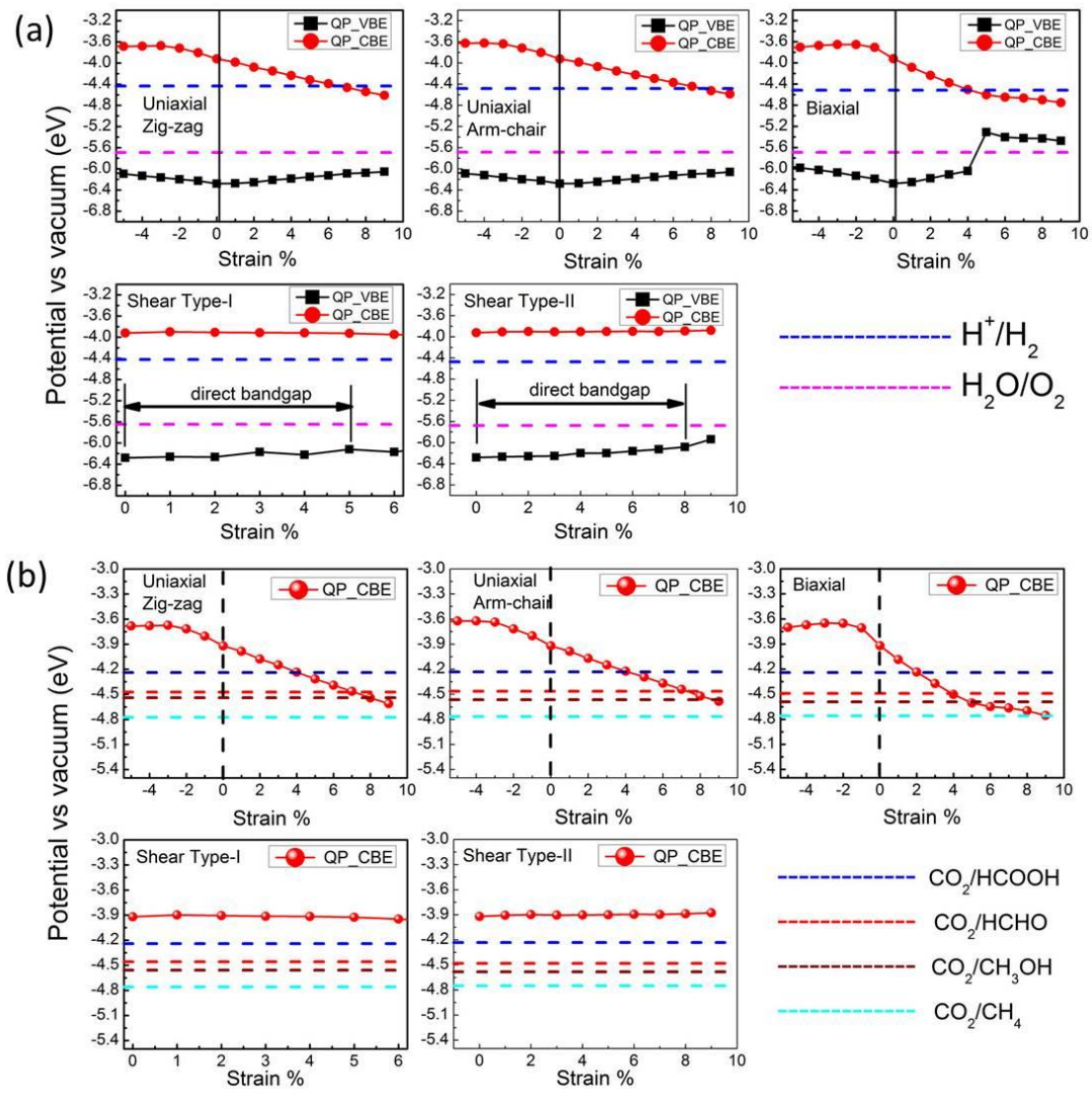

Figure 5. 6 Variation in the valence and conduction band edges with the application of different kinds of mechanical strain for (a) solar water splitting and (b) light driven CO_2 reduction with H_2O. QP_CBE is an acronym for G_oW_o quasiparticle (QP) approximation and conduction band edge

As electronic properties in ML-MoS_2 are very sensitive to the applied mechanical strain, the variation in the alignment of the band edges with respect to reduction potentials of both H_2O and CO_2 and oxidation potential of H_2O has been plotted as a function of strain in Figure 5.6. Figure 5.6 (a) depicts that CBE drops gradually towards the reduction potential with the application of uniaxial and biaxial tensile strain; however, VBE progressively rises towards the oxidation potential. 6% and 7% are found to be the optimum magnitudes of uniaxial tensile strain applied along the zz and ac directions; corresponding to which the band edges reach closest to the redox potentials. For biaxial tensile strain, it occurs at 4% when both oxygen evolution and hydrogen evolution reactions, are optimally favoured. Moreover, the optical conductivity and absorbance reach their maximum at 3% and 1% uniaxial tensile strain along

zig-zag and arm-chair directions respectively, and 1% biaxial tensile strain. These results on tensile strain is consistent with the experimentally observed enhancement in photocatalytic HER in MoS_2 nanosheet induced by increased specific surface area or tensile strain induced by the lattice mismatch at the MoS_2/TiO_2 interface[279]. Shear strain is found to be particularly interesting. The band edge positions undergo minimal changes under the application of shear strain of both types, whereas the other properties such as carrier mobility vary significantly with the application of shear strain. With the application of shear strain of both types, the CBE and VBE are found to shift slightly towards the reduction potential and oxidation potential respectively.

For CO_2 reduction with H_2O, the reduction potential is not a single one or unique. The several reduction potentials of CO_2 correspond to the different degrees in the reduction of CO_2. Production of different solar fuels or precursors such as HCOOH, HCHO, CH_3OH, CO and CH_4 is determined by the extent to which the oxidation state in C is lowered. As CBE in ML-MoS_2 nanosheet lies above all these reduction potentials, it may be considered as a suitable candidate for CO_2 reduction as well. Furthermore, as shown in Figure 5.6 (b), 3% of the uniaxial tensile strain along its zz as well as ac direction is the optimum strain percentage. For biaxial tensile strain the optimum value is 1% of strain. For shear strain cases, band edges hardly shift with the application of strain.

5.3.4 Suitability of pH for solar fuel production

Efficiency of photo-catalytic reactions is crucially determined by the pH value[286,305]. Water redox potential can be adjusted to a suitable level to drive the overall water-splitting reactions on a single-layer MoS_2 photo-catalyst. Many metal complexes such as Mn, Fe, Co etc.[306] are known to catalyze CO_2 reduction and some of them show high selectivity. Selectivity over an inorganic semiconductor can be controlled by changing acidity/basicity. Furthermore, differences in the potential for reduction of CO_2 to different fuels, such as HCOOH, HCHO, CH_3OH, CH_4, depending on the degree of CO_2 reduction, provides an opportunity to carefully tune the selectivity in the generation of these renewable solar fuels, as shown in Figure 5.7 (b). The reduction potential of all the fuel precursors can be adjusted to suitable pH for CO_2 reduction. Experimental values of redox potential for all redox level at pH =7[307] have been used in this study. Specifically, the electrochemical potential of the oxidation and reduction reactions can be calculated using the Nernst equation[308] at all pH ranges from 0-14.

$$E^{Ox}_{O_2/H_2O} = -4.44 + (-1)(+1.229) + pH \times 0.0529eV - \frac{0.0592}{4} log_{10}(pO_2)$$

$$E^{Ox}_{H^+/H_2} = -4.44 + (-1)(+0.401) - pOH \times 0.0529eV - \frac{0.0592}{4} log_{10}(pO_2)$$

where pO_2 denotes the partial pressure of oxygen in ambient conditions, -4.44 eV corresponds to the NHE potential, and pOH + pH=14. From Figure 5.7 (a) it can be directly observed that pH between 0.5-6.5 seems to be the favorable condition for water splitting reaction whereas for CO_2 reduction with H_2O, the suitable pH range is 0.5-3, as shown by Figure 5.7 (b).

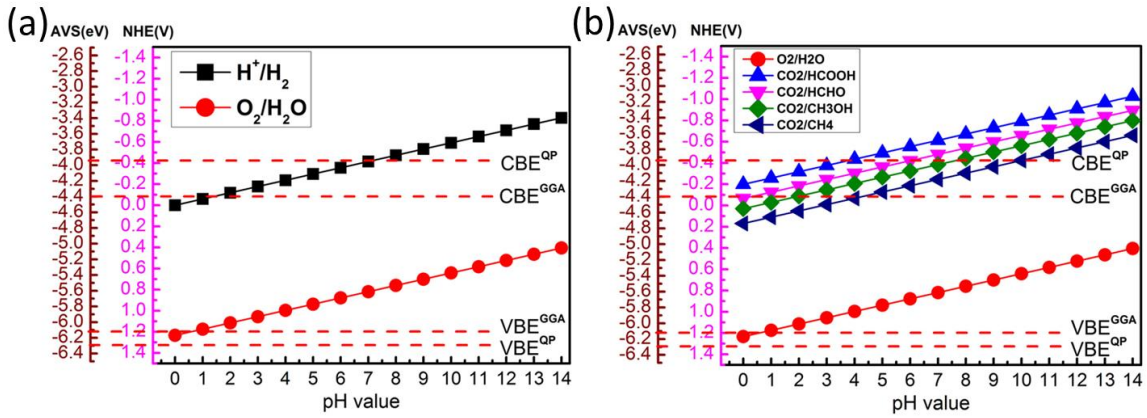

Figure 5. 7 Effect of pH value on the redox potential level for (a) H_2O splitting and (b) CO_2 reduction with respect to the absolute vacuum scale and normal hydrogen electrode. QP is an acronym for G_0W_0 quasiparticle (QP) approximation, while AVS & NHE denote absolute vacuum scale and normal hydrogen electrode respectively

5.3.5 Carrier Mobility

The photocatalytic activity strongly depends on the charge carrier separation, carrier lifetimes or carrier recombination rates. To study the separation and migration of electron-hole pairs, the charge carrier mobility in pristine ML-MoS_2 nanosheet and its variation with the applied mechanical strain has been studied. Correlation between the electron–hole recombination rate and the degree of lattice strain has also experimentally verified with silicon NWs and strain-tuned carrier decay lifetime in InGaN/GaN SQW [309,310]. Room temperature carrier mobility is calculated by using longitudinal acoustic phonon-limited scattering model which was actually based on deformation potential approximation formulated by Bardeen and Schokley [176]-[177]. In 2D inorganic semiconductors, at room temperature, the coherent wavelength of thermally agitated carriers is much larger than their lattice constants and is close to acoustic phonon modes at the zone centre of the BZ where coupling between electron and acoustic phonons dominates over the carrier scattering in the low energy regime. Therefore, in this limit, carrier mobility can be effectively derived from effective mass and deformation potential approximation. This formulation has recently been significantly refined by Lang et al.[177] In

this formulation, mobility along one direction depends not only on the parameters (effective mass, deformation potential constant, and elastic modulus) in the same direction, but also on those along the perpendicular direction. The carrier mobility ratio has been shown to arise mainly from the anisotropic effective mass, while the contribution from the deformation potential constant and the elastic modulus are relatively insignificant. It has also been used recently to study on SnSe[217]. MoS_2 has not been studied in that study possibly due to its isotropic nature in the pristine structure in terms of all these parameters, such as effective mass and elastic modulus. Nevertheless, the application of mechanical strain induces anisotropy in ML-MoS_2 and therefore, this approach is substantially more accurate in calculating the carrier mobility and its anisotropy under strain. The original formulation of the deformation potential theory of Bardeen and Shockley, which has been widely adopted has been demonstrated to be relatively much less reliable and more likely to overestimate the carrier mobility and the carrier mobility ratio, relative to this new formulation, in a large number of case studies[177]. The carrier mobility in the new formulation is given as

$$\mu_{\alpha x} \approx \frac{e\hbar^3 \left(\frac{5C_{x_{2D}} + 3C_{y_{2D}}}{8}\right)}{k_B T (m_{\alpha x})^{\frac{3}{2}} (m_{\alpha y})^{\frac{1}{2}} \left(\frac{9E_{\alpha x}^2 + 7E_{\alpha x}E_{\alpha y} + 4E_{\alpha y}^2}{20}\right)} x10^4 \; cm^2 V^{-1} s^{-1}$$

Where $\alpha = e, h$ denotes the type of carriers (electrons or holes), effective mass of carriers α in the units of rest mass of electron m_0 along the $\boldsymbol{x}$ and $\boldsymbol{y}$ directions are designated by $m_{\alpha x}$ and $m_{\alpha y}$ respectively and calculated by using the relation: $m_\alpha = \hbar^2[\partial^2 E(k)/\partial k^2]^{-1}$, deformation potential of the carriers along the x and y directions are denoted by $E_{\alpha x}$ and $E_{\alpha y}$ respectively and 2D elastic stiffness coefficients along the $\boldsymbol{x}$ and $\boldsymbol{y}$ directions are designated by $C_{x_{2D}}$ and $C_{y_{2D}}$ respectively. All the mobility calculations have been carried out at 300K. The other component $\mu_{\alpha y}$ of mobility can be easily calculated by simply interchanging x and y in the above mobility relation. The calculated parameters for the pristine ML-MoS_2 are tabulated in Table 5.1.

Table 5. 1 Effective mass (m_α), elastic stiffness coefficient (C_{2D}), deformation potential ($E_{direction\_2D}$) and charge carrier mobility (μ) along zigzag (zz) and armchair (ac) direction in pristine ML-MoS_2 nanosheet

Carrier type	m_{α_zz}/m_0	m_{α_ac}/m_0	$C_{zz\_2_D}$ (N/m)	$C_{ac\_2_D}$(N/m)	$E_{zz\_2_D}$ (eV)	$E_{ac\_2_D}$(eV)	μ_{zz} ($cm^2V^{-1}s^{-1}$)	μ_{ac}($cm^2V^{-1}s^{-1}$)
Electron (e)	0.468	0.468	134.9	135.22	-10.94	-11.84	21.52	20.89
Hole (h)	0.57	0.57	134.9	135.22	-5.84	-5.58	38.02	38.70

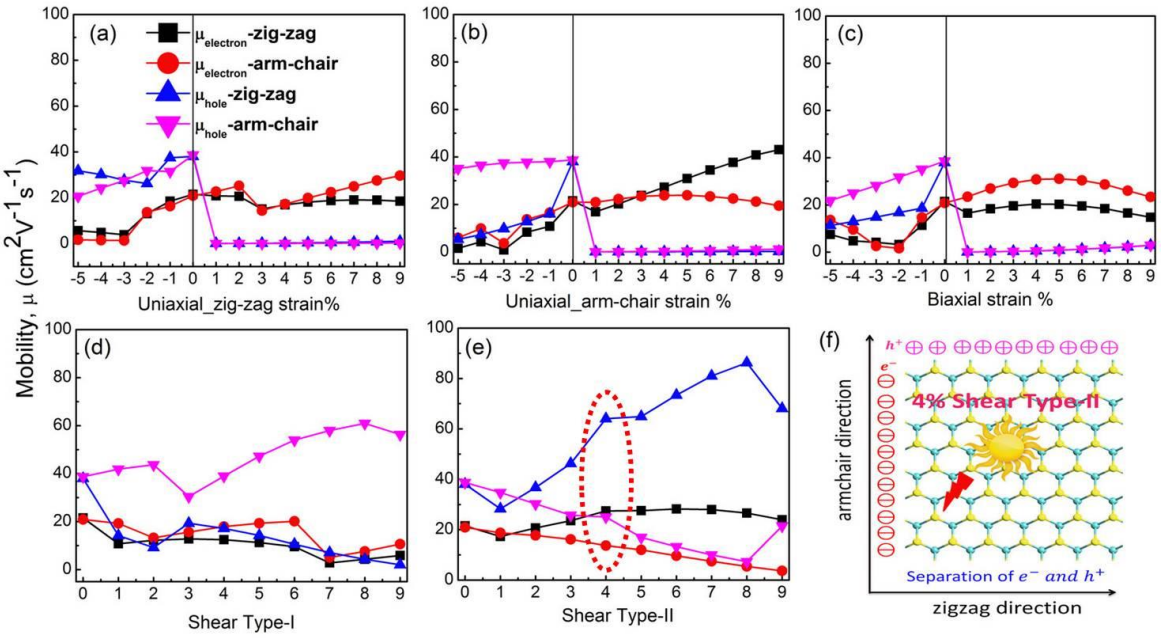

Figure 5. 8 Variation in carrier mobility (a)-(e) with the application of external mechanical strain of different types on the ML-MoS_2 nanosheet and (f) high hole to electron mobility ratio ensures an efficient separation of e^-/h^+ pairs at 3-4% of shear strain, when optical absorbance/conductivity also reaches its maximum.

For pristine ML-MoS_2, the electron mobilities are found to be 21.52 $cm^2V^{-1}s^{-1}$ and 20.89 $cm^2V^{-1}s^{-1}$ along the zz and ac direction respectively, whereas for hole mobility, it comes out to be 38.02 $cm^2V^{-1}s^{-1}$ and 38.07 $cm^2V^{-1}s^{-1}$ along the zz and ac directions respectively. Using this new formulation, the hole mobility is found to be two times the electron mobility, which is in good agreement with experimental findings[311]. While the hole to electron mobility ratio was reported to be about three, using the original deformation potential theory of Bardeen and Shockley [178], implying the higher accuracy and reliability of the most recent formulation. The effective masses and the carrier mobilities are found to be isotropic in pristine ML-MoS_2 nanosheet; however, anisotropy arises when external mechanical strain is applied to the monolayer nanosheet. To clarify the strain-induced anisotropy, the mobility of charge carriers along zz and ac direction have been plotted as a function of strain in Figure 5.8. Hole mobility drops down drastically under the application of 1% tensile strain of both types, namely, tensile and uniaxial, applied along the zz and the ac directions. The hole mobility remains nearly the same even for higher values of applied tensile strain. Shear strain of type II was found to be the most interesting one where the hole mobility increases along the zz direction while electron mobility decreases along the ac direction. At 3-4% of this strain, which is actually the optimal value for optical and electronic properties, the difference between electron mobility and the hole mobility in the transverse direction is large enough to bring about electron-hole separation

and their subsequent migration along the opposite or mutually perpendicular directions, as shown in Figure 5.8 (e)-(f). The relaxation time of the charge carriers also signify the role of shear type-II strain as explained in detail in Figure 5.9.

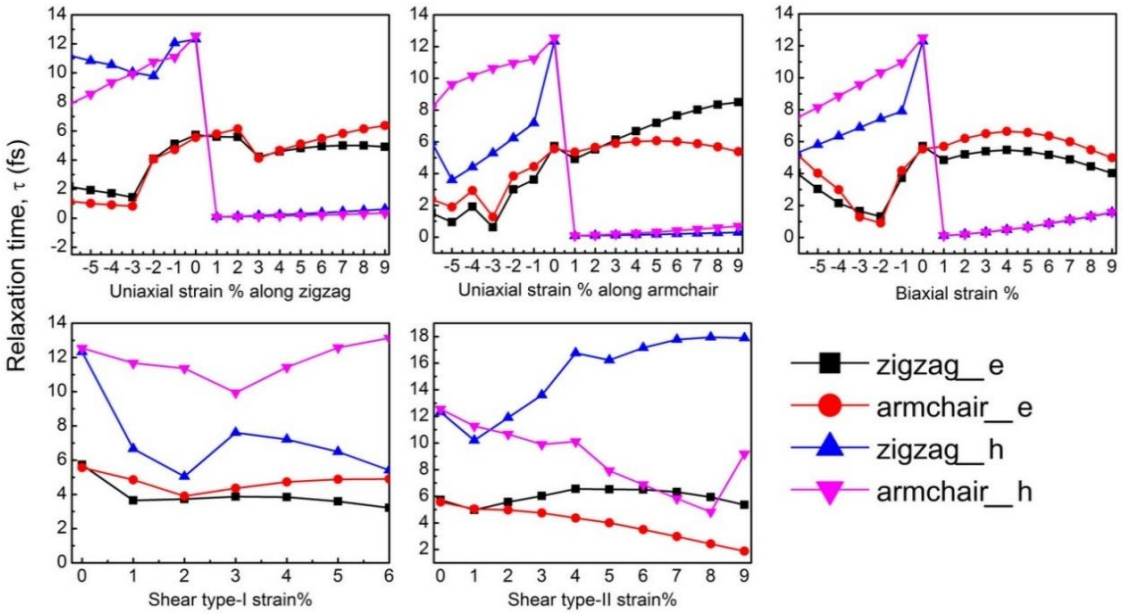

Figure 5. 9 Variation in the relaxation time of the charge carriers along the zig-zag (zz) and arm-chair (ac) direction with mechanical strain of different types applied on to monolayer MoS_2 nanosheet.

Furthermore, carrier mobility ratio of the charge carriers is calculated using relation,

$$R_{mobility\_\eta} = \frac{\max(\mu_{e}\_\eta, \mu_{h}\_\eta)}{\min(\mu_{e}\_\eta, \mu_{h}\_\eta)}$$

where η is either zz or ac direction as shown in Figure 5.10. At 1% of uniaxial tensile strain along the zz and ac direction and also with biaxial tensile strain, the carrier mobility ratio reaches its maximum value and beyond this value the ratio decreases with the further applied tensile strain. This is due to the significantly small hole mobility at 1% tensile strain. Shear strain of type-II strain is found to be very interesting where anisotropic ratio gradually increases with strain, as shown in Figure 5.10(d), which clearly indicates the higher probabilities for electron-hole separation and their migration along different directions.

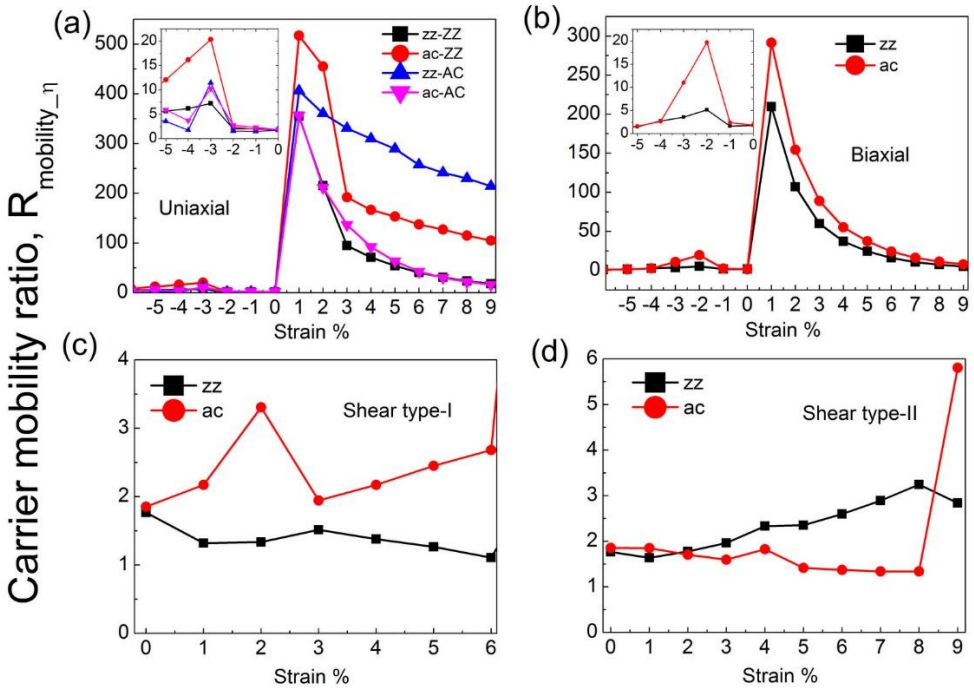

Figure 5. 10 Variation in the carrier mobility ratio with the mechanical strain applied on to the ML-MoS_2 nanosheet (a)-(d): Carrier mobility ratio, $R_{mobility\_\eta} = \frac{\max(\mu_{e\_\eta},\mu_{h\_\eta})}{\min(\mu_{e\_\eta},\mu_{h\_\eta})}$, where η is either the zigzag (zz) or armchair (ac) direction. $R_{mobility\_\eta} = \left(\frac{\mu_h}{\mu_e}\right)_\eta$ or $\left(\frac{\mu_e}{\mu_h}\right)_\eta$; $R_{mobility\_\eta} > 1$, $\mu_{e(h)}$ is the electron (hole) mobility. Labels in Fig. (a): zz-ZZ denotes anisotropy ratio, R_{ani} along the zig-zag (zz) direction for uniaxial strain applied along the zig-zag (ZZ) direction. Likewise, ac-ZZ implies anisotropy ratio along the arm-chair (ac) direction for uniaxial strain applied along the zig-zag (ZZ) direction and so on.

The selectivity of CO_2 reduction and HER is found to be tunable by pH. In Fig 5.7, the CO_2 reduction level (CO_2/HCOOH) lies closer to the conduction band edge for pH=0-3 than the water reduction potential or HER level. Therefore, in this pH range, CO_2 reduction reaction will be more thermodynamically favorable than the HER. So, CO_2 reduction reaction will be selective in the pH range (0-3). Moreover, the relative surface chemistry of these species (CO_2 Vs hydrogen) with the MoS_2 monolayer may play a role, which is addressable in future studies. Again, CO_2 reduction reaction is found to be thermodynamically forbidden for pH > 3, while HER is still favorable up to pH = 6.5-7. Therefore, HER will be selective and proceed without any competition or hindrance for pH=3-7.

5.4 Conclusion

Solar fuel production from abundant sources such as CO_2 and H_2O is a daunting research challenge that necessarily requires a number of interconnected factors to act together in unison. Strained single-layer of MoS_2 has been investigated as a potential photo-catalyst for the

generation of solar fuels and oxygen by the photo-reduction of CO_2 with H_2O. All kinds of strain have been applied to calibrate the photocatalytic response of ML-MoS_2 to strain and in turn, to ascertain the type and magnitude of strain, and pH under which the photocatalytic response in ML-MoS_2 are optimized. All factors governing the photocatalytic activity have been fully addressed in this work: optical absorbance and conductivity, suitable band edges, exciton binding energies, carrier mobilities and their anisotropy, and pH. The excitonic binding energy for pristine monolayer MoS_2 calculated in this work (0.41eV) is in good agreement with the previous reports. The redshift in optical absorbance peaks with the application of tensile strain of both types, uniaxial and biaxial, agrees with the PL observed experimentally on monolayer MoS_2 nanosheet. Calculated optical conductivity correctly reproduces all main features measured experimentally and calculated theoretically in earlier studies. Optical absorbance and conductivity show the same trend: the peak value rises with the application of 1-5% of uniaxial tensile strain, while it reaches its maximum at 3% strain. Shear strain of both types are found to be most effective in enhancing the optical conductivity and absorbance along the direction of lattice dilation. Compressive strain is found to attenuate optical absorbance and conductivity. 3-4% of shear strain of type-II is found to be most favorable for artificial photosynthesis in monolayer MoS_2 nanosheet on account of the following reasons. The optical absorbance and conductivity are found to be maximally enhanced, while the exciton binding energies also remain desirably small under 3-4% shear strain of type II. Band edge positions in pristine ML-MoS_2 nanosheet are found to be well suited for CO_2 reduction with H_2O and oxidation of water leading to oxygen evolution reaction. Moreover, the band edges barely undergo any shift under the application of shear strain of both types, which is an additional advantage. Shear strain, in general, and shear strain of type II, in particular, brings about the highest enhancement in carrier mobility along with the carrier mobility ratio, which facilitates the charge separation and the migration of the separated $e^- - h^+$ pairs along opposite or transverse directions. As a result, the carrier lifetimes are prolonged; or, in other words, the carrier recombination rates are lowered. Nernst formulation is found to be beneficial in understanding the importance of adjusting the pH level for optimizing CO_2 reduction with H_2O and oxygen evolution reaction. Acidic medium turns out to be most suitable for carrying out such photo-conversion. This work is important from both scientific and technological perspectives. It provides an in-depth insight into the Science of photo-conversion of CO_2 with H_2O and in the natural fixation of carbon.

Chapter 6

Summary and Future Directions

The main thesis findings discussed in the different Chapters are summarized in this last Chapter.

Chapter 1 provides a broad overview of the three different kinds of energy conversion in 2D materials, while Chapter 2 introduces the theoretical background and tools used in carrying out the Ph.D. work.

Chapter 3 infers that the inversion symmetry in centrosymmetric Group IVB transition metal dichalcogenide (TMDC) monolayers occurring in 1T phase is broken upon the formation of its Janus structures and in turn, piezoelectricity is induced. Quantitatively, the piezoelectric constants have been split into its electronic and ionic components in order to highlight the dominance of the ionic contribution to the piezoelectric coefficient. Piezoelectric coefficient (d_{22} = 4.68 - 14.58 pm/V) in the Janus structures in Group IVB TMDC monolayers are found to be much higher than that in single layer 1H-MoS_2 (d_{11} = 2.99 pm/V). Dynamical, mechanical and thermodynamic properties confirm the all-around stability of these monolayers. A colossal enhancement in the piezoelectric coefficients in Janus HfSSe is observed under the application of uniaxial tensile strain along the arm-chair direction, where d_{22} goes to 123.04 pm/V at 9% strain, reaching the level of the piezoelectric coefficients in the state-of-the-art perovskites. This work highlights an interesting avenue to induce a high level of piezoelectricity in 2D materials. Moreover, as Janus monolayer, MoSSe, has been experimentally synthesized, formation of Janus monolayer structures in the Group IVB transition metal dichalcogenides will be viable via the same synthesis route.

In Chapter 4, thermoelectric properties in ML-MoS_2 nanosheet have been found to be sensitive to the application of mechanical strain, implying that strain can serve as an important avenue in tuning the thermoelectric properties in 2D semiconducting transition metal dichalcogenides. Out of the three modes of compressive strain, uniaxial strain along the zig-zag direction is found to be most effectual due to the higher electron mobility and its sensitivity to lattice compression along this direction. Relaxation time-scaled thermoelectric power factor is found to be higher upon n-type doping as compared to p-type doping. As a result, the maximal enhancement in $S^2\sigma/\tau$, upon optimal n-type doping, is found to occur under the application 3% of uniaxial compressive strain, when the electronic band gap and Seebeck coefficient, S reaches its maximum. At T = 900 K and 3% of compressive strain along zig-zag direction, the thermoelectric power factor is found to attain its maximum value of 51.75 x 10^{10} $Wm^{-1}K^{-2}s^{-1}$.

Strain sensitivity of the thermoelectric properties in 2D materials can be gainfully exploited in practical applications. Experimentally, application of up to 3% compressive strain has been possible. Therefore, compressive strain can be highly feasibly applied in adjusting the thermoelectric properties in nanosheets.

A systematic investigation of ultralow lattice thermal conductivities of HfS_2, $HfSe_2$ and their Janus derivative HfSSe monolayers is carried out by means of second-order harmonic and third-order anharmonic interatomic force constants. The large LO-TO splitting around the Γ-point induced by the substantially high phonon-electric field coupling effect that results from the domination of ionic bond character and high Born-effective/dynamical charges has been adequately addressed. This effect brings about a striking difference in the lattice thermal conductivities upon the incorporation of non-analytical correction term. Small magnitudes of phonon lifetimes combined with reduced group velocities, lead to a severely low lattice thermal conductivities. The calculated mode Grüneisen parameter is found to be as high as ~ 2.0 at $300\ K$, which is a fairly large value in 2D materials, indicating a strong anharmonicity in these monolayers. A clear understanding of the origin of thermal conductivities can be optimally utilized in choosing appropriate materials judiciously in designing efficient thermoelectric devices.

Finally, Chapter 5 concludes that the solar fuel production from abundant sources such as CO_2 and H_2O is a daunting research challenge that necessarily requires a number of interconnected factors to act together in unison. Strained single-layer of MoS_2 has been investigated as a potential photo-catalyst for the generation of solar fuels and oxygen by the photoreduction of CO_2 with H_2O. 4-5% of shear strain of type-II is found to be the most optimum one as it maximally enhances the optical absorbance and conductivity. The exciton binding energies are also desirably small under 4-5% shear strain. Band edge positions of pristine ML-MoS_2 are found to be well suited for CO_2 reduction with H_2O. Moreover, the band edges barely undergo any shift under the application of shear strain, which is an additional advantage. Shear strain in general, and shear strain of type II, in particular, brings about the highest enhancement in carrier mobility and its anisotropy which facilitates the charge separation and the migration of the separated $e^- - h^+$ pairs along transverse directions. As a result, the carrier lifetimes are prolonged; or, in other words, the recombination rate of electrons and holes are lowered. Nernst formulation is found to be beneficial in understanding the importance of adjusting the pH level for optimizing CO_2 reduction with H_2O and producing oxygen. Acidic medium turns out to be most suitable for carrying out such photoconversion. It provides an in-depth insight into the Science of photoconversion and useful pointers to experimentalists and technologists on

photoreduction of CO_2 with H_2O and in the natural fixation of carbon. Direct application of strain has been scarcely investigated in photocatalytic studies in experiments. However, the feasibility of applying elastic strain reversibly can be immensely beneficial in tuning the photocatalytic or artificial photosynthetic activities in a very controlled manner.

Appendix

Appendix I

Lattice thermal conductivity

The lattice thermal conductivity, k_L is calculated by solving the linearized phonon Boltzmann transport equation (LBTE) under the single-mode-relaxation-time (SMRT) method as implemented in Phono3py [242] package, the lattice thermal conductivity tensor can be written in a closed-form. k_L can be calculated as [242]

$$k_L = \frac{1}{NV_0}\sum_{\lambda} C_{ph,\lambda} v_\lambda \otimes v_\lambda \tau_\lambda^{SMRT},$$

where V_0 is the volume of a unit cell, v_λ and τ_λ^{SMRT} are the group velocity and SMRT of the phonon mode λ, respectively. $C_{ph,\lambda}$ is the mode-dependent specific heat capacity defined as [242]

$$C_{ph,\lambda} = k_B \left(\frac{\hbar\omega_\lambda}{k_B T}\right)^2 \frac{\exp(\hbar\omega_\lambda/k_B T)}{[\exp(\hbar\omega_\lambda/k_B T) - 1]^2}$$

The mode-specific phonon group velocity can be obtained directly from the eigen-value equation:

$$v_\alpha(\lambda) \equiv \frac{\partial \omega_\lambda}{\partial q_\alpha}$$

$$= \frac{1}{2\omega_\lambda} \sum_{kk'\beta\gamma} W_\beta(k,\lambda) \frac{\partial D_{\beta\gamma}}{\partial q_\alpha} W_\gamma(k',\lambda)$$

The single-mode relaxation time, τ_λ^{SMRT} can be approximated by the phonon lifetime τ_λ, which is the reciprocal of the phonon linewidth $2\Gamma_\lambda(\omega)$

$$\tau_\lambda^{SMRT} = \tau_\lambda = \frac{1}{2\Gamma_\lambda(\omega)}$$

Cumulative lattice thermal conductivity

The cumulative lattice thermal conductivity, k_c is defined as [242]

$$k_c(\omega) = \int_0^\omega \frac{1}{N}\sum_{\lambda} k_\lambda \, \delta(\omega_\lambda - \omega') d\omega'$$

k_λ is the contribution to k from the phonon mode λ which is defined as

$$k_\lambda = \frac{1}{V_0} C_\lambda v_\lambda \otimes v_\lambda \tau_\lambda$$

Appendix II

Mode Grüneisen parameter

The dimensionless mode-Gruneisen parameter can be written by relating the shifts in phonon frequencies modes {q, j} with respect to the varying volume, but a more general way is to define it is by the application of external strain [312]

$$\gamma_{\mu\nu}(qj) = -\frac{1}{\omega_{qj}} \frac{\partial \omega_{qj}}{\partial \eta_{\mu\nu}}$$

For the present work, within the DFT-based approach, γ_{qj} is obtained from third-order IFCs using the following relation [312]-[313]

$$\gamma_{qj} = -\frac{1}{2\omega_{qj}^2} \sum_{l'l''} \sum_{kk'k''} \sum_{\alpha\beta\gamma} \frac{W_{qj}^{\alpha k*} W_{qj}^{\beta k'}}{\sqrt{m_k m_{k'}}} \times \Phi_{\alpha\beta\gamma}(0k, l'k', l''k'') \times e^{iq.[r(l'k')-r(0k))]} \times r(l''k''\gamma)$$

Appendix III

Non-analytical correction (NAC) term

LO-TO mode spitting is calculated by including the long-range Coulomb interactions with the non-analytic term correction [243,244]. The required dielectric constant (ϵ^∞) and Born effective charges (Z^*) are obtained by using the framework of DFPT [115].

$$D_{\alpha\beta}(jj', q \to 0) = D_{\alpha\beta}(jj', q = 0) + \frac{1}{\sqrt{m_j m_{j'}}} \frac{4\pi}{\Omega_0} \frac{\left[\sum_\gamma q_\gamma Z^*_{j,\gamma\alpha}\right]\left[\sum_{\gamma'} q_{\gamma'} Z^*_{j'\gamma'\beta}\right]}{\sum_{\alpha\beta} q_\alpha \epsilon^\infty_{\alpha\beta} q_\beta}$$

Bibliography

[1] C.S. Smith, Materials and the Development of Civilization and Science, Science (80-.). 148 (1965) 908–917.

[2] R. Peierls, Quelques proprietes typiques des corpses solides, Ann. I. H. Poincare. 5 (1935) 177–222.

[3] L.D. Landau, Zur Theorie der phasenumwandlungen II, Phys. Z. Sowjetunion. 11 (1937) 26–35.

[4] N.D. Mermin, H. Wagner, Absence of ferromagnetism or antiferromagnetism in one-or two-dimensional isotropic Heisenberg models, Phys. Rev. Lett. 17 (1966) 1133.

[5] N.D. Mermin, Crystalline order in two dimensions, Phys. Rev. 176 (1968) 250–254.

[6] A.K.G. K. S. Novoselov, A.A.F. S. V. Morozov, D. Jiang, Y. Zhang, S. V. Dubonos, I. V. Grigorieva, Electric Field Effect in Atomically Thin Carbon Films, Science (80-.). 306 (2004) 666. doi:10.1126/science.1102896.

[7] A. Molle, J. Goldberger, M. Houssa, Y. Xu, S.-C. Zhang, D. Akinwande, Buckled two-dimensional Xene sheets, Nat Mater. 16 (2017) 163–169.

[8] S. Zhang, S. Guo, Z. Chen, Y. Wang, H. Gao, J. Gómez-Herrero, P. Ares, F. Zamora, Z. Zhu, H. Zeng, Recent progress in 2D group-VA semiconductors: From theory to experiment, Chem. Soc. Rev. 47 (2018) 982–1021. doi:10.1039/c7cs00125h.

[9] M. Pumera, Z. Sofer, 2D Monoelemental Arsenene, Antimonene, and Bismuthene: Beyond Black Phosphorus, Adv. Mater. 29 (2017) 1605299. doi:10.1002/adma.201605299.

[10] Q.H. Wang, K. Kalantar-Zadeh, A. Kis, J.N. Coleman, M.S. Strano, Electronics and optoelectronics of two-dimensional transition metal dichalcogenides, Nat. Nanotechnol. 7 (2012) 699–712. doi:10.1038/nnano.2012.193.

[11] Z.Y. Al Balushi, K. Wang, R.K. Ghosh, R.A. Vilá, S.M. Eichfeld, J.D. Caldwell, X. Qin, Y.C. Lin, P.A. Desario, G. Stone, S. Subramanian, D.F. Paul, R.M. Wallace, S. Datta, J.M. Redwing, J.A. Robinson, Two-dimensional gallium nitride realized via graphene encapsulation, Nat. Mater. 15 (2016) 1166–1171. doi:10.1038/nmat4742.

[12] M. Naguib, O. Mashtalir, J. Carle, V. Presser, J. Lu, L. Hultman, Y. Gogotsi, M.W. Barsoum, Two-dimensional transition metal carbides., ACS Nano. 6 (2012) 1322–1331.

doi:10.1021/nn204153h.

[13] D.J. Late, B. Liu, J. Luo, A. Yan, H.S.S.R. Matte, M. Grayson, C.N.R. Rao, V.P. Dravid, GaS and GaSe ultrathin layer transistors, Adv. Mater. 24 (2012) 3549–3554. doi:10.1002/adma.201201361.

[14] B. Huang, G. Clark, E. Navarro-Moratalla, D.R. Klein, R. Cheng, K.L. Seyler, D. Zhong, E. Schmidgall, M.A. McGuire, D.H. Cobden, W. Yao, D. Xiao, P. Jarillo-Herrero, X. Xu, Layer-dependent ferromagnetism in a van der Waals crystal down to the monolayer limit., Nature. 546 (2017) 270–273. doi:10.1038/nature22391.

[15] A.Y. Lu, H. Zhu, J. Xiao, C.P. Chuu, Y. Han, M.H. Chiu, C.C. Cheng, C.W. Yang, K.H. Wei, Y. Yang, Y. Wang, D. Sokaras, D. Nordlund, P. Yang, D.A. Muller, M.Y. Chou, X. Zhang, L.J. Li, Janus monolayers of transition metal dichalcogenides, Nat. Nanotechnol. 12 (2017) 744–749. doi:10.1038/nnano.2017.100.

[16] B. Radisavljevic, A. Radenovic, J. Brivio, V. Giacometti, A. Kis, Single-layer MoS2 transistors, Nat. Nanotechnol. 6 (2011) 147–150.

[17] K.F. Mak, K. He, J. Shan, T.F. Heinz, Control of valley polarization in monolayer MoS2 by optical helicity, Nat. Nanotechnol. 7 (2012) 494–498.

[18] A.K. Geim, I. V Grigorieva, Van der Waals heterostructures., Nature. 499 (2013) 419–25. doi:10.1038/nature12385.

[19] J.K. Ellis, M.J. Lucero, G.E. Scuseria, The indirect to direct band gap transition in multilayered MoS2as predicted by screened hybrid density functional theory, Appl. Phys. Lett. 99 (2011) 261908. doi:10.1063/1.3672219.

[20] T.T. Tran, K. Bray, M.J. Ford, M. Toth, I. Aharonovich, Quantum emission from hexagonal boron nitride monolayers, Nat. Nanotechnol. 11 (2016) 37–41. doi:10.1038/nnano.2015.242.

[21] A.S. Rodin, A. Carvalho, A.H. Castro Neto, Strain-induced gap modification in black phosphorus, Phys. Rev. Lett. 112 (2014) 176801. doi:10.1103/PhysRevLett.112.176801.

[22] Letian Dou, Andrew B. Wong, Yi Yu, Minliang Lai, Nikolay Kornienko, Samuel W. Eaton, Anthony Fu, Connor G. Bischak, Jie Ma, Tina Ding, Naomi S. Ginsberg, Lin-Wang Wang, Paul Alivisatos, Peidong Yang, Atomically thin two-dimensional organic-inorganic hybrid perovskites, Science (80-.). 349 (2015) 1518–1521. doi:10.1126/science.aaa8515.

[23] G. Cheon, K.A.N. Duerloo, A.D. Sendek, C. Porter, Y. Chen, E.J. Reed, Data Mining for New Two- and One-Dimensional Weakly Bonded Solids and Lattice-Commensurate Heterostructures, Nano Lett. 17 (2017) 1915–1923. doi:10.1021/acs.nanolett.6b05229.

[24] K. Choudhary, I. Kalish, R. Beams, F. Tavazza, High-throughput Identification and Characterization of Two-dimensional Materials using Density functional theory, Sci. Rep. 7 (2017) 5179. doi:10.1038/s41598-017-05402-0.

[25] J. Zhou, L. Shen, M.D. Costa, K.A. Persson, S.P. Ong, P. Huck, Y. Lu, X. Ma, Y. Chen, H. Tang, Y.P. Feng, 2DMatPedia, an open computational database of two-dimensional materials from top-down and bottom-up approaches, Sci. Data. 6 (2019) 86. doi:10.1038/s41597-019-0097-3.

[26] N. Mounet, M. Gibertini, P. Schwaller, D. Campi, A. Merkys, A. Marrazzo, T. Sohier, I.E. Castelli, A. Cepellotti, G. Pizzi, N. Marzari, Two-dimensional materials from high-throughput computational exfoliation of experimentally known compounds, Nat. Nanotechnol. 13 (2018) 246–252. doi:10.1038/s41565-017-0035-5.

[27] C. Lee, X. Wei, J.W. Kysar, J. Hone, Measurement of the elastic properties and intrinsic strength of monolayer graphene, Science (80-.). 321 (2008) 385–388.

[28] C.S. Ruiz-Vargas, H.L. Zhuang, P.Y. Huang, A.M. Van Der Zande, S. Garg, P.L. McEuen, D.A. Muller, R.G. Hennig, J. Park, Softened elastic response and unzipping in chemical vapor deposition graphene membranes, Nano Lett. 11 (2011) 2259–2263.

[29] K.-A.N.A.N. Duerloo, M.T. Ong, E.J. Reed, Intrinsic piezoelectricity in two-dimensional materials, J. Phys. Chem. Lett. 3 (2012) 2871–2876. doi:10.1021/jz3012436.

[30] L.D. Zhao, S.H. Lo, Y. Zhang, H. Sun, G. Tan, C. Uher, C. Wolverton, V.P. Dravid, M.G. Kanatzidis, Ultralow thermal conductivity and high thermoelectric figure of merit in SnSe crystals, Nature. 508 (2014) 373–377. doi:10.1038/nature13184.

[31] K. Peng, X. Lu, H. Zhan, S. Hui, X. Tang, G. Wang, J. Dai, C. Uher, G. Wang, X. Zhou, Broad temperature plateau for high ZTs in heavily doped p-type SnSe single crystals, Energy Environ. Sci. 9 (2016) 454–460. doi:10.1039/c5ee03366g.

[32] C. Chang, G. Tan, J. He, M.G. Kanatzidis, L.D. Zhao, The Thermoelectric Properties of SnSe Continue to Surprise: Extraordinary Electron and Phonon Transport, Chem. Mater. 30 (2018) 7355–7367. doi:10.1021/acs.chemmater.8b03732.

[33] H.L. Zhuang, R.G. Hennig, Theoretical perspective of photocatalytic properties of single-layer SnS2, Phys. Rev. B - Condens. Matter Mater. Phys. 88 (2013) 115314. doi:10.1103/PhysRevB.88.115314.

[34] Y. Sun, H. Cheng, S. Gao, Z. Sun, Q. Liu, Q. Leu, F. Lei, T. Yao, J. He, S. Wei, Y. Xie, Freestanding tin disulfide single-layers realizing efficient visible-light water splitting, Angew. Chemie - Int. Ed. 51 (2012) 8727–8731. doi:10.1002/anie.201204675.

[35] H. Park, A. Wadehra, J.W. Wilkins, A.H. Castro Neto, Magnetic states and optical properties of single-layer carbon-doped hexagonal boron nitride, Appl. Phys. Lett. 100 (2012) 253115.

[36] H.L. Zhuang, R.G. Hennig, Computational search for single-layer transition-metal dichalcogenide photocatalysts, J. Phys. Chem. C. 117 (2013) 20440–20445.

[37] H.L. Zhuang, R.G. Hennig, Single-layer group-III monochalcogenide photocatalysts for water splitting, Chem. Mater. 25 (2013) 3232–3238. doi:10.1021/cm401661x.

[38] M. Yi, Z. Shen, A review on mechanical exfoliation for the scalable production of graphene, J. Mater. Chem. A. 3 (2015) 11700–11715. doi:10.1039/c5ta00252d.

[39] J. Shen, Y. He, J. Wu, C. Gao, K. Keyshar, X. Zhang, Y. Yang, M. Ye, R. Vajtai, J. Lou, P.M. Ajayan, Liquid Phase Exfoliation of Two-Dimensional Materials by Directly Probing and Matching Surface Tension Components, Nano Lett. 15 (2015) 5449–5454. doi:10.1021/acs.nanolett.5b01842.

[40] Y. Xu, H. Cao, Y. Xue, B. Li, W. Cai, Liquid-Phase Exfoliation of Graphene: An Overview on Exfoliation Media, Techniques, and Challenges, Nanomaterials. 8 (2018) 942. doi:10.3390/nano8110942.

[41] A. Koma, Van der Waals epitaxy for highly lattice-mismatched systems, J. Cryst. Growth. 201 (1999) 236–241. doi:10.1016/S0022-0248(98)01329-3.

[42] B. Hunt, T. Taniguchi, P. Moon, M. Koshino, R.C. Ashoori, Massive Dirac Fermions and Hofstadter Butterfly in a, Science (80-.). 340 (2013) 1427–1431. doi:10.1594/PANGAEA.808834.

[43] L. Britnell, R.M. Ribeiro, A. Eckmann, R. Jalil, B.D. Belle, A. Mishchenko, Y.J. Kim, R. V. Gorbachev, T. Georgiou, S. V. Morozov, A.N. Grigorenko, A.K. Geim, C. Casiraghi, A.H.C. Neto, K.S. Novoselov, Strong Light-Matter Interactions Thin Films, Science (80-.). 340 (2013) 1311--1314. doi:10.1126/science.1235547.

[44] W. Zhang, Q. Wang, Y. Chen, Z. Wang, A.T.S. Wee, Van der Waals stacked 2D layered materials for optoelectronics, 2D Mater. 3 (2016) 22001. doi:10.1088/2053-1583/3/2/022001.

[45] M. Offidani, M. Milletarì, R. Raimondi, A. Ferreira, Optimal Charge-to-Spin Conversion in Graphene on Transition-Metal Dichalcogenides, Phys. Rev. Lett. 119 (2017) 196801. doi:10.1103/PhysRevLett.119.196801.

[46] L.A. Benítez, J.F. Sierra, W. Savero Torres, A. Arrighi, F. Bonell, M. V. Costache, S.O. Valenzuela, Strongly anisotropic spin relaxation in graphene-transition metal dichalcogenide heterostructures at room temperature, Nat. Phys. 14 (2018) 303–308. doi:10.1038/s41567-017-0019-2.

[47] U. Maitra, S.R. Lingampalli, C.N.R. Rao, Artificial photosynthesis and the splitting of water to generate hydrogen, Curr. Sci. 106 (2014) 518–527.

[48] B. Walsh, P. Ciais, I.A. Janssens, J. Penuelas, K. Riahi, F. Rydzak, D.P. van Vuuren, M. Obersteiner, J. Peñuelas, K. Riahi, F. Rydzak, D.P. van Vuuren, M. Obersteiner, Pathways for balancing CO2 emissions and sinks, Nat. Commun. 8 (2017) 148568. doi:10.1038/ncomms14856.

[49] R.J. Francey, C.M. Trudinger, M. Van Der Schoot, R.M. Law, P.B. Krummel, R.L. Langenfelds, L.P. Steele, C.E. Allison, A.R. Stavert, R.J. Andres, Atmospheric verification of anthropogenic CO2 emission trends, Nat. Clim. Chang. 3 (2013) 520–524.

[50] S.I. Seneviratne, M.G. Donat, A.J. Pitman, R. Knutti, R.L. Wilby, Allowable CO2 emissions based on regional and impact-related climate targets, Nature. 529 (2016) 477–483.

[51] P. Friedlingstein, R.M. Andrew, J. Rogelj, G.P. Peters, J.G. Canadell, R. Knutti, G. Luderer, M.R. Raupach, M. Schaeffer, D.P. Van Vuuren, Persistent growth of CO2 emissions and implications for reaching climate targets, Nat. Geosci. 7 (2014) 709–715.

[52] R.B. Jackson, J.G. Canadell, C. Le Quéré, R.M. Andrew, J.I. Korsbakken, G.P. Peters, N. Nakicenovic, Reaching peak emissions, Nat. Clim. Chang. 6 (2016) 7–10.

[53] H. Fu, R.E. Cohen, Polarization rotation mechanism for ultrahigh electromechanical response in single-crystal piezoelectrics, Nature. 403 (2000) 281–283.

[54] Z. Lin, J. Song, Piezoelectric Nanogenerators Based on Zinc Oxide Nanowire Arrays

Author(s): Zhong Lin Wang and Jinhui Song Source:, Science (80-.). 312 (2006) 242–246. doi:10.1126/science.1124005.

[55] H. Zhu, Y. Wang, J. Xiao, M. Liu, S. Xiong, Z.J. Wong, Z. Ye, Y. Ye, X. Yin, X. Zhang, Observation of piezoelectricity in free-standing monolayer MoS2, Nat. Nanotechnol. 10 (2015) 151–155. doi:10.1038/nnano.2014.309.

[56] K.N. Duerloo, M.T. Ong, E.J. Reed, Intrinsic Piezoelectricity in 2D Materials Intrinsic Piezoelectricity in 2D Materials, (2012).

[57] W. Li, J. Li, Piezoelectricity in two-dimensional group-III monochalcogenides, Nano Res. 8 (2015) 3796–3802. doi:10.1007/s12274-015-0878-8.

[58] A. Carvalho, A.H.C. Neto, Enhanced piezoelectricity and modified dielectric screening of 2-D group-IV monochalcogenides, (2015) 1–9.

[59] W. Wu, L. Wang, Y. Li, F. Zhang, L. Lin, S. Niu, D. Chenet, X. Zhang, Y. Hao, T.F. Heinz, J. Hone, Z.L. Wang, Piezoelectricity of single-atomic-layer MoS2 for energy conversion and piezotronics, Nature. 514 (2014) 470. doi:10.1038/nature13792.

[60] G.J. Snyder, E.S. Toberer, Complex thermoelectric materials, Nat. Mater. 7 (2008) 105–114.

[61] X. Zhang, L.-D. Zhao, Thermoelectric materials: Energy conversion between heat and electricity, J. Mater. 1 (2015) 92–105.

[62] G.J. Snyder, T.S. Ursell, Thermoelectric efficiency and compatibility, Phys. Rev. Lett. 91 (2003) 148301.

[63] P.X. Thi, M. Miyata, H. Van Ngoc, P.T. Lam, N.T. Tung, M. Muruganathan, P.T. Tue, M. Akabori, D.H. Chi, H. Mizuta, Y. Takamura, M. Koyano, Thermoelectric Properties and Carrier Localization in Ultrathin Layer of Nb-Doped MoS2, Phys. Status Solidi. 255 (2018) 1800125. doi:10.1002/pssb.201800125.

[64] J. Yang, H.L. Yip, A.K.Y. Jen, Rational design of advanced thermoelectric materials, Adv. Energy Mater. 3 (2013) 549–565. doi:10.1002/aenm.201200514.

[65] Z. Jin, Q. Liao, H. Fang, Z. Liu, W. Liu, Z. Ding, T. Luo, N. Yang, A Revisit to High Thermoelectric Performance of Single-layer MoS2, Sci. Rep. 5 (2015) 18342. doi:10.1038/srep18342.

[66] Z. Feng, Y. Wang, Y. Yan, G. Zhang, J. Yang, J. Zhang, C. Wang, An impurity intermediate band due to Pb doping induced promising thermoelectric performance of

Ca5In2Sb6, Phys. Chem. Chem. Phys. 17 (2015) 15156–15164. doi:10.1039/c5cp00972c.

[67] D.B. Luo, Y.X. Wang, Y.L. Yan, G. Yang, J.M. Yang, The high thermopower of the Zintl compound Sr5Sn2As6 over a wide temperature range: First-principles calculations, J. Mater. Chem. A. 2 (2014) 15159–15167. doi:10.1039/c4ta02452d.

[68] Y. Zhou, L. Zhao, Promising Thermoelectric Bulk Materials with 2D Structures, Adv. Mater. 29 (2017) 1702676.

[69] Y. Liu, W. Wang, J. Yang, S. Li, Recent Advances of Layered Thermoelectric Materials, Adv. Sustain. Syst. 2 (2018) 1800046. doi:10.1002/adsu.201800046.

[70] G. Zhang, Y.W. Zhang, Thermal properties of two-dimensional materials, Chinese Phys. B. 27 (2017) 1604134. doi:10.1088/1674-1056/26/3/034401.

[71] S. Sharma, U. Schwingenschlögl, Thermoelectric Response in Single Quintuple Layer Bi2Te3, ACS Energy Lett. 1 (2016) 875–879. doi:10.1021/acsenergylett.6b00289.

[72] B. Xu, J. Zhang, G. Yu, S. Ma, Y. Wang, Y. Wang, Thermoelectric properties of monolayer Sb2Te3, J. Appl. Phys. 124 (2018) 165104. doi:10.1063/1.5051470.

[73] A.H. Romero, E.K.U. Gross, M.J. Verstraete, O. Hellman, Thermal conductivity in PbTe from first principles, Phys. Rev. B - Condens. Matter Mater. Phys. 91 (2015) 214310. doi:10.1103/PhysRevB.91.214310.

[74] M.-J.J. Lee, J.-H.H. Ahn, J.H. Sung, H. Heo, S.G. Jeon, W. Lee, J.Y. Song, K.-H.H. Hong, B. Choi, S.-H.H. Lee, M.H. Jo, Thermoelectric materials by using two-dimensional materials with negative correlation between electrical and thermal conductivity, Nat. Commun. 7 (2016) 12011. doi:10.1038/ncomms12011.

[75] W. Zhou, Z. Yu, H. Song, R. Fang, Z. Wu, L. Li, Z. Ni, W. Ren, L. Wang, S. Ruan, Lattice dynamics in monolayer and few-layer SnSe2, Phys. Rev. B. 96 (2017) 35401. doi:10.1103/PhysRevB.96.035401.

[76] G. Li, G. Ding, G.L. and G.D. and G. Gao, Thermoelectric properties of SnSe2 monolayer, J. Phys. Condens. Matter. 29 (2017) 015001 (7pp). doi:10.1088/0953-8984/29/1/015001.

[77] Y. Ding, B. Xiao, G. Tang, J. Hong, Transport properties and high thermopower of SnSe2: A full ab-initio investigation, J. Phys. Chem. C. 121 (2017) 225–236. doi:10.1021/acs.jpcc.6b11467.

[78] A. Banik, S. Roychowdhury, K. Biswas, The journey of tin chalcogenides towards high-performance thermoelectrics and topological materials, Chem. Commun. 54 (2018) 6573–6590. doi:10.1039/c8cc02230e.

[79] F. Caruso, M. Troppenz, S. Rigamonti, C. Draxl, Thermally enhanced Fröhlich coupling in SnSe, Phys. Rev. B. 99 (2019) 081104 (R). doi:10.1103/physrevb.99.081104.

[80] S. Roychowdhury, M. Samanta, S. Perumal, K. Biswas, Germanium Chalcogenide Thermoelectrics: Electronic Structure Modulation and Low Lattice Thermal Conductivity †, Chem. Mater. 30 (2018) 5799–5813. doi:10.1021/acs.chemmater.8b02676.

[81] S. Hao, F. Shi, V.P. Dravid, M.G. Kanatzidis, C. Wolverton, Computational Prediction of High Thermoelectric Performance in Hole Doped Layered GeSe, Chem. Mater. 28 (2016) 3218–3226. doi:10.1021/acs.chemmater.6b01164.

[82] H. Zhou, Y. Cai, G. Zhang, Y.W. Zhang, Unusual phonon behavior and ultra-low thermal conductance of monolayer InSe, Nanoscale. 10 (2018) 480–487. doi:10.1039/c7nr07779c.

[83] H. Wang, G. Qin, G. Li, Q. Wang, M. Hu, Low thermal conductivity of monolayer ZnO and its anomalous temperature dependence, Phys. Chem. Chem. Phys. 19 (2017) 12882–12889. doi:10.1039/c7cp00460e.

[84] J. Gao, A. Hu, W. Tang, M. Sun, J.-P. Chou, L. Shi, G. Zhang, Few-Layer PdSe2 Sheets: Promising Thermoelectric Materials Driven by High Valley Convergence, ACS Omega. 3 (2018) 5971–5979. doi:10.1021/acsomega.8b00485.

[85] D.O. Lindroth, P. Erhart, Thermal transport in van der Waals solids from first-principles calculations, Phys. Rev. B. 94 (2016) 115205. doi:10.1103/PhysRevB.94.115205.

[86] Y. Cai, J. Lan, G. Zhang, Y.-W.W. Zhang, Lattice vibrational modes and phonon thermal conductivity of monolayer MoS2, Phys. Rev. B. 89 (2014) 35438. doi:10.1103/PhysRevB.89.035438.

[87] Dimple, N. Jena, A. De Sarkar, Compressive strain induced enhancement in thermoelectric-power-factor in monolayer MoS2 nanosheet, J. Phys. Condens. Matter. 29 (2017) 225501. doi:10.1088/1361-648X/aa6cbc.

[88] M. Zare, B.Z. Rameshti, F.G. Ghamsari, R. Asgari, Thermoelectric transport in monolayer phosphorene, Phys. Rev. B. 95 (2017) 45422.

doi:10.1103/PhysRevB.95.045422.

[89] S. Sharma, N. Singh, U. Schwingenschlögl, Two-Dimensional Tellurene as Excellent Thermoelectric Material, ACS Appl. Energy Mater. 1 (2018) 1950–1954. doi:10.1021/acsaem.8b00032.

[90] R. Levy, Solar energy conversion can be small-scale and low-tech, Phys. Today. 60 (2007) 12–14.

[91] A. Fujishima, K. Honda, Electrochemical photolysis of water at a semiconductor electrode, Nature. 238 (1972) 37.

[92] J. Xing, W.Q. Fang, H.J. Zhao, H.G. Yang, Inorganic photocatalysts for overall water splitting, Chem. Asian J. 7 (2012) 642–657.

[93] S.N. Habisreutinger, L. Schmidt-Mende, J.K. Stolarczyk, Photocatalytic reduction of CO2 on TiO2 and other semiconductors, Angew. Chemie Int. Ed. 52 (2013) 7372–7408.

[94] U.G. Akpan, B.H. Hameed, Parameters affecting the photocatalytic degradation of dyes using TiO2-based photocatalysts: a review, J. Hazard. Mater. 170 (2009) 520–529.

[95] J.L. White, M.F. Baruch, J.E. Pander III, Y. Hu, I.C. Fortmeyer, J.E. Park, T. Zhang, K. Liao, J. Gu, Y. Yan, Light-driven heterogeneous reduction of carbon dioxide: Photocatalysts and photoelectrodes, Chem. Rev. 115 (2015) 12888–12935.

[96] B. Luo, G. Liu, L. Wang, Recent advances in 2D materials for photocatalysis, Nanoscale. 8 (2016) 6904–6920.

[97] T. Takagahara, K. Takeda, Theory of the quantum confinement effect on excitons in quantum dots of indirect-gap materials, Phys. Rev. B. 46 (1992) 15578.

[98] Y.-W. Son, M.L. Cohen, S.G. Louie, Energy gaps in graphene nanoribbons, Phys. Rev. Lett. 97 (2006) 216803.

[99] Y. Sun, S. Gao, F. Lei, Y. Xie, Atomically-thin two-dimensional sheets for understanding active sites in catalysis, Chem. Soc. Rev. 44 (2015) 623–636.

[100] Q. Wan, T.H. Wang, J.C. Zhao, Enhanced photocatalytic activity of ZnO nanotetrapods, Appl. Phys. Lett. 87 (2005) 83105.

[101] M. Born, R. Oppenheimer, Zur quantentheorie der molekeln, Ann. Phys. 389 (1927) 457–484.

[102] L.H. Thomas, The calculation of atomic fields, in: Math. Proc. Cambridge Philos. Soc.,

Cambridge University Press, 1927: pp. 542–548.

[103] E. Fermi, Statistical method to determine some properties of atoms, Rend. Accad. Naz. Lincei. 6 (1927) 602–607.

[104] P. Hohenberg, W. Kohn, Inhomogeneous electron gas, Phys. Rev. 136 (1964) B864.

[105] W. Kohn, L.J. Sham, Self-Consistent Equations Including Exchange and Correlation Effects, Phys. Rev. 140 (1965) A1133–A1138. doi:10.1103/PhysRev.140.A1133.

[106] J.P. Perdew, K. Burke, M. Ernzerhof, Generalized Gradient Approximation Made Simple, Phys. Rev. Lett. 77 (1996) 3865–3868. doi:10.1103/PhysRevLett.77.3865.

[107] B. Santra, A. Michaelides, M. Fuchs, A. Tkatchenko, C. Filippi, M. Scheffler, On the accuracy of density-functional theory exchange-correlation functionals for H bonds in small water clusters. II. The water hexamer and van der Waals interactions, J. Chem. Phys. 129 (2008) 194111.

[108] M. Grodzicki, J.M. Seminario, P. Politzer, Energy barriers of symmetry-forbidden reactions: Local density functional calculations, J. Chem. Phys. 94 (1991) 1668–1669.

[109] O. Gunnarsson, R.O. Jones, Total-energy differences: Sources of error in local-density approximations, Phys. Rev. B. 31 (1985) 7588.

[110] I.N. Yakovkin, P.A. Dowben, The problem of the band gap in LDA calculations, Surf. Rev. Lett. 14 (2007) 481–487.

[111] A.D. Becke, A new mixing of Hartree–Fock and local density-functional theories, J. Chem. Phys. 98 (1993) 1372–1377.

[112] J. Harris, Adiabatic-connection approach to Kohn-Sham theory, Phys. Rev. A. 29 (1984) 1648.

[113] J. Heyd, G.E. Scuseria, M. Ernzerhof, Hybrid functionals based on a screened Coulomb potential, J. Chem. Phys. 118 (2003) 8207–8215.

[114] A. V Krukau, O.A. Vydrov, A.F. Izmaylov, G.E. Scuseria, Influence of the exchange screening parameter on the performance of screened hybrid functionals, J. Chem. Phys. 125 (2006) 224106.

[115] X. Wu, D. Vanderbilt, D.R. Hamann, Systematic treatment of displacements, strains, and electric fields in density-functional perturbation theory, Phys. Rev. B - Condens. Matter Mater. Phys. 72 (2005) 35105. doi:10.1103/PhysRevB.72.035105.

[116] S. Baroni, S. De Gironcoli, A.D. Corso, S. Scuola, I. Superiore, I. Istituto, F. Materia, I.- Trieste, P. Giannozzi, S. De Gironcoli, A. Dal Corso, P. Giannozzi, Phonons and related crystal properties from density-functional perturbation theory, Rev. Mod. Phys. 73 (2001) 515.

[117] S. Baroni, R. Resta, Ab initio calculation of the macroscopic dielectric constant in silicon, Phys. Rev. B. 33 (1986) 7017–7021. doi:10.1103/PhysRevB.33.7017.

[118] K.F. Mak, C. Lee, J. Hone, J. Shan, T.F. Heinz, Atomically thin MoS2: a new direct-gap semiconductor, Phys. Rev. Lett. 105 (2010) 136805.

[119] M.M. Alyörük, Y. Aierken, D. Çaklr, F.M. Peeters, C. Sevik, Promising Piezoelectric Performance of Single Layer Transition- Metal Dichalcogenides and Dioxides, J. Phys. Chem. C. 119 (2015) 23231–23237. doi:10.1021/acs.jpcc.5b06428.

[120] L.C. Gomes, A. Carvalho, A.H. Castro Neto, Enhanced piezoelectricity and modified dielectric screening of two-dimensional group-IV monochalcogenides, Phys. Rev. B - Condens. Matter Mater. Phys. 92 (2015) 1–8. doi:10.1103/PhysRevB.92.214103.

[121] R. Fei, W. Li, J. Li, L. Yang, Giant piezoelectricity of monolayer group IV monochalcogenides: SnSe, SnS, GeSe, and GeS, Appl. Phys. Lett. 107 (2015). doi:10.1063/1.4934750.

[122] H. Yin, J. Gao, G.P. Zheng, Y. Wang, Y. Ma, Giant Piezoelectric Effects in Monolayer Group-V Binary Compounds with Honeycomb Phases: A First-Principles Prediction, J. Phys. Chem. C. 121 (2017) 25576–25584. doi:10.1021/acs.jpcc.7b08822.

[123] W. Wu, Z.L. Wang, Piezotronics and piezo-phototronics for adaptive electronics and optoelectronics, Nat. Rev. Mater. 1 (2016) 16031.

[124] Z.L. Wang, Progress in piezotronics and piezo-phototronics, Adv. Mater. 24 (2012) 4632–4646.

[125] M.B. Starr, J. Shi, X. Wang, Piezopotential-Driven Redox Reactions at the Surface of Piezoelectric Materials, Angew. Chemie Int. Ed. 51 (2012) 5962–5966.

[126] M.B. Starr, X. Wang, Fundamental analysis of piezocatalysis process on the surfaces of strained piezoelectric materials, Sci. Rep. 3 (2013) 2160.

[127] M.K. Lo, S.Y. Lee, K.S. Chang, Study of ZnSnO3-nanowire piezophotocatalyst using two-step hydrothermal synthesis, J. Phys. Chem. C. 119 (2015) 5218–5224. doi:10.1021/acs.jpcc.5b00282.

[128] L. Dong, J. Lou, V.B. Shenoy, Large In-Plane and Vertical Piezoelectricity in Janus Transition Metal Dichalchogenides, ACS Nano. 11 (2017) 8242–8248. doi:10.1021/acsnano.7b03313.

[129] Y. Guo, S. Zhou, Y. Bai, J. Zhao, Enhanced piezoelectric effect in Janus group-III chalcogenide monolayers, Appl. Phys. Lett. 110 (2017). doi:10.1063/1.4981877.

[130] J. Zhang, S. Jia, I. Kholmanov, L. Dong, D. Er, W. Chen, H. Guo, Z. Jin, V.B. Shenoy, L. Shi, J. Lou, Janus Monolayer Transition-Metal Dichalcogenides, ACS Nano. 11 (2017) 8192–8198. doi:10.1021/acsnano.7b03186.

[131] C. Tan, X. Cao, X. Wu, Q. He, J. Yang, X. Zhang, J. Chen, W. Zhao, S. Han, G. Nam, M. Sindoro, H. Zhang, Recent Advances in Ultrathin Two-Dimensional Nanomaterials, Chem. Rev. 117 (2016) 6225−6331. doi:10.1021/acs.chemrev.6b00558.

[132] S.J. Yun, G.H. Han, H. Kim, D.L. Duong, B.G. Shin, J. Zhao, Q.A. Vu, J. Lee, S.M. Lee, Y.H. Lee, Telluriding monolayer MoS2 and WS2 via alkali metal scooter, Nat. Commun. 8 (2017) 2163.

[133] Y. Ji, M. Yang, H. Lin, T. Hou, L. Wang, Y. Li, S.-T. Lee, Janus Structures of Transition Metal Dichalcogenides as the Heterojunction Photocatalysts for Water Splitting, J. Phys. Chem. C. 122 (2018) 3123–3129. doi:10.1021/acs.jpcc.7b11584.

[134] X. Ma, X. Wu, H. Wang, Y. Wang, A Janus MoSSe monolayer: a potential wide solar-spectrum water-splitting photocatalyst with a low carrier recombination rate, J. Mater. Chem. A. 6 (2018) 2295–2301. doi:10.1039/C7TA10015A.

[135] D. Er, H. Ye, N.C. Frey, H. Kumar, J. Lou, V.B. Shenoy, Prediction of Enhanced Catalytic Activity for Hydrogen Evolution Reaction in Janus Transition Metal Dichalcogenides, Nano Lett. 18 (2018) 3943–3949. doi:10.1021/acs.nanolett.8b01335.

[136] T. Hu, F. Jia, G. Zhao, J. Wu, A. Stroppa, W. Ren, Intrinsic and anisotropic Rashba spin splitting in Janus transition-metal dichalcogenide monolayers, Phys. Rev. B. 97 (2018) 235404. doi:10.1103/PhysRevB.97.235404.

[137] Q.F. Yao, J. Cai, W.Y. Tong, S.J. Gong, J.Q. Wang, X. Wan, C.G. Duan, J.H. Chu, Manipulation of the large Rashba spin splitting in polar two-dimensional transition-metal dichalcogenides, Phys. Rev. B. 95 (2017) 1–8. doi:10.1103/PhysRevB.95.165401.

[138] J. He, S. Li, Two-dimensional Janus transition-metal dichalcogenides with intrinsic ferromagnetism and half-metallicity, Comput. Mater. Sci. 152 (2018) 151–157.

doi:10.1016/j.commatsci.2018.05.049.

[139] M.J. Mleczko, C. Zhang, H.R. Lee, H.-H. Kuo, B. Magyari-Köpe, R.G. Moore, Z.-X. Shen, I.R. Fisher, Y. Nishi, E. Pop, HfSe2 and ZrSe2: Two-dimensional semiconductors with native high-κ oxides, Sci. Adv. 3 (2017) e1700481.

[140] M. Zhang, Y. Zhu, X. Wang, Q. Feng, S. Qiao, W. Wen, Y. Chen, M. Cui, J. Zhang, C. Cai, L. Xie, Controlled Synthesis of ZrS2 Monolayer and Few Layers on Hexagonal Boron Nitride, J. Am. Chem. Soc. 137 (2015) 7051–7054. doi:10.1021/jacs.5b03807.

[141] R. Yue, A.T. Barton, H. Zhu, A. Azcatl, L.F. Pena, J. Wang, X. Peng, N. Lu, L. Cheng, R. Addou, S. McDonnell, X. Peng, N. Lu, L. Cheng, J. Kim, L. Colombo, R.M. Wallace, A. Azcatl, R. Yue, C.L. Hinkle, L.F. Pena, M.J. Kim, J. Wang, A.T. Barton, J.W.P. Hsu, H. Zhu, R. Addou, A. Azcatl, L.F. Pena, J. Wang, X. Peng, N. Lu, L. Cheng, R. Addou, HfSe2 thin films: 2D transition metal dichalcogenides grown by molecular beam epitaxy, ACS Nano. 9 (2014) 474–480. doi:10.1021/nn5056496.

[142] C. Yan, C. Gong, P. Wangyang, J. Chu, K. Hu, C. Li, X. Wang, X. Du, T. Zhai, Y. Li, J. Xiong, 2D Group IVB Transition Metal Dichalcogenides, Adv. Funct. Mater. 1803305 (2018) 1–18. doi:10.1002/adfm.201803305.

[143] T. Kanazawa, T. Amemiya, A. Ishikawa, V. Upadhyaya, K. Tsuruta, T. Tanaka, Y. Miyamoto, Few-layer HfS2 transistors, Sci. Rep. 6 (2016) 22277.

[144] F.A. Rasmussen, K.S. Thygesen, Computational 2D Materials Database: Electronic Structure of Transition-Metal Dichalcogenides and Oxides, J. Phys. Chem. C. 119 (2015) 13169–13183. doi:10.1021/acs.jpcc.5b02950.

[145] Q. Zhao, Y. Guo, K. Si, Z. Ren, J. Bai, X. Xu, Elastic, electronic, and dielectric properties of bulk and monolayer ZrS2 , ZrSe2 , HfS2 , HfSe2 from van der Waals density-functional theory, Phys. Status Solidi. 254 (2017) 1700033. doi:10.1002/pssb.201700033.

[146] K.H. Michel, Piezoelectricity in two-dimensional materials : Comparative study between lattice dynamics and ab initio calculations, Phys. Rev. B. 125415 (2017) 1–7. doi:10.1103/PhysRevB.95.125415.

[147] H. Yin, G.-P. Zheng, J. Gao, Y. Wang, Y. Ma, Enhanced piezoelectricity of monolayer phosphorene oxides: a theoretical study, Phys. Chem. Chem. Phys. 19 (2017) 27508–27515. doi:10.1039/C7CP05669A.

[148] G. Kresse, J. Hafner, Ab Initio Molecular-Dynamics Simulation of the Liquid-Metal-Amorphous-Semiconductor Transition in Germanium, Phys. Rev. B Condens. Matter Mater. Phys. 49 (1994) 14251–14269.

[149] G. Kresse, J. Furthmüller, Efficiency of ab-initio total energy calculations for metals and semiconductors using a plane-wave basis set, Comput. Mater. Sci. 6 (1996) 15–50. doi:10.1016/0927-0256(96)00008-0.

[150] G. and J.F. Kresse, J. Furthmüller, Efficient iterative schemes for ab initio total-energy calculations using a plane-wave basis set, Phys. Rev. B. 54 (1996) 11169. doi:10.1103/PhysRevB.54.11169.

[151] P.E. Blöchl, Projector augmented-wave method, Phys. Rev. B. 50 (1994) 17953–17979. doi:10.1103/PhysRevB.50.17953.

[152] A. Togo, I. Tanaka, First principles phonon calculations in materials science, Scr. Mater. 108 (2015) 1–5.

[153] D.L.D.L. Greenaway, R. Nitsche, Preparation and optical properties of group IV–VI2 chalcogenides having the CdI2 structure, J. Phys. Chem. Solids. 26 (1965) 1445–1458. doi:10.1016/0038-1098(65)90319-4.

[154] J.H. Han, T. Heine, P. Miró, J.H. Han, J. Cheon, T. Heine, Hexagonal Transition-Metal Chalcogenide Nanoflakes with Pronounced Lateral Quantum Confinement Hexagonal Transition-Metal Chalcogenide Nanoflakes with Pronounced Lateral Quantum Confinement **, Angew. Chemie Int. Ed. 53 (2014) 12624–12628. doi:10.1002/anie.201404704.

[155] C. Ataca, M. Topsakal, E. Akturk, S. Ciraci, A comparative study of lattice dynamics of three-and two-dimensional MoS2, J. Phys. Chem. C. 115 (2011) 16354–16361.

[156] J. Li, N. V Medhekar, V.B. Shenoy, Bonding charge density and ultimate strength of monolayer transition metal dichalcogenides, J. Phys. Chem. C. 117 (2013) 15842–15848.

[157] J. Hong, C. Lee, J.-S. Park, J.H. Shim, Control of valley degeneracy in MoS2 by layer thickness and electric field and its effect on thermoelectric properties, Phys. Rev. B. 93 (2016) 35445.

[158] V. Zólyomi, N.D. Drummond, V.I. Fal'Ko, Electrons and phonons in single layers of hexagonal indium chalcogenides from ab initio calculations, Phys. Rev. B. 89 (2014) 205416.

[159] C. Gong, H. Zhang, W. Wang, L. Colombo, R.M. Wallace, K. Cho, Band alignment of two-dimensional transition metal dichalcogenides: Application in tunnel field effect transistors, Appl. Phys. Lett. 103 (2013) 53513.

[160] Q. Peng, S. De, Outstanding mechanical properties of monolayer MoS2 and its application in elastic energy storage, Phys. Chem. Chem. Phys. 15 (2013) 19427. doi:10.1039/c3cp52879k.

[161] J. Kang, H. Sahin, F.M. Peeters, Mechanical properties of monolayer sulphides :, Phys. Chem. Chem. Phys. 17 (2015) 27742–49. doi:10.1039/C5CP04576B.

[162] W. Shi, Z. Wang, Mechanical and electronic properties of Janus monolayer transition metal dichalcogenides, J. Phys. Condens. Matter. 30 (2018) 215301.

[163] K. Liu, Q. Yan, M. Chen, W. Fan, Y. Sun, J. Suh, D. Fu, S. Lee, J. Zhou, S. Tongay, Elastic properties of chemical-vapor-deposited monolayer MoS2, WS2, and their bilayer heterostructures, Nano Lett. 14 (2014) 5097–5103.

[164] S. Bertolazzi, J. Brivio, A. Kis, Stretching and breaking of ultrathin MoS2, ACS Nano. 5 (2011) 9703–9709.

[165] A. Lipatov, H. Lu, M. Alhabeb, B. Anasori, A. Gruverman, Y. Gogotsi, A. Sinitskii, Elastic properties of 2D Ti3C2Tx MXene monolayers and bilayers, Sci. Adv. 4 (2018) 1–7.

[166] L. Song, L. Ci, H. Lu, P.B. Sorokin, C. Jin, J. Ni, A.G. Kvashnin, D.G. Kvashnin, J. Lou, B.I. Yakobson, P.M. Ajayan, Large Scale Growth and Characterization of Atomic Hexagonal Boron Nitride Layers, Nano Lett. 10 (2010) 3209–3215. doi:10.1021/nl1022139.

[167] J.J.S.J. Lee, J.Y. Park, E.B. Cho, T.Y. Kim, S.A. Han, T.Y. Kim, Y. Liu, S.S.K. Kim, C.J. Roh, H. Yoon, H. Ryu, W. Seung, J.J.S.J. Lee, J.J.S.J. Lee, S.S.K. Kim, Reliable Piezoelectricity in Bilayer WSe2 for Piezoelectric Nanogenerators, Adv. Funct. Mater. 29 (2017) 1606667. doi:10.1002/adma.201606667.

[168] J. Gao, Z. Xu, F. Li, C. Zhang, Y. Liu, G. Liu, H. He, The hydrostatic pressure dependence of the piezoelectric properties for the barium titanate and lead titanate crystals: Thermodynamic analysis, J. Appl. Phys. 109 (2011) 114111.

[169] Z. Wu, R.E. Cohen, Pressure-induced anomalous phase transitions and colossal enhancement of piezoelectricity in PbTiO3, Phys. Rev. Lett. 95 (2005) 37601.

[170] A. Kvasov, L.J. McGilly, J. Wang, Z. Shi, C.S. Sandu, T. Sluka, A.K. Tagantsev, N. Setter, Piezoelectric enhancement under negative pressure, Nat. Commun. 7 (2016) 12136.

[171] Y.-M. You, W.-Q. Liao, D. Zhao, H.-Y. Ye, Y. Zhang, Q. Zhou, X. Niu, J. Wang, P.-F. Li, D.-W. Fu, An organic-inorganic perovskite ferroelectric with large piezoelectric response, Science (80-.). 357 (2017) 306–309.

[172] N.A. Pike, B. Van Troeye, A. Dewandre, G. Petretto, X. Gonze, G.M. Rignanese, M.J. Verstraete, Origin of the counterintuitive dynamic charge in the transition metal dichalcogenides, Phys. Rev. B. 95 (2017) 1–6. doi:10.1103/PhysRevB.95.201106.

[173] F. Detraux, P. Ghosez, X. Gonze, Anomalously large Born effective charges in cubic WO 3, Phys. Rev. B. 56 (1997) 983.

[174] P. Ghosez, X. Gonze, P. Lambin, J.-P. Michenaud, Born effective charges of barium titanate: Band-by-band decomposition and sensitivity to structural features, Phys. Rev. B. 51 (1995) 6765.

[175] G. Yumnam, T. Pandey, A.K. Singh, Interplay of Structural and Bonding Characters in Thermal Conductivity and Born-Effective Charge of Transition Metal Dichalcogenides, J. Phys. Chem. C. 122 (2018) 2521–2527. doi:10.1021/acs.jpcc.7b11160.

[176] J. Bardeen, W. Shockley, Deformation potentials and mobilities in non-polar crystals, Phys. Rev. 80 (1950) 72.

[177] H. Lang, S. Zhang, Z. Liu, Mobility anisotropy of two-dimensional semiconductors, Phys. Rev. B. 94 (2016) 235306.

[178] Y. Cai, G. Zhang, Y.-W. Zhang, Polarity-reversed robust carrier mobility in monolayer MoS2 nanoribbons, J. Am. Chem. Soc. 136 (2014) 6269–6275.

[179] N. Jena, Dimple, S.D. Behere, A. De Sarkar, Strain-Induced Optimization of Nanoelectromechanical Energy Harvesting and Nanopiezotronic Response in a MoS2 Monolayer Nanosheet, J. Phys. Chem. C. 121 (2017) 9181–9190.

[180] A. Rawat, N. Jena, Dimple, A. De Sarkar, A comprehensive study on carrier mobility and artificial photosynthetic properties in group VIB transition metal dichalcogenide monolayers, J. Mater. Chem. A. 6 (2018) 8693–8704. doi:10.1039/c8ta01943f.

[181] S.H. Wei, A. Zunger, Predicted band-gap pressure coefficients of all diamond and zinc-blende semiconductors: Chemical trends, Phys. Rev. B - Condens. Matter Mater. Phys.

60 (1999) 5404–5411. doi:10.1103/PhysRevB.60.5404.

[182] J. Wiktor, A. Pasquarello, Absolute deformation potentials of two-dimensional materials, Phys. Rev. B. 94 (2016) 1–8. doi:10.1103/PhysRevB.94.245411.

[183] W. Zhang, Z. Huang, W. Zhang, Y. Li, Two-dimensional semiconductors with possible high, Nano Res. 7 (2014) 1731–1737. doi:10.1007/s12274-014-0532-x.

[184] S.H. Chae, Y. Jin, T.S. Kim, D.S. Chung, H. Na, H. Nam, H. Kim, D.J. Perello, H.Y. Jeong, T.H. Ly, Y.H. Lee, Oxidation effect in octahedral hafnium disulfide thin film, ACS Nano. 10 (2016) 1309–1316. doi:10.1021/acsnano.5b06680.

[185] J.M. Chem, X. Wang, L. Huang, X.W. Jiang, Y. Li, Z. Wei, J. Li, Large scale ZrS2 atomically thin layers, J. Mater. Chem. C. 4 (2016) 3143–3148. doi:10.1039/c6tc00254d.

[186] M.S. Dresselhaus, G. Chen, M.Y. Tang, R.G. Yang, H. Lee, D.Z. Wang, Z.F. Ren, J. Fleurial, P. Gogna, New Directions for Low-Dimensional Thermoelectric Materials, Adv. Mater. 19 (2007) 1043–1053.

[187] K.I. Bolotin, K.J. Sikes, Z. Jiang, M. Klima, G. Fudenberg, J. Hone, P. Kim, H.L. Stormer, Ultrahigh electron mobility in suspended graphene, Solid State Commun. 146 (2008) 351–355. doi:10.1016/j.ssc.2008.02.024.

[188] D. Dragoman, M. Dragoman, Giant thermoelectric effect in graphene, Appl. Phys. Lett. 91 (2007) 203116.

[189] A.K. Geim, K.S. Novoselov, The rise of graphene, Nat. Mater. 6 (2007) 183–191.

[190] J.H. Seol, I. Jo, A.L. Moore, L. Lindsay, Z.H. Aitken, M.T. Pettes, X. Li, Z. Yao, R. Huang, D. Broido, Two-dimensional phonon transport in supported graphene, Science (80-.). 328 (2010) 213–216.

[191] D. Akinwande, N. Petrone, J. Hone, Two-dimensional flexible nanoelectronics, Nat. Commun. 5 (2014) 5678.

[192] O. Lopez-Sanchez, D. Lembke, M. Kayci, A. Radenovic, A. Kis, Ultrasensitive photodetectors based on monolayer MoS2, Nat. Nanotechnol. 8 (2013) 497–501.

[193] R. Ganatra, Q. Zhang, Few-layer MoS2: a promising layered semiconductor, ACS Nano. 8 (2014) 4074–4099.

[194] A.B. Laursen, S. Kegnæs, S. Dahl, I. Chorkendorff, Molybdenum sulfides-efficient and viable materials for electro and photoelectrocatalytic hydrogen evolution, Energy Environ. Sci. 5 (2012) 5577–5591.

[195] E. Benavente, M.A. Santa Ana, F. Mendizábal, G. González, Intercalation chemistry of molybdenum disulfide, Coord. Chem. Rev. 224 (2002) 87–109.

[196] X. Zhang, Z. Lai, C. Tan, H. Zhang, Solution Processed Two Dimensional MoS2 Nanosheets: Preparation, Hybridization, and Applications, Angew. Chemie Int. Ed. 55 (2016) 8816–8838.

[197] H. Li, J. Wu, Z. Yin, H. Zhang, Preparation and applications of mechanically exfoliated single-layer and multilayer MoS2 and WSe2 nanosheets, Acc. Chem. Res. 47 (2014) 1067–1075.

[198] B. Schönfeld, J.J. Huang, S.C. Moss, Anisotropic mean-square displacements (MSD) in single-crystals of 2H-and 3R-MoS2, Acta Crystallogr. Sect. B Struct. Sci. 39 (1983) 404–407.

[199] K. Kobayashi, J. Yamauchi, Electronic structure and scanning-tunneling-microscopy image of molybdenum dichalcogenide surfaces, Phys. Rev. B. 51 (1995) 17085.

[200] S. Bhattacharyya, T. Pandey, A.K. Singh, Effect of strain on electronic and thermoelectric properties of few layers to bulk MoS2., Nanotechnology. 25 (2014) 465701. doi:10.1088/0957-4484/25/46/465701.

[201] D. Wickramaratne, F. Zahid, R. K. Lake, Electronic and thermoelectric properties of few-layer transition metal dichalcogenides, J. Chem. Phys. 140 (2014) 124710. doi:10.1063/1.4869142.

[202] W. Huang, X. Luo, C.K. Gan, S.Y. Quek, G. Liang, Theoretical study of thermoelectric properties of few-layer MoS2 and WSe2, Phys. Chem. Chem. Phys. 16 (2014) 10866–10874. doi:10.1039/C4CP00487F.

[203] K. Hippalgaonkar, Y. Wang, Y. Ye, H. Zhu, Y. Wang, J. Moore, X. Zhang, High thermo electric power factor in two-dimensional crystals of MoS2, Phys. Rev. B. 95 (2017) 115407.

[204] H. Babaei, J.M. Khodadadi, S. Sinha, Large theoretical thermoelectric power factor of suspended single-layer MoS2, Appl. Phys. Lett. 105 (2014) 193901.

[205] M. Buscema, M. Barkelid, V. Zwiller, H.S.J. van der Zant, G.A. Steele, A. Castellanos-Gomez, Large and tunable photothermoelectric effect in single-layer MoS2, Nano Lett. 13 (2013) 358–363.

[206] K.-X. Chen, X.-M. Wang, D.-C. Mo, S.-S. Lyu, Thermoelectric Properties of Transition

Metal Dichalcogenides: From Monolayers to Nanotubes, J. Phys. Chem. C. 119 (2015) 26706–26711.

[207] Z. Zhang, Y. Xie, Q. Peng, Y. Chen, A theoretical prediction of super high-performance thermoelectric materials based on MoS2/WS2 hybrid nanoribbons, Sci. Rep. 6 (2016) 21639.

[208] H.Y. Lv, W.J. Lu, D.F. Shao, H.Y. Lu, Y.P. Sun, Strain-induced enhancement in the thermoelectric performance of a ZrS2 monolayer, J. Mater. Chem. C. 4 (2016) 4538–4545.

[209] S.-D. Guo, Biaxial strain tuned thermoelectric properties in monolayer PtSe2, J. Mater. Chem. C. 4 (2016) 9366–9374. doi:10.1039/C6TC03074B.

[210] J.P. Perdew, K. Burke, M. Ernzerhof, Phys Rev Lett 77: 3865, Errata(1997) Phys Rev Lett. 78 (1996) 1396.

[211] G. Kresse, J. Hafner, Ab initio molecular-dynamics simulation of the liquid-metal–amorphous-semiconductor transition in germanium, Phys. Rev. B. 49 (1994) 14251.

[212] G. Kresse, J. Hafner, Ab initio molecular dynamics for liquid metals, Phys. Rev. B. 47 (1993) 558.

[213] G.K.H.H. Madsen, D.J. Singh, BoltzTraP. A code for calculating band-structure dependent quantities, Comput. Phys. Commun. 175 (2006) 67–71. doi:10.1016/j.cpc.2006.03.007.

[214] J.-W. Jiang, H.S. Park, T. Rabczuk, Molecular dynamics simulations of single-layer molybdenum disulphide (MoS2): Stillinger-Weber parametrization, mechanical properties, and thermal conductivity, J. Appl. Phys. 114 (2013) 64307. doi:10.1063/1.4818414.

[215] J. Zhang, X.-L. Liu, Y. Wen, L. Shi, R. Chen, H. Liu, B. Shan, Titanium trisulfide (TiS3) monolayer as a potential thermoelectric material: first-principles based Boltzmann transport study, ACS Appl. Mater. Interfaces. 9 (2017) 2509–2515.

[216] G. Wang, R. Pandey, S.P. Karna, Carbon phosphide monolayers with superior carrier mobility, Nanoscale. 8 (2016) 8819–8825.

[217] M. Zhou, X. Chen, M. Li, A. Du, Widely Tunable And Anisotropic Charge Carrier Mobility In Monolayer Tin (II) Selenide Using Biaxial Strain: A First-principles Study, J. Mater. Chem. C. 5 (2017) 1247–1254.

[218] S. Guo, Spin-orbit and strain effect on power factor in monolayer MoS2, Comput. Mater. Sci. 123 (2016) 8–13. doi:10.1016/j.commatsci.2016.06.011.

[219] H.J. Goldsmid, J.W. Sharp, Estimation of the thermal band gap of a semiconductor from Seebeck measurements, J. Electron. Mater. 28 (1999) 869–872. doi:10.1007/s11664-999-0211-y.

[220] T. Kubo, R. Häusermann, J. Tsurumi, J. Soeda, Y. Okada, Y. Yamashita, N. Akamatsu, A. Shishido, C. Mitsui, T. Okamoto, S. Yanagisawa, H. Matsui, J. Takeya, Suppressing molecular vibrations in organic semiconductors by inducing strain, Nat. Commun. 7 (2016) 11156.

[221] B. Peng, H. Zhang, H. Shao, Y. Xu, X. Zhang, H. Zhu, Thermal conductivity of monolayer MoS2, MoSe2, and WS2: Interplay of mass effect, interatomic bonding and anharmonicity, arXiv. 6 (2015) 1–19. doi:10.1039/c5ra19747c.

[222] S. Kumar, U. Schwingenschlögl, Thermoelectric response of bulk and monolayer MoSe2 and WSe2, Chem. Mater. 27 (2015) 1278–1284. doi:10.1021/cm504244b.

[223] D. Wang, J. Meng, X. Zhang, G. Guo, Z. Yin, H. Liu, L. Cheng, M. Gao, J. You, R. Wang, Selective Direct Growth of Atomic Layered HfS2 on Hexagonal Boron Nitride for High Performance Photodetectors, Chem. Mater. 30 (2018) 3819–3826. doi:10.1021/acs.chemmater.8b01091.

[224] E. Vassalou, P. Tsipas, J. Marquez-Velasco, D. Tsoutsou, A. Dimoulas, N. Kelaidis, K.E. Aretouli, S.A. Giamini, E. Xenogiannopoulou, Two-dimensional semiconductor HfSe2 and MoSe2/HfSe2 van der Waals heterostructures by molecular beam epitaxy, Appl. Phys. Lett. 106 (2015) 143105. doi:10.1063/1.4917422.

[225] G. Ding, G.Y. Gao, Z. Huang, W. Zhang, K. Yao, Thermoelectric properties of monolayer MSe2 (M = Zr, Hf): Low lattice thermal conductivity and a promising figure of merit, Nanotechnology. 27 (2016) 375703. doi:10.1088/0957-4484/27/37/375703.

[226] H.Y. Lv, W.J. Lu, X. Luo, H.Y. Lu, X.B. Zhu, Y.P. Sun, Enhancing the thermoelectric performance of a HfS2 monolayer through valley engineering, arXiv:1608.05464. (2016). http://arxiv.org/abs/1608.05464.

[227] S. Ju, T. Shiga, L. Feng, J. Shiomi, Revisiting PbTe to identify how thermal conductivity is really limited, Phys. Rev. B. 97 (2018) 184305. doi:10.1103/PhysRevB.97.184305.

[228] M.K. Han, Y. Jin, D.H. Lee, S.J. Kim, Thermoelectric properties of Bi2Te3: CuI and the

effect of its doping with Pb atoms, Materials (Basel). 10 (2017) 1235. doi:10.3390/ma10111235.

[229] A. Shafique, Y.H. Shin, Thermoelectric and phonon transport properties of two-dimensional IV-VI compounds, Sci. Rep. 7 (2017) 506. doi:10.1038/s41598-017-00598-7.

[230] G. Li, K. Yao, G. Gao, Strain-induced enhancement of thermoelectric performance of TiS2 monolayer based on first-principles phonon and electron band structures, Nanotechnology. 29 (2018) 15204. doi:10.1088/1361-6528/aa99ba.

[231] G. Zhang, Y.W. Zhang, Thermoelectric properties of two-dimensional transition metal dichalcogenides, J. Mater. Chem. C. 5 (2017) 7684–7698. doi:10.1039/c7tc01088e.

[232] N. Hung, A.R.T. Nugraha, T. Yang, Z. Zhang, R. Saito, Thermoelectric performance of monolayer InSe improved by convergence of multivalley bands, J. Appl. Phys. 125 (2019) 82502. doi:10.1063/1.5040752.

[233] G. Ding, J. Chen, K. Yao, G. Gao, Convergence of separate orbits for enhanced thermoelectric performance of layered ZrS2, New J. Phys. 19 (2017) 73036. doi:10.1088/1367-2630/aa7b58.

[234] T. Sohier, M. Gibertini, D. Campi, G. Pizzi, N. Marzari, Valley-Engineering Mobilities in Two-Dimensional Materials, Nano Lett. 19 (2019) 3723–3729. doi:10.1021/acs.nanolett.9b00865.

[235] D. Zou, C. Yu, Y. Li, Y. Ou, Y. Gao, Pressure-induced enhancement in the thermoelectric properties of monolayer and bilayer SnSe2, R. Soc. Open Sci. 5 (2018) 171827. doi:10.1098/rsos.171827.

[236] D. Qin, X.J. Ge, G.Q. Ding, G.Y. Gao, J.T. Lü, Strain-induced thermoelectric performance enhancement of monolayer ZrSe2, RSC Adv. 7 (2017) 47243–47250. doi:10.1039/c7ra08828k.

[237] N. Glebko, A.J. Karttunen, Lattice thermal conductivity of TiS2 , ZrS2 , and HfS2 : Periodic trends studied by dispersion-corrected hybrid density functional methods, Phys. Rev. B. 100 (2019) 24301. doi:10.1103/physrevb.100.024301.

[238] G. Özbal, R.T. Senger, C. Sevik, H. Sevinçli, Ballistic thermoelectric properties of monolayer semiconducting transition metal dichalcogenides and oxides, Phys. Rev. B. 100 (2019) 85415. doi:10.1103/PhysRevB.100.085415.

[239] G. Yumnam, T. Pandey, A.K. Singh, High temperature thermoelectric properties of Zr and Hf based transition metal dichalcogenides: A first principles study, J. Chem. Phys. 143 (2015) 234704. doi:10.1063/1.4937774.

[240] G. Kresse, J. Hafner, Ab initio molecular dynamcis for liquid metals, Phys. Rev. B. 47 (1993) 558. https://journals.aps.org/prb/pdf/10.1103/PhysRevB.47.558.

[241] J. Perdew, K. Burke, Y. Wang, Generalized gradient approximation for the exchange-correlation hole of a many-electron system, Phys. Rev. B. 54 (1996) 16533–16539. doi:10.1103/PhysRevB.54.16533.

[242] A. Togo, L. Chaput, I. Tanaka, Distributions of phonon lifetimes in Brillouin zones, Phys. Rev. B. 91 (2015) 94306. doi:10.1103/PhysRevB.91.094306.

[243] X. Gonze, J.C. Charlier, D.C. Allan, M.P. Teter, Interatomic force constants from first principles: The case of α-quartz, Phys. Rev. B. 50 (1994) 13035–13038. doi:10.1103/PhysRevB.50.13035.

[244] X. Gonze, C. Lee, Dynamical matrices, Born effective charges, dielectric permittivity tensors, and interatomic force constants from density-functional perturbation theory, Phys. Rev. B - Condens. Matter Mater. Phys. 55 (1997) 10355–10368. doi:10.1103/PhysRevB.55.10355.

[245] D. Wang, X. Zhang, H. Liu, J. Meng, J. Xia, Z. Yin, Y. Wang, J. You, X.M. Meng, Epitaxial growth of HfS2 on sapphire by chemical vapor deposition and application for photodetectors, 2D Mater. 4 (2017) 31012. doi:10.1088/2053-1583/aa7ea2.

[246] T. Eknapakul, I. Fongkaew, S. Siriroj, R. Vidyasagar, J.D. Denlinger, L. Bawden, S.K. Mo, P.D.C. King, H. Takagi, S. Limpijumnong, W. Meevasana, Nearly-free-electron system of monolayer Na on the surface of single-crystal HfSe2, Phys. Rev. B. 94 (2016) 201121 (R). doi:10.1103/PhysRevB.94.201121.

[247] T. Eknapakul, I. Fongkaew, S. Siriroj, W. Jindata, S. Chaiyachad, S.K. Mo, S. Thakur, L. Petaccia, H. Takagi, S. Limpijumnong, W. Meevasana, Direct observation of strain-induced orbital valence band splitting in HfSe2 by sodium intercalation, Phys. Rev. B. 97 (2018) 201104(R). doi:10.1103/PhysRevB.97.201104.

[248] X. Gu, R. Yang, Phonon transport in single-layer transition metal dichalcogenides: A first-principles study, Appl. Phys. Lett. 105 (2014) 131903. doi:10.1063/1.4896685.

[249] J. Kang, H. Sahin, F.M. Peeters, Mechanical properties of monolayer sulphides: a

comparative study between MoS2 , HfS2 and TiS3, Phys. Chem. Chem. Phys. 17 (2015) 27742–27749. doi:10.1039/C5CP04576B.

[250] C. Habenicht, L. Sponza, R. Schuster, M. Knupfer, B. Büchner, Mapping of the energetically lowest exciton in bulk 1T-HfS2, Phys. Rev. B. 98 (2018) 155204. doi:10.1103/PhysRevB.98.155204.

[251] G.A. Akhmedova, D.S. Abdinov, Effect of thallium doping on the thermal conductivity of PbTe single crystals, Inorg. Mater. 45 (2009) 854–858. doi:10.1134/s0020168509080056.

[252] Y. Xiao, C. Chang, Y. Pei, D. Wu, K. Peng, X. Zhou, S. Gong, J. He, Y. Zhang, Z. Zeng, L.D. Zhao, Origin of low thermal conductivity in SnSe, Phys. Rev. B. 94 (2016) 125203. doi:10.1103/PhysRevB.94.125203.

[253] A. Bano, P. Khare, N.K. Gaur, Thermal transport properties of bulk and monolayer MoS2: An ab-initio approach, J. Phys. Conf. Ser. 836 (2017) 12052. doi:10.1088/1742-6596/836/1/012052.

[254] Dimple, N. Jena, A. Rawat, R. Ahammed, M.K. Mohanta, A. De Sarkar, Emergence of high piezoelectricity along with robust electron mobility in Janus structures in semiconducting Group IVB dichalcogenide monolayers, J. Mater. Chem. A. 6 (2018) 24885–24898. doi:10.1039/C8TA08781D.

[255] A. Molina-Sanchez, L. Wirtz, A. Molina-Sánchez, L. Wirtz, Phonons in single-layer and few-layer MoS2 and WS2, Phys. Rev. B - Condens. Matter Mater. Phys. 84 (2011) 155413. doi:10.1103/PhysRevB.84.155413.

[256] A.B. Laursen, S. Kegnæs, S. Dahl, I. Chorkendorff, Molybdenum sulfides—efficient and viable materials for electro-and photoelectrocatalytic hydrogen evolution, Energy Environ. Sci. 5 (2012) 5577–5591.

[257] Y. Li, H. Wang, L. Xie, Y. Liang, G. Hong, H. Dai, MoS2 nanoparticles grown on graphene: an advanced catalyst for hydrogen evolution reaction, J. Am. Chem. Soc. 133 (2011) 7296–7299.

[258] Z. Chen, D. Cummins, B.N. Reinecke, E. Clark, M.K. Sunkara, T.F. Jaramillo, Core–shell MoO3–MoS2 nanowires for hydrogen evolution: a functional design for electrocatalytic materials, Nano Lett. 11 (2011) 4168–4175.

[259] H. Vrubel, D. Merki, X. Hu, Hydrogen evolution catalyzed by MoS3 and MoS2 particles,

Energy Environ. Sci. 5 (2012) 6136–6144.

[260] D. Merki, X. Hu, Recent developments of molybdenum and tungsten sulfides as hydrogen evolution catalysts, Energy Environ. Sci. 4 (2011) 3878–3888.

[261] H.I. Karunadasa, E. Montalvo, Y. Sun, M. Majda, J.R. Long, C.J. Chang, A molecular MoS2 edge site mimic for catalytic hydrogen generation, Science (80-.). 335 (2012) 698–702.

[262] E. Parzinger, B. Miller, B. Blaschke, J.A. Garrido, J.W. Ager, A. Holleitner, U. Wurstbauer, Photocatalytic stability of single-and few-layer MoS2, ACS Nano. 9 (2015) 11302–11309.

[263] X. Hai, W. Zhou, K. Chang, H. Pang, H. Liu, L. Shi, F. Ichihara, J. Ye, Engineering Crystallinity of MoS2 Monolayers for Highly Efficient Solar Hydrogen Production, J. Mater. Chem. A. 5 (2017) 8591–8598.

[264] H. Wang, F. Wen, X. Li, X. Gan, Y. Yang, P. Chen, Y. Zhang, Cerium-doped MoS2 nanostructures: Efficient visible photocatalysis for Cr (VI) removal, Sep. Purif. Technol. 170 (2016) 190–198.

[265] P. Liu, Y. Liu, W. Ye, J. Ma, D. Gao, Flower-like N-doped MoS2 for photocatalytic degradation of RhB by visible light irradiation, Nanotechnology. 27 (2016) 225403.

[266] Y.-L.Y. Li, Y.-L.Y. Li, C.M. Araujo, W. Luo, R. Ahuja, Single-layer MoS2 as an efficient photocatalyst, Catal. Sci. Technol. 3 (2013) 2214. doi:10.1039/c3cy00207a.

[267] H. He, J. Lin, W. Fu, X. Wang, H. Wang, Q. Zeng, Q. Gu, Y. Li, C. Yan, B.K. Tay, MoS2/TiO2 Edge-On Heterostructure for Efficient Photocatalytic Hydrogen Evolution, Adv. Energy Mater. 6 (2016) 1600464.

[268] K. Chang, Z. Mei, T. Wang, Q. Kang, S. Ouyang, J. Ye, MoS2/graphene cocatalyst for efficient photocatalytic H2 evolution under visible light irradiation, ACS Nano. 8 (2014) 7078–7087.

[269] J. Xu, X. Cao, Characterization and mechanism of MoS 2/CdS composite photocatalyst used for hydrogen production from water splitting under visible light, Chem. Eng. J. 260 (2015) 642–648.

[270] S. Zhang, F. Tang, J. Liu, W. Che, H. Su, W. Liu, Y. Huang, Y. Jiang, T. Yao, Q. Liu, MoS 2-coated ZnO nanocomposite as an active heterostructure photocatalyst for hydrogen evolution, Radiat. Phys. Chem. 137 (2017) 104–107.

[271] J. Wang, Z. Guan, J. Huang, Q. Li, J. Yang, Enhanced photocatalytic mechanism for the hybrid gC3 N4/MoS2 nanocomposite, J. Mater. Chem. A. 2 (2014) 7960–7966.

[272] P. Abbasi, M. Asadi, C. Liu, S. Sharifi-Asl, B. Sayahpour, A. Behranginia, P. Zapol, R. Shahbazian-Yassar, L.A. Curtiss, A. Salehi-Khojin, Tailoring the edge structure of molybdenum disulfide toward electrocatalytic reduction of carbon dioxide, ACS Nano. 11 (2016) 453–460.

[273] M. Asadi, B. Kumar, A. Behranginia, B.A. Rosen, A. Baskin, N. Repnin, D. Pisasale, P. Phillips, W. Zhu, R. Haasch, Robust carbon dioxide reduction on molybdenum disulphide edges, Nat. Commun. 5 (2014) 4470.

[274] P. Liao, E.A. Carter, New concepts and modeling strategies to design and evaluate photo-electro-catalysts based on transition metal oxides, Chem. Soc. Rev. 42 (2013) 2401–2422.

[275] D.K. Kanan, E.A. Carter, Band gap engineering of MnO via ZnO alloying: a potential new visible-light photocatalyst, J. Phys. Chem. C. 116 (2012) 9876–9887.

[276] Y. Li, Y. Li, C. Tang, ScienceDirect Strain engineering and photocatalytic application, Int. J. Hydrogen Energy. 42 (2016) 161–167. doi:10.1016/j.ijhydene.2016.11.097.

[277] K. Yan, T.A. Maark, A. Khorshidi, V.A. Sethuraman, A.A. Peterson, P.R. Guduru, The Influence of Elastic Strain on Catalytic Activity in the Hydrogen Evolution Reaction, Angew. Chemie. 128 (2016) 6283–6289.

[278] H. Feng, Z. Xu, L. Wang, Y. Yu, D. Mitchell, D. Cui, X. Xu, J. Shi, T. Sannomiya, Y. Du, Modulation of photocatalytic properties by strain in 2D BiOBr nanosheets, ACS Appl. Mater. Interfaces. 7 (2015) 27592–27596.

[279] M. Shen, Z. Yan, L. Yang, P. Du, J. Zhang, B. Xiang, MoS2 nanosheet/TiO2 nanowire hybrid nanostructures for enhanced visible-light photocatalytic activities, Chem. Commun. 50 (2014) 15447–15449.

[280] T. Adit Maark, B.R.K. Nanda, Enhancing CO2 Electroreduction by Tailoring Strain and Ligand Effects in Bimetallic Copper–Rhodium and Copper–Nickel Heterostructures, J. Phys. Chem. C. 121 (2017) 4496–4504.

[281] M. Du, Q. Wan, Z. Wang, L. Cui, Elastic strain effects on the photocatalytic TiO2 nanofilm: Utilizing the martensitic surface relief of FeNiCoTi alloy substrate, Chem. Phys. Lett. 658 (2016) 130–133.

[282] Y. Yang, T.A. Maark, A. Peterson, S. Kumar, Elastic strain effects on catalysis of a PdCuSi metallic glass thin film, Phys. Chem. Chem. Phys. 17 (2014) 1746–1754.

[283] T. Adit Maark, A.A. Peterson, Understanding strain and ligand effects in hydrogen evolution over Pd (111) surfaces, J. Phys. Chem. C. 118 (2014) 4275–4281.

[284] X. Jiang, J. Nisar, B. Pathak, J. Zhao, R. Ahuja, Graphene oxide as a chemically tunable 2-D material for visible-light photocatalyst applications, J. Catal. 299 (2013) 204–209. doi:10.1016/j.jcat.2012.12.022.

[285] S.N. Shirodkar, U. V Waghmare, T.S. Fisher, R. Grau-Crespo, Engineering the electronic bandgaps and band edge positions in carbon-substituted 2D boron nitride: a first-principles investigation, Phys. Chem. Chem. Phys. 17 (2015) 13547–13552. doi:10.1039/C5CP01680K.

[286] Y.-L. Li, Y. Li, C. Tang, Strain engineering and photocatalytic application of single-layer ReS2, Int. J. Hydrogen Energy. 42 (2017) 161–167.

[287] Dimple, J. Nityasagar, S.D. Behere, A. De Sarkar, The effects of different possible modes of uniaxial strain on the tunability of electronic and band structures in MoS2 monolayer nanosheet via first-principles density functional theory, Pramana–J. Phys. 89 (2017) 2.

[288] M. Gajdoš, K. Hummer, G. Kresse, J. Furthmüller, F. Bechstedt, Linear optical properties in the projector-augmented wave methodology, Phys. Rev. B. 73 (2006) 45112.

[289] L. Li, M. Zhao, Structures, energetics, and electronic properties of multifarious stacking patterns for high-buckled and low-buckled silicene on the MoS2 substrate, J. Phys. Chem. C. 118 (2014) 19129–19138.

[290] D.M. Guzman, A. Strachan, Role of strain on electronic and mechanical response of semiconducting transition-metal dichalcogenide monolayers: An ab-initio study, J. Appl. Phys. 115 (2014) 243701.

[291] L. Feng, J. Su, Z. Liu, Effect of vacancies on structural, electronic and optical properties of monolayer MoS2: a first-principles study, J. Alloys Compd. 613 (2014) 122–127.

[292] W.S. Yun, S.W. Han, S.C. Hong, I.G. Kim, J.D. Lee, Thickness and strain effects on electronic structures of transition metal dichalcogenides: 2H-MX2 semiconductors (M= Mo, W; X= S, Se, Te), Phys. Rev. B. 85 (2012) 33305.

[293] H. Soni, P.K. Jha, Ab-initio study of dynamical properties of two dimensional MoS2 under strain, AIP Adv. 5 (2015) 107103.

[294] M.-H. Chiu, C. Zhang, H.-W. Shiu, C.-P. Chuu, C.-H. Chen, C.-Y.S. Chang, C.-H. Chen, M.-Y. Chou, C.-K. Shih, L.-J. Li, Determination of band alignment in the single-layer MoS2/WSe2 heterojunction, Nat. Commun. 6 (2015) 7666.

[295] S. Ahmad, S. Mukherjee, A comparative study of electronic properties of Bulk MoS2 and Its monolayer using DFT technique: application of mechanical Strain on MoS2 monolayer, Graphene. 3 (2014) 52–59.

[296] D. Lloyd, X. Liu, J.W. Christopher, L. Cantley, A. Wadehra, B.L. Kim, B.B. Goldberg, A.K. Swan, J.S. Bunch, Band gap engineering with ultralarge biaxial strains in suspended monolayer MoS2, Nano Lett. 16 (2016) 5836–5841.

[297] H.J. Conley, B. Wang, J.I. Ziegler, R.F. Haglund Jr, S.T. Pantelides, K.I. Bolotin, Bandgap engineering of strained monolayer and bilayer MoS2, Nano Lett. 13 (2013) 3626–3630.

[298] Y. V Morozov, M. Kuno, Optical constants and dynamic conductivities of single layer MoS2, MoSe2, and WSe2, Appl. Phys. Lett. 107 (2015) 83103.

[299] G.Y. Jia, Y. Liu, J.Y. Gong, D.Y. Lei, D.L. Wang, Z.X. Huang, Excitonic quantum confinement modified optical conductivity of monolayer and few-layered MoS 2, J. Mater. Chem. C. 4 (2016) 8822–8828.

[300] T. Cheiwchanchamnangij, W.R.L. Lambrecht, Quasiparticle band structure calculation of monolayer, bilayer, and bulk MoS2, Phys. Rev. B. 85 (2012) 205302.

[301] A.S. Rodin, A. Carvalho, A.H.C. Neto, Excitons in anisotropic two-dimensional semiconducting crystals, Phys. Rev. B. 90 (2014) 75429.

[302] M. Feierabend, A. Morlet, G. Berghäuser, E. Malic, Impact of strain on the optical fingerprint of monolayer transition metal dichalcogenides, Phys. Rev. B. 96 (2017) 45425.

[303] R.K. Defo, S. Fang, S.N. Shirodkar, G.A. Tritsaris, A. Dimoulas, E. Kaxiras, Strain dependence of band gaps and exciton energies in pure and mixed transition-metal dichalcogenides, Phys. Rev. B. 94 (2016) 155310.

[304] S. Xie, Q. Zhang, G. Liu, Y. Wang, Photocatalytic and photoelectrocatalytic reduction of CO2 using heterogeneous catalysts with controlled nanostructures, Chem. Commun.

52 (2016) 35–59.

[305] A.F. Alkaim, T.A. Kandiel, F.H. Hussein, R. Dillert, D.W. Bahnemann, Enhancing the photocatalytic activity of TiO2 by pH control: a case study for the degradation of EDTA, Catal. Sci. Technol. 3 (2013) 3216–3222.

[306] R. Kuriki, O. Ishitani, K. Maeda, Unique Solvent Effects on Visible-Light CO2 Reduction over Ruthenium (II)-Complex/Carbon Nitride Hybrid Photocatalysts, ACS Appl. Mater. Interfaces. 8 (2016) 6011–6018.

[307] R. Kuriki, H. Matsunaga, T. Nakashima, K. Wada, A. Yamakata, O. Ishitani, K. Maeda, Nature-inspired, highly durable CO2 reduction system consisting of a binuclear ruthenium (II) complex and an organic semiconductor using visible light, J. Am. Chem. Soc. 138 (2016) 5159–5170.

[308] V. Chakrapani, J.C. Angus, A.B. Anderson, S.D. Wolter, B.R. Stoner, G.U. Sumanasekera, Charge transfer equilibria between diamond and an aqueous oxygen electrochemical redox couple, Science (80-.). 318 (2007) 1424–1430.

[309] C. Du, X. Huang, C. Jiang, X. Pu, Z. Zhao, L. Jing, W. Hu, Z.L. Wang, Tuning carrier lifetime in InGaN/GaN LEDs via strain compensation for high-speed visible light communication, Sci. Rep. 6 (2016) 37132.

[310] E.M. Grumstrup, M.M. Gabriel, C.W. Pinion, J.K. Parker, J.F. Cahoon, J.M. Papanikolas, Reversible strain-induced electron–hole recombination in silicon nanowires observed with femtosecond pump–probe microscopy, Nano Lett. 14 (2014) 6287–6292.

[311] Y. Zhang, J. Ye, Y. Matsuhashi, Y. Iwasa, Ambipolar MoS2 thin flake transistors, Nano Lett. 12 (2012) 1136–1140.

[312] J. Linnera, A.J. Karttunen, Ab initio study of the lattice thermal conductivity of Cu2O using the generalized gradient approximation and hybrid density functional methods, Phys. Rev. B. 96 (2017) 14304. doi:10.1103/PhysRevB.96.014304.

[313] D.C. Wallace, Thermodynamics of Crystals, Dover, Mineola, New York, 1990. https://www.abebooks.co.uk/9780486402123/Thermodynamics-Crystals-WALLACE-0486402126/plp.

Vita

Mr. Dimple received his Bachelor in Science degree with mains in Physics, Mathematics and Computer Science from D.A.V. College, Jalandhar (Punjab), India in 2012. He received his Master's degree with first class in Physics from Dr. B. R. Ambedkar National Institute of Technology (NIT), Jalandhar, India in 2014. Then, he joined Institute of Nano Science and Technology (INST), Mohali, and registered with Indian Institute of Science Education and Research (IISER), Mohali for his Ph.D. studies in August, 2014. He is a student of First Ph.D. Batch at INST, Mohali. His current research interest is mainly focussed on computationally exploration of advanced atomically-thin layered 2D materials for energy conversion applications such as: mechanical energy harvesting (Nanoscale Piezoelectricity), Waste-heat harvesting (2D Thermoelectricity), and Solar-energy harvesting: Artificial Photosynthesis.